

# **Modelling flood induced sediment motion and mechanical erosion in an alpine river**

Master thesis

To achieve the  
Master's degree MSc

at the Faculty of Natural and Life Sciences  
of the Paris Lodron University Salzburg

Submitted by Michaela Sichert  
Student ID: 01616117

Supervisor: Assoz. Prof. Priv.- Doz. Mag. Dr. Jörg Robl

Department of Environment and Biodiversity

Salzburg, February 2022

## **Declaration of originality**

I hereby declare in lieu of an oath that I have written this thesis independently and have not used any sources or aids other than those indicated. All references that have been taken verbatim or in terms of content from the stated sources are marked as such. This thesis has not yet been submitted as a master's thesis in the same or a similar form.

A handwritten signature in black ink, appearing to read "M. Sichert".

---

Salzburg, 08.02.2022 Michaela Sichert

## **Acknowledgement**

I would like to take this opportunity to thank everyone who supported me during the completion of this master thesis.

Special thanks go to my main supervisor, Assoz. Prof. Dr. Jörg Robl, for his advice, his constructive comments and his active and motivating support.

I also want to thank my secondary supervisor, Ass. Prof. Dr. Jan- Christoph. Otto, for his support not only during this thesis, but throughout my studies.

I would also like to thank Mag. Gerald Griesebner and the hydrographic service of Salzburg for providing important data.

Last but not least, I would like to thank my parents, Helga and Dipl- Ing. Thomas Sichert, and my partner, Sebastian Moderegger, for their support and encouragement throughout my studies.

## Abstract

Torrents are not continuously morphologically active but show a threshold limited behaviour. Thus, single flood events in alpine environments control the morphological changes in riverine landscapes. During these relevant phases of river flow, not only sediment remobilisation but also mechanical bedrock erosion occurs in alpine rivers and torrents. One of those rivers where both processes are frequently observed is the Taugl River in the province of Salzburg. The alteration of riverine landscapes can be linked to single flood events due to the bed shear stress exerted by the stream and critical shear stresses which are required for initial sediment motion and bedrock erosion.

The aim of this thesis was to develop a fluid dynamic model in order to predict the triggering discharge rates leading to incipient sediment motion and mechanical erosion by plucking and to evaluate these events in terms of their magnitude and frequency. Initially, the threshold range for initial sediment motion was calculated between 46.35 Pa and 66.21 Pa and for plucking between 486 Pa and 684 Pa. These critical values were implemented in a fluid dynamic model based on the Gerris Flow Solver. By simulating single flood events with different magnitudes, a threshold discharge of  $\geq 3 \text{ m}^3/\text{s}$  and  $\geq 25 \text{ m}^3/\text{s}$  was identified, which is required to trigger initial sediment motion and plucking, respectively. In addition, a discharge rate of  $\geq 25 \text{ m}^3/\text{s}$  was determined as necessary for overbank floods. The assessment of the frequency and magnitude of the threshold discharges showed that initial sediment motion occurs at high frequency but low magnitude, and plucking as well as overbank floods occur at low frequency but high magnitude. As both, the frequency and the magnitude of flood events exceeding the critical bed shear stresses play a major role in the evolution of landscapes in terms of morphological changes, a UAV based monitoring series was continued. Thereby, alterations in the riverine landscape were documented via DEM and orthophoto generation by applying Structure from Motion photogrammetry. Due to an analysis of the derived remote sensing data in dedicated areas along the river course, the simulation results were comprehensively confirmed and verified.

Although the detailed analyses performed in this Master thesis are related to a section of the Taugl River, the chosen methodology and equations can be used for research in similar study areas. The results of this thesis thus contribute to the research in fluvial geomorphology by predicting single flood induced morphological changes in alpine rivers.

## **Zusammenfassung**

Wildbäche sind nicht kontinuierlich morphologisch aktiv, sondern zeigen ein schwellenbegrenztes Verhalten. Daher steuern einzelne Hochwasserereignisse im alpinen Raum die morphologischen Veränderungen in den Flusslandschaften. Während dieser relevanten Abflussphasen kommt es in alpinen Flüssen und Wildbächen nicht nur zu einer Remobilisierung von Sedimenten, sondern auch zur mechanischen Festgesteinserosion. Einer der Flüsse, an denen beide Prozesse häufig zu beobachten sind, ist die Taugl im Salzburger Land. Die Veränderung von Flusslandschaften kann mit einzelnen Hochwasserereignissen aufgrund der vom Strom ausgeübten Sohlscherspannung und einer kritischen Scherspannung, die für die anfängliche Sedimentbewegung oder Festgesteinserosion erforderlich ist, verknüpft werden.

Ziel dieser Masterarbeit war es, ein strömungsdynamisches Modell zu entwickeln, um die auslösenden Abflussraten, die zu initiale Sedimentbewegung und zu mechanischer Erosion durch Plucking führen, vorherzusagen und diese Ereignisse hinsichtlich ihrer Magnitude und Frequenz zu bewerten. Zunächst wurde der Schwellenbereich für die anfängliche Sedimentbewegung zwischen 46,35 Pa und 66,21 Pa und für Plucking zwischen 486 Pa und 684 Pa berechnet. Diese kritischen Werte wurden in ein fliddynamisches Modell, basierend auf dem Gerris Flow Solver, implementiert. Durch die Simulation einzelner Hochwasser mit unterschiedlichen Abflussraten wurde ein kritischer Abfluss von  $\geq 3 \text{ m}^3/\text{s}$  und  $\geq 25 \text{ m}^3/\text{s}$  identifiziert, der erforderlich ist, um eine initiale Sedimentbewegung bzw. Plucking auszulösen. Für die Überflutung des gesamten Überschwemmungsbereichs wurde eine Abflussrate von  $\geq 25 \text{ m}^3/\text{s}$  identifiziert. Die Bewertung der Häufigkeit und des Ausmaßes der Ergebnisse ergab, dass die initiale Sedimentbewegung mit hoher Frequenz aber geringer Magnitude auftritt, während Plucking und die Überschwemmungen des gesamten Überflutungsbereichs mit geringer Frequenz aber hoher Magnitude eintreten. Da die Häufigkeit und das Ausmaß von Hochwasserereignissen, die die kritische Sohlscherspannung überschreiten, eine wichtige Rolle bei der Landschaftsentwicklung spielt, wurde eine mehrjährige UAV-gestützte Überwachungsserie fortgesetzt. Dadurch wurden Veränderungen in der Flusslandschaft durch generierte DEMs und Orthophotos mit Hilfe von Structure from Motion Photogrammetrie dokumentiert. Durch die Auswertung der abgeleiteten Fernerkundungsdaten in bestimmten Bereichen entlang des Flusslaufs wurden die Simulationsergebnisse umfassend bestätigt und verifiziert.

Obwohl sich die detaillierten Analysen dieser Masterarbeit auf einen Flussabschnitt der Taugl beziehen, können die gewählten Methoden und Gleichungen auch für die Forschung in ähnlichen Untersuchungsgebieten verwendet werden. Die Ergebnisse dieser Arbeit tragen somit zur Erforschung der fluvialen Geomorphologie bei, indem sie morphologische Änderungen infolge von einzelnen Hochwassern in einer alpinen Umgebung vorhersagen.

## Table of contents

Declaration of originality .....	I
Acknowledgement.....	II
Abstract .....	III
Zusammenfassung.....	IV
List of figures .....	VII
List of figures (appendix) .....	VIII
List of tables .....	IX
List of abbreviations .....	X
1    Introduction .....	1
2    Alteration of riverine landscapes.....	2
2.1    Physics of sediment and block motion .....	2
2.2    Flood events .....	8
3    Study area .....	11
3.1    Geology .....	13
3.2    Geomorphology .....	14
3.3    Climate and discharge .....	15
3.4    Flora and fauna.....	18
4    Methods .....	20
4.1    Photogrammetry .....	20
4.1.2    Data acquisition.....	23
4.1.3    Data processing .....	24
4.2    Hydraulic modelling.....	25
4.2.1    Numerical models in fluvial geomorphology .....	26
4.2.2    Model development .....	27
4.2.2.1    Calculation of thresholds for initial sediment motion and plucking.....	27
4.2.2.2    Setting up an executable flood simulation file .....	29
5    Results .....	34
5.1    Monitoring.....	34
5.2    Critical shear stresses .....	37
5.3    Simulating floods of different magnitudes .....	40

---

**Table of contents**

5.4	Initial sediment motion.....	46
5.5	Critical shear stress for plucking .....	50
6	Discussion .....	53
6.1	Overbank floods .....	53
6.2	Initial sediment motion.....	54
6.2.1	Advantages and potential errors of determining the median grain diameter based on the calculated roughness map.....	54
6.2.2	Sediment remobilization.....	55
6.3	Flood induced bedrock incision due to plucking.....	57
7	Conclusion.....	59
	References .....	60
	Appendix .....	65

## List of figures

Figure 1: Force balance on grain .....	3
Figure 2: Calculating block entrainment based on five main forces .....	6
Figure 3: Overview map.....	11
Figure 4: Flow length profile.....	12
Figure 5: a) Hillshade and b) slope within the AOI .....	12
Figure 6: Geology in the Taugl River catchment .....	13
Figure 7: Mechanical bedrock erosion observed in the AOI.....	14
Figure 8: View from a gravel bank onto the main channel .....	15
Figure 9: Mean monthly and annual temperature [°C].....	16
Figure 10: Total monthly and annual precipitation [mm] .....	17
Figure 11: Averaged annual water level [m] and discharge [m <sup>3</sup> /s] .....	17
Figure 12: Section of the histogram showing the discharge rates in relation to the frequency .....	18
Figure 13: Tauglgries (marked in green) and European natural reserve (red area) .....	19
Figure 14: Geometrical basics of photogrammetry .....	22
Figure 15: Structure from Motion (SfM) photogrammetric survey method.....	23
Figure 16: TwinFOLD GEO drone .....	24
Figure 17: Workflow showing the main processing steps of aerial images using Agisoft Metashape Professional .....	25
Figure 18: Main steps for setting up an executable parameter file for flood simulations .....	29
Figure 19: Subdivision of a a) quadtree and the corresponding b) tree representation .....	30
Figure 20: Location of inflow.....	31
Figure 21: Virtual data loggers.....	32
Figure 22: Sections of the orthomosaics derived by drone surveys .....	34
Figure 23: Sections of the orthomosaic derived via drone survey from 23.07.2021 .....	35
Figure 24: Sections of the DEMs from 2016 to 2021.....	36
Figure 25: Sections of the DEM 2016 and 2021 in the middle of the AOI.....	37
Figure 26: Comparison of the grain size [m] count based on a) field measurements and b) statistical evaluation of the calculated roughness map .....	38
Figure 27: Roughness map .....	38
Figure 28: Linear correlation between the median grain size $D_{50}$ and the critical shear stress for incipient sediment motion .....	39

Figure 29: Ratio between protrusion height P [m] and block length L [m] .....	40
Figure 30: Varying critical Shields stress [ ] for block entrainment by sliding.....	40
Figure 31: Peak flow of 1 m <sup>3</sup> /s modelled with the Gerris flow solver .....	41
Figure 32: Water depth at the stations 3 (solid line) and 6 (scattered line) during increasing discharge rates .....	42
Figure 33: Water depth [m] across the three profiles during peak flows of increasing magnitude.....	42
Figure 34: Evolution of maximum water depth [m] during rising discharge rates .....	43
Figure 35: Alteration in maximum flow velocity [m/s] during increasing peak flows rates.....	44
Figure 36: Exerted maximum bed shear stress [Pa] during rising discharge rates .....	45
Figure 37: Relationship between variable discharge rates and the maximum values of the main physical parameters .....	46
Figure 38: Ratio between the maximum applied bed shear stress and the lower and upper threshold for initial sediment motion.....	47
Figure 39: Maximum bed shear stress [Pa] plotted against the distance of the profiles during rising peak flows .....	48
Figure 40: Increasing maximum bed shear stress [Pa] during rising peak flows at the eight stations ..	49
Figure 41: Ratio between maximum bed shear stress and the a) lower (486 Pa) and b) upper (684 Pa) critical shear stress for plucking jointed limestone .....	50
Figure 42: Maximum bed shear stress [Pa] plotted against the distance of a) profile 1 and b) profile 2 during rising peak flows .....	51
Figure 43: Increasing maximum bed shear stress [Pa] during rising peak flows at the three susceptible stations.....	52

## **List of figures (appendix)**

Appendix 1: Orthomosaic and derived DEM processed with SfM photogrammetry and acquired via drone survey from 23.04.2018 with a spatial resolution of 0.05 m.....	67
Appendix 2: Orthomosaic and derived DEM processed with SfM photogrammetry and acquired via drone survey from 04.12.2019 with a spatial resolution of 0.05 m .....	67
Appendix 3: Orthomosaic and derived DEM processed with SfM photogrammetry and acquired via drone survey from 23.07.2021with a spatial resolution of 0.05 m .....	68

## **List of tables**

Table 1: Density [kg/m <sup>3</sup> ] of some rock types .....	5
Table 2: Typical friction angles [°] of some type of rocks .....	8
Table 3: Critical bed shear stresses required for initial sediment motion and plucking limestone beds	37
Table 4: Critical discharge rates necessary to cause initial sediment motion at the virtual data loggers .....	49
Table 5: Critical discharge rates necessary to cause bed shear stresses that surpass at least the lower threshold for block entrainment by sliding.....	52

## List of abbreviations

ALS	Airborne laser scanning
AMR	Adaptive mesh refinement
AOI	Area of interest
CFD	Computational fluid dynamic
DEM	Digital elevation model
GCP	Ground control point
GCS	Ground control station
GFS	Gerris flow solver
GMT	Generic mapping tools
GNSS	Global navigation satellite system
GPS	Global positioning system
GSD	Ground sample distance
IMU	Inertial measurement unit
MEMS	Microelectromechanical
MVS	Multi- view stereo
UAV	Unmanned aircraft vehicle
RS	Remote Sensing
SDW	Smart, Duncan and Walsh friction model
SIFT	Scale invariant feature transform
SWE	Shallow water equations

# 1 Introduction

Flood events are a key factor for the alteration of riverine landscapes. They cause changes in the riverbed by sediment remobilization and bedrock erosion. Unfortunately, the importance of such events in alpine regions is not fully understood since variations in erosion and transportation during flood events are poorly researched yet (Baynes et al., 2015). Alterations of riverine landscapes by single flood events result from the shear stress exerted by the fluid and a critical value required to initially mobilize sediments or to erode bedrock (Larsen and Lamb, 2016). The shear stress describes the downstream acting force and is considered as one of the most important parameters in fluvial geomorphology (Rhoads, 2020). Since the magnitude of flood events must be large enough to exceed the critical value for sediment motion or mechanical bedrock erosion, rivers are not continuously geomorphologically active, but only beyond a certain discharge rate (Whipple et al., 2013, Larsen and Lamb, 2016). Changes in riverine landscapes occur whenever critical thresholds are surpassed by the shear stress (Phillips and Jerolmack, 2016). With increasing magnitude, not only the exerted shear stress in the main channels increases, but also the entire floodplain is progressively flooded (Bridge, 2003). Despite the impacts of bankfull floods on geomorphological changes, the shear stresses exerted in torrents are not well investigated so far. A high shear stress at the channel bed triggers initial sediment motion, but also leads to bedrock erosion through the main processes, abrasion and plucking. Plucking, or quarrying, is comparatively less studied, although this process is considered to be highly efficient (Hurst et al., 2021). Plucking can be observed exceptionally well in the Taugl River, a torrent in the province of Salzburg, which is the subject of the following study. Through mechanical erosion and as a result of sediment remobilisation, the river dynamically changes the landscape it flows through.

In the scope of this thesis, the effects of single flood events with varying magnitudes are investigated with regard to threshold exceedance. To accomplish this, the critical shear stress for incipient sediment motion and mechanical erosion through plucking are to be physically calculated. The aim of this thesis is to predict the triggering discharge rates and evaluate them in terms of their frequency and magnitude. This requires the development of a calibrated, physically based fluid dynamic model to simulate single floods of different magnitudes. By modelling different peak flows, overbank floods can be determined and susceptible sites for initial sediment motion and plucking are located during events of various magnitudes. To understand and monitor the alteration in the riverine landscape, a time series of remote sensing data was evaluated and analysed. The resulting database of geomorphological changes was expanded by recent drone surveys based on photogrammetric methods. In summary, the following five research questions will be answered through this study:

1. What is the threshold for incipient sediment motion?
2. At which critical shear stress does bedrock incision by plucking occur?
3. Where and at which threshold discharge is the Taugl River geomorphologically active within the study area?
4. Which discharge rate leads to overbank floods?
5. Is the trigger for exceeding the threshold discharges rather magnitude or frequency of single flood events?

## 2 Alteration of riverine landscapes

Calculating the initial motion is one of the major problems in sedimentology and geomorphology, despite its importance (Lamb et al., 2008). Sediment transport as well as bedrock incision are generally based on a basal shear stress caused by the flux, showing a threshold limited behaviour (Snyder et al., 2003, DiBiase and Whipple, 2011, Scherler et al., 2017). This concept is explained further below, including the influence of flood events on shear stress and on the attainment of thresholds for sediment transport and mechanical erosion by plucking (Whipple et al., 2013, Lamb et al., 2015).

### 2.1 Physics of sediment and block motion

The physical principle of particle movement is based on a concept of four forces in equilibrium (Wiberg and Smith, 1987, Kirchner et al., 1990). Incipient motion is caused if the downstream upwards acting forces exceed the forces that hold sediments back on the channel bed (Wiberg and Smith, 1987). The buoyancy force  $F_B$ , the lift force  $F_L$  and the drag force  $F_D$  are thus causing sediment motion, whereas the gravitational force  $F_G$  acts against them in order to keep the grains in place (Figure 1) (Wiberg and Smith, 1987, Lamb et al., 2008, Lamb et al., 2015). Those forces affect all sediments laying on the channel bed within the stream and control the grain motion (Kirchner et al., 1990). Once they are in balance (within a coordinate system parallel to the riverbed), the sediments start to move. This so called force balance model (1) is based on the four involved forces, the bed slope  $\theta$  and the friction angle by  $\phi$  (Lamb et al., 2008).

$$F_D + (F_G - F_B) \sin \theta = [(F_G - F_B) \cos \theta - F_L] \tan \phi \quad (1)$$

The buoyancy force (2c) acts in the contrary direction to the gravitational force (2d). Here,  $F_B$  works vertically and not in perpendicular to the flow. The lift force (2b) is vertical to the channel bed and the drag force (2a) acts parallel to the stream (Lamb et al., 2008). The friction angle is also called particle angle of response, because it describes the resistance of sediments from being moved by the stream (Wiberg and Smith, 1987, Kirchner et al., 1990). The four main forces can be expressed as followed (Lamb et al., 2008):

$$F_D = \frac{1}{2} C_D \rho (u^2) A_{xs} \quad (2a)$$

$$F_L = \frac{1}{2} C_L \rho (u^2) A_{xs} \quad (2b)$$

$$F_B = \rho g V_{ps} \quad (2c)$$

$$F_G = \rho_S g V_p \quad (2d)$$

Here,  $C_D$  and  $C_L$  are the corresponding drag and lift coefficients,  $\rho_S$  and  $\rho$  are the sediment and water densities, respectively (Lamb et al., 2008). The flow velocity is denoted as  $u$  (Larsen and Lamb, 2016).  $V_p$  describes the particle volume, whereas  $V_{ps}$  is the submerged particle volume.  $A_{xs}$  is the cross sectional area of the sediment vertical to the stream. The combination and rearrangement of the equations 2a - 2c

enable the calculation of different parameters for hydraulic modelling e.g. the Shields number (Lamb et al., 2008).

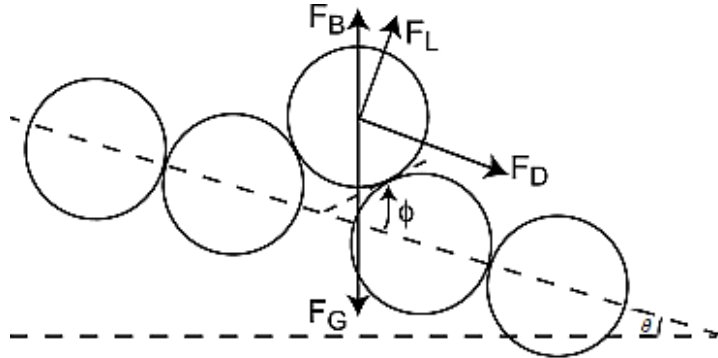


Figure 1: Force balance on grain.  $F_B$ ,  $F_L$ ,  $F_D$  and  $F_G$  are the forces due to buoyancy, lift, drag and gravity, respectively.  $\phi$  is the friction angle and  $\theta$  is the bed-slope angle. The figure was modified after Lamb et al., (2008).

### Shear stress

In studies about fluvial dynamics, the shear stress is one of the most important parameters as it defines the force acting downstream. Therefore, the shear stress can initiate the incipient movement of sediments (Rhoads, 2020). It depends on the slope and the flow velocity, which is controlled by the water depth (Scherler et al., 2017). Under the assumption of a steady and uniform flow behaviour, the average shear stress  $\tau_0$  can be calculated by the product of the water density and the bed shear velocity  $u_*$ :

$$\tau_0 = \rho u_*^2 = \rho g d I \quad (3)$$

where  $g$  is the gravitational acceleration,  $d$  is the mean flow depth and  $I$  represents the mean slope (Hancock et al., 1998, Snyder et al., 2003, Ferguson, 2007, Lamb and Dietrich, 2009, Zhang et al., 2015, Lapotre et al., 2016, Noss and Lorke, 2016, Rhoads, 2020, Bartels et al., 2021). The shear velocity  $u_*$  can be computed as the square root of the bed shear stress  $\tau_b$  divided by the density of water (4) (Smart et al., 2002, Lamb et al., 2008, Lamb et al., 2015).

$$u_* = \sqrt{\tau_b / \rho} \quad (4)$$

The local shear stress varies within the flow above the channel bed. The reason for the spatial variation is the changing extension of the overlaying water. Consequently, the shear stress decrease with increasing distance from channel bed and turns to 0 while reaching the surface (Rhoads, 2020). The bed shear stress describes the complex interaction between the flow of a stream and the channel bed roughness (Ferguson, 2007, Noss and Lorke, 2016). In order to calculate the actual shear stress on the channel bed friction must be considered. Since several friction coefficients exist, various equations to calculate the bed shear stress are valid (Larsen and Lamb, 2016, Noss and Lorke, 2016). One established formula (5) uses for example the friction coefficient  $C_f$ , which is multiplied with the flow velocity and the water density (Larsen and Lamb, 2016).

$$\tau_b = \rho u^2 C_f \quad (5)$$

Here, the bed shear stress  $\tau_b$  [Pa] is additionally dependent on Manning's  $n$ , as this coefficient is needed to calculate the friction (6). Thereby, the water depth  $h$  is also included (Larsen and Lamb, 2016).

$$C_f = \frac{gn^2}{h^{1/3}} \quad (6)$$

Overall, several flow resistance models exist which utilise a vast variety of friction coefficients (e.g. the Darcy-Weisbach parameter  $f$  or Chezy's  $C$ ). In general, the friction coefficient describes the flow resistance or the ratio between the average flow velocity and the shear velocity ( $u_*/u$ ) (Smart et al., 2002). The roughness, i.e. the amount of irregularities of a riverbed surface, has a great influence on the flow resistance. Woody debris and vegetation have thus also a high impact. The hydraulic roughness is often used as a parameter equal to the riverbed grain size (Noss and Lorke, 2016).

### Threshold for incipient sediment motion

Surpassing a critical level of bed shear stress to initiate sediment motion became a popular concept in the sediment transport theory (NiÑo et al., 2003). The threshold shear stress describes the minimum that is needed for incipient motion (Scherler et al., 2017). The ability of rivers to mobilize grains of a given size is also called competence. It is quantified by the Shields number  $\tau^*$  (Church, 2006):

$$\tau^* = \frac{\tau_b}{(\rho_s - \rho)gD} \quad (7)$$

The Shields number expresses the amount of bed shear stress caused by the flow on a sediment with a specific weight per unit area. Thus, it is controlled by the grain diameter  $D$  and the sediment density  $\rho_s$  (Table 1), but also by the gravitational acceleration and water density. For incipient motion a critical Shields number  $\tau_c^*$  varying with different grain sizes must be surpassed (Kirchner et al., 1990, Lamb et al., 2008, Scheingross et al., 2013, Lamb et al., 2015). In most cases, the median grain diameter  $D_{50}$  is used for the calculation of the critical value (Kirchner et al., 1990, Johnson, 2014, Lamb et al., 2015). Generally, smaller particles are moving earlier than coarser ones, since a corresponding lower critical shear stress needs to be exceeded (Lamb et al., 2008). However, it is also possible to use the largest transported grain diameter  $D_{max}$  in order to identify the critical shear stress during flood events. Thus, the identification of only one grain size is needed for the calculation (Scheingross et al., 2013). This approach is based on the assumption that smaller grains reach the incipient motion at a lower threshold than the largest one (Lamb et al., 2008, Scheingross et al., 2013). Consequently, the bed shear stress must refer to its maximal value  $\tau_{max}$ . In order to calculate the critical Shields number for initial sediment motion, equation (7) was modified to (Scheingross et al., 2013):

$$\tau_c^* = \frac{\tau_{max}}{(\rho_s - \rho)gD_{max}} \quad (8)$$

The initiation of particle motion varies between areas covered with alluvium and uncovered bedrock (Johnson, 2014). In addition, a difference between low and steep gradients can be recognized. Gravel-bed rivers with lower slope angles allow the determination of a constant critical Shields number ( $\tau_c^* \sim 0.045$ ). But typically it ranges between 0.03 and 0.06 (Church, 2006, Scheingross et al., 2013, Johnson, 2014). Under the assumption of a critical Shields number of 0.045 for low gradient gravel-bed rivers, the threshold shear stress for incipient motion  $\tau_b^*$  can be calculated by rearranging equation (7) to:

$$\tau_b^* = \tau_c^*(\rho_s - \rho)gD = 0.045(\rho_s - \rho)gD_{50} \quad (9)$$

where  $\tau_c^* = 0.045$  and the grain diameter corresponds to the median  $D_{50}$  (Larsen and Lamb, 2016). In contrast, this would not be appropriate for steep rivers. It is still discussed whether the critical shear stress increases or decreases due to a higher gradient (Scheingross et al., 2013). Some argue, that the critical bed shear stress decreases with the increasing gravitational force due to the comparatively higher gradient (e.g., Wiberg and Smith, 1987). According to recent studies, the critical Shields stress increase with the gradient because of the alteration of flow velocity and the emergence of turbulences caused by the changing ratio between water depth and grain size (e.g., Lamb et al., 2008).

*Table 1: Density [kg/m<sup>3</sup>] of some rock types. Table modified from Selby (1993).*

Rock type	Density [kg/m <sup>3</sup> ]
<b>Andesite</b>	2400
<b>Basalt</b>	2600 – 2800
<b>Conglomerate</b>	2500 – 2700
<b>Dolomite</b>	2400 – 2700
<b>Granite</b>	2640
<b>Limestone</b>	2300 – 2700
<b>Phyllite</b>	2800
<b>Quartzite</b>	2500 – 2800
<b>Sandstone</b>	2200 – 2500
<b>Schist</b>	2400 – 2800

### Threshold for block entrainment

The entry of blocks into bedrock rivers is still poorly investigated. However, those threshold values are important for inferring the bedrock incision through plucking (Lamb et al., 2015). Plucking is one of the most effective processes in eroding well jointed bedrock (Lamb and Dietrich, 2009). It occurs whenever the drag and lift forces are strong enough to separate the blocks from the riverbed (Whipple et al., 2013). Therefore, the threshold for incipient motion is dependent on the balance of the dominant hydrodynamic forces that act on the blocks and the gravitational force for stabilization (Figure 2) (Yang et al., 2019). Vertical entrainment, sliding and toppling are the three main processes that cause block entrainment (Hurst et al., 2021). Through vertical entry, a gap in the previous block position within the bedrock occurs (Lamb et al., 2015). In nature, this mechanism occurs very rare since high wall stresses on all

block sides and uncommonly high lift forces are needed (Hurst et al., 2021). In contrast, sliding and toppling can take place where adjacent blocks in downstream direction have already entered the channel (Lamb et al., 2015). They are strongly affected by bedding structure and fracture distances, controlled by the length ( $L$ ) and height ( $H$ ) of the block (Hurst et al., 2021).

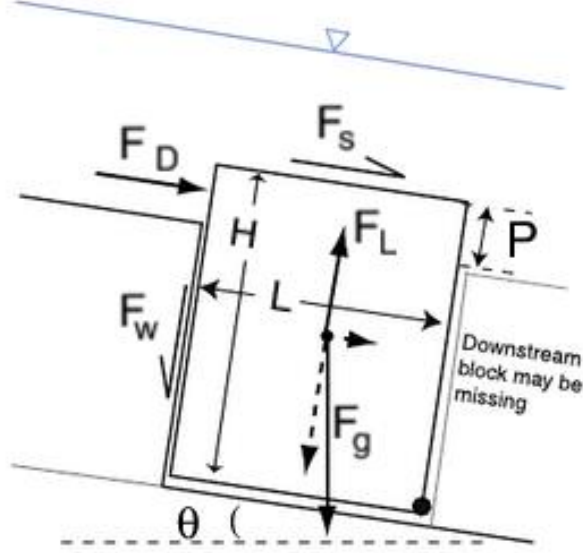


Figure 2: Calculating block entrainment based on five main forces. Buoyancy and gravity are summarized as  $F_g$ , the shear stress acting downstream is represented as  $F_s$ , the drag force  $F_d$  is dependent on the protrusion height  $P$ , the lift force  $F_L$  is acting parallel to the flux and frictional forces  $F_w$  are determined by the sidewalls. For vertical entrainment the pivot point (dot at lower right corner) is crucial, whereas the mechanisms of sliding and toppling are based on the assumption of a missing block further downstream. The channel bed angle is represented as  $\theta$  (Lamb et al., 2015).

Under the assumption of submerged and well jointed (in parallel and perpendicular to the channel), rectangular blocks, five main forces exists (Figure 2). Here, buoyancy and gravity forces can be aggregated as  $F_g$ , the basal shear stress is expressed as  $F_s$  and friction along the walls is represented as  $F_w$ :

$$F_g = LWHg(\rho_r - \rho) \quad (10a)$$

$$F_s = \tau_b LW \quad (10b)$$

$$F_w = \tau_w A_w \quad (10c)$$

The block width ( $W$ ), bulk density ( $\rho_r$ ), the hydraulic lift ( $F_L^*$ ) and the frictional stress ( $\tau_w$ ) along an area of the sidewalls ( $A_w$ ) are included (Lamb et al., 2015). By considering the dimensionless local drag parameter  $C_D$ , impacts of block shape, orientation and roughness in relation to the flux are involved in block entrainment equations (Hurst et al., 2021). Moreover, the drag force  $F_d$  controlled by the drag coefficient  $C_D$  (2a) and the hydraulic lift force  $F_L$  controlled by the lift coefficient  $C_L$  (2b) can be rewritten as (Lamb et al., 2008, Hurst et al., 2021):

$$F_D = \frac{1}{2} C_D \rho u^2 PW \quad (10d)$$

$$F_L = \frac{1}{2} C_L \rho u^2 PW \quad (10e)$$

In contrast, Lamb et al., (2015) defined the hydraulic lift force  $F_L$  as a linear function due to the multiplication of a constant lift  $F_L^*$  force with the sum of drag and shear force:

$$F_L = F_L^*(F_D + F_S) \quad (10f)$$

In most cases, sliding is the main reason for block entrainment (Larsen and Lamb, 2016). The critical stress for block entrainment by sliding  $\tau_{pc}^*$  is based on the assumption of a force balance that is parallel to the channel (Lamb et al., 2015). Consequently, block entrainment is approached if the driving forces surpass resisting forces (e.g. basal and side wall friction) (Hurst et al., 2021). By considering submerged blocks, the critical Shields number can be expressed by (Lamb et al., 2015):

$$\tau_{pc}^* = \frac{\cos(\theta) [\tan(\phi) - \tan(\theta)] + 2\tau_w^*}{\left[1 + \frac{1}{2} C_D \left(\frac{u}{u_*}\right)^2 \frac{P}{L}\right] [1 + F_L^* \tan(\phi)]} \quad (11)$$

Again,  $\theta$  is the bed angle and  $\phi$  is the bed friction angle (Figure 2) (Lamb et al., 2015, Larsen and Lamb, 2016). Typical friction angles for different rock types are listed in Table 2 (Selby, 1993). Furthermore, the ratio between the protrusion height and the block length, as well as the relation between flow and shear velocity are included (Larsen and Lamb, 2016). The dimensionless sidewall stress of the block is  $\tau_w^* = \frac{\tau_w}{(\rho_s - \rho)gW}$ . Due to the sliding motion, only two sidewalls are affected by this frictional stress in parallel to the flow direction (Lamb et al., 2015). However, the sidewall stress is difficult to determine (Larsen and Lamb, 2016). In the case of  $\tau_w^* \sim 1$ , the sidewall stress would approach the block weight per unit area, which is very rare in nature (Lamb et al., 2015). If  $\tau_w^* \sim 0$  in contrast, the joint would be widely open. A block sidewall stress of 0.3 for example would define a wall stress of 30% of the block weight per unit area, which occurs if there is a cohesion between the blocks (Larsen and Lamb, 2016). The dimensionless drag coefficient  $C_D$  depends on the Reynolds number  $Re = \frac{\rho U d}{\mu}$ . Here,  $U$  is the mean velocity based on the average depth  $d$  and  $\mu$  is the kinematic viscosity (Lamb et al., 2015, Lamb et al., 2008). After calculating the critical Shields number  $\tau_{pc}^*$ , the resulting value can be used to compute the critical shear stress for plucking by block sliding  $\tau_{pc}$  (Larsen and Lamb, 2016):

$$\tau_{pc} = \tau_{pc}^* (\rho_s - \rho) g D \quad (12)$$

Table 2: Typical friction angles [ $^{\circ}$ ] of some type of rocks under the assumption of a flat and unweathered surface. Table modified from Selby (1993).

<b>Rock type</b>	<b>Moisture</b>	<b>Friction angle [<math>^{\circ}</math>]</b>
<b>Basalt</b>	Dry	35 – 38
	Wet	31 - 36
<b>Dolerite</b>	Dry	36
	Wet	32
<b>Gneiss</b>	Dry	26 – 29
	Wet	23 - 26
<b>Limestone</b>	Dry	31 – 37
	Wet	27 - 35
<b>Sandstone</b>	Dry	26 – 35
	Wet	25 – 34

## 2.2 Flood events

From a geomorphological point of view, the key task of rivers is the transportation of sediment. That is the reason why this process can be called ‘geomorphic work’ of rivers (Rhoads, 2020). The importance of the ratio between sediment flux and transport capacity as well as the key role of a critical threshold for erosion are well-known with regard to the climate, tectonics and relief (Whipple et al., 2013). Variations in transportation rates occur due to changing discharge rates and bed shear stresses which are typically caused by flood events (Lamb et al., 2015). Therefore, a correlation between floods and fluvial transport capacity exists (Guan et al., 2016, Phillips and Jerolmack, 2016, Rhoads, 2020). This relationship determines the rate of geomorphic work during various discharge rates (Rhoads, 2020). Flood events must be large enough to surpass the critical thresholds for incipient sediment motion or to initiate bedrock incision (Whipple et al., 2013, Larsen and Lamb, 2016). The consequence of those processes is the alteration of riverine landscapes (Phillips and Jerolmack, 2016). Analysing the geomorphological effectiveness due to extreme events like flooding with a high magnitude is thus an event based concept (Rhoads, 2020). By definition, a large flood has a magnitude which is two times bigger than mean annual events but occur only infrequent and last for a short time (Guan et al., 2016, Rhoads, 2020). Such extreme events contribute significantly to alteration in channel morphology and river hydraulics for short or long term. The origins of floods vary, for example they can be caused by intense rainfall (flash floods), dam bursts or glacial outburst (Guan et al., 2016).

Channel widening or incision, denudation and withdrawal and channel disconnection are the most frequent erosive results from high magnitude flood impacts. During flood events, the fluvial transport capability is higher. Consequently, bigger grain sizes can be transported leading to geomorphological changes since sediments act like erosive tools. The effects on deposits may be recognised by the formation of bars within the riverbed, vertical accumulation on floodplains (e.g. sand ridges, gravel stripes, etc.) or channel infilling (Rhoads, 2020). Channel adjustment itself can have an impact on flooding. High deposition rates reduce the potential channel capacity which leads to the formation of a larger floodplain (Guan et al., 2016). Overall, sediment from both channel and overbank flows is deposited on the floodplains. The inundation in this area is therefore only temporary. When discharge

rates rise, the floodplain is progressively covered with water (Bridge, 2003). Consequently, the water depths in the main channel are significantly higher than in the floodplain. During the peak flow, the entire floodplain is inundated, resulting in a wide but shallow channel (floodplain). However, it contains narrower and deeper channels (main channels) (Riahi-Madvar et al., 2011). The evolution of inundation and the resulting sediment transport on floodplains is complex as it depends on varying width, topography (e.g. depressions), vegetation, anthropogenic influence as well as grain size and availability. The highest flow velocities in overbank floods occur in the main channel and decrease laterally (Bridge, 2003, Fernandes, 2021). The same applies to basal shear stress. The flow velocity is also higher in zones of channel convergence than in diverging zones (Bridge, 2003). In addition, roughness is an important control factor. Overall, the interaction between the spatially varying higher and lower flow velocities causes a so called shear layer in the transition zone (Fernandes, 2021). If the discharge rates decrease again, the water flows back into the main channels as a result of drainage and groundwater flow. Determining the recurrence interval of overbank flows is difficult because of uncertainties in the definition of a bankfull level. However, it is typically an interval of less than one year up to two years (Bridge, 2003).

Bedrock incision results in minor overbank flows instead (Guan et al., 2016). Erosion rates in bedrock rivers are generally low during medium or low water levels. But during high magnitude and low frequency flood events, the higher sediment transport capacities lead to an increasing erosion rate (Kim et al., 2006). The efficiency of erosion is thereby higher no matter if a bedrock channel is covered by a thin sediment layer between the flood events (Whipple et al., 2013, Hurst et al., 2021). Consequently bedrock erosion is not a continuous process, it rather occurs intermittent due to infrequent flooding whenever the critical shear stress is exceeded (Snyder et al., 2003, DiBiase and Whipple, 2011). This is the reason why bedrock erosion processes are primarily studied in relation to extreme events (Kim et al., 2006). For modelling the evolution of riverine landscapes over time, it is thus important to take threshold for incipient motion into account and to analyse thereby the stochastic distribution of erosive events (Snyder et al., 2003). Besides considering the immediately geomorphological response during a single but high magnitude flood, it is important to analyse the effects of flooding with a higher frequency but lower magnitude. Such a repetition of events in a short period of time cause sediment exploitation. Sedimentary evidence from previous flooding may be disappeared thereby. This makes understanding sediment dynamics and the reconstruction of hydraulics more difficult in comparison to single floods (Guan et al., 2016).

Models of topographic changes require a wide time scale, which also makes climate to an important component that is unfortunately often not considered (Snyder et al., 2003). Linking fluvial erosion and climate trough precipitation is difficult for bedrock rivers. One reason among others is that both discharge and sediment supply control the incision rate (Phillips and Jerolmack, 2016). Magnitude and frequency of flood events depend on hydrological variations, e.g. peak values in the discharge (Guan et al., 2016). Due to the high transport capacity during flood events, riverine landscapes can change in a short period of time (Baynes et al., 2015, Rhoads, 2020). A recovery to the initial situation is unlikely, especially if big grain sizes were transported and deposited that only a high- magnitude flood can mobilize (Rhoads, 2020). Thus, previous studies about flood events have focussed on the analysis of the deposited particle sizes and on simulating the hydrological conditions (Baynes et al., 2015). However, the reconstruction of geomorphological and hydrological parameters is difficult. Larsen and Lamb

(2016) used the geometry of canyons and the deposited sediments to conclude on the discharge, water depth and bed shear stress of outburst floods (Larsen and Lamb, 2016). Even if high magnitude events alter the channel morphology rapidly and significantly, the rarity of those large floods need to be considered. Moreover, smaller but frequent floods can lead to a significant channel change as well, based on the concept of accumulation. This states infrequent high magnitude floods transport large amounts of sediment, but the cumulative geomorphological work of smaller, higher frequency floods can be equal to or greater than these quantities. In total, the impact of flood events is controlled by magnitude and frequency (Wolman and Miller, 1960).

### 3 Study area

The area of interest (AOI) is part of the Taugl River catchment, which is located on the south-western edge of the Osterhorn Group in the Northern Calcareous Alps in the Salzburger Land (Guttmann, 1997). The Taugl River originates from a spring on the Gruberhorn (Osterhorn Group) and discharges on the right into the Salzach River, which drains a large area of the Eastern Alps (Figure 3) (Rettenbacher and Rettenbacher-Höllwerth, 1982, Janitz, 2012, Hergarten et al., 2013, Tourismusverband Bad Vigaun, 2021). The catchment area is bordered by the ridge of Schlenken (1649 m), Schmittenstein (1696 m), Gruberhorn (1734 m), Trattberg (1758 m) and is descending over the crest line of the Koloman plateau (Spiegler, 1971). The catchment drained by the Taugl River is about 50 km<sup>2</sup> (Leditzky, 1990). The AOI is located between the municipalities Bad Vigaun and Kuchl.

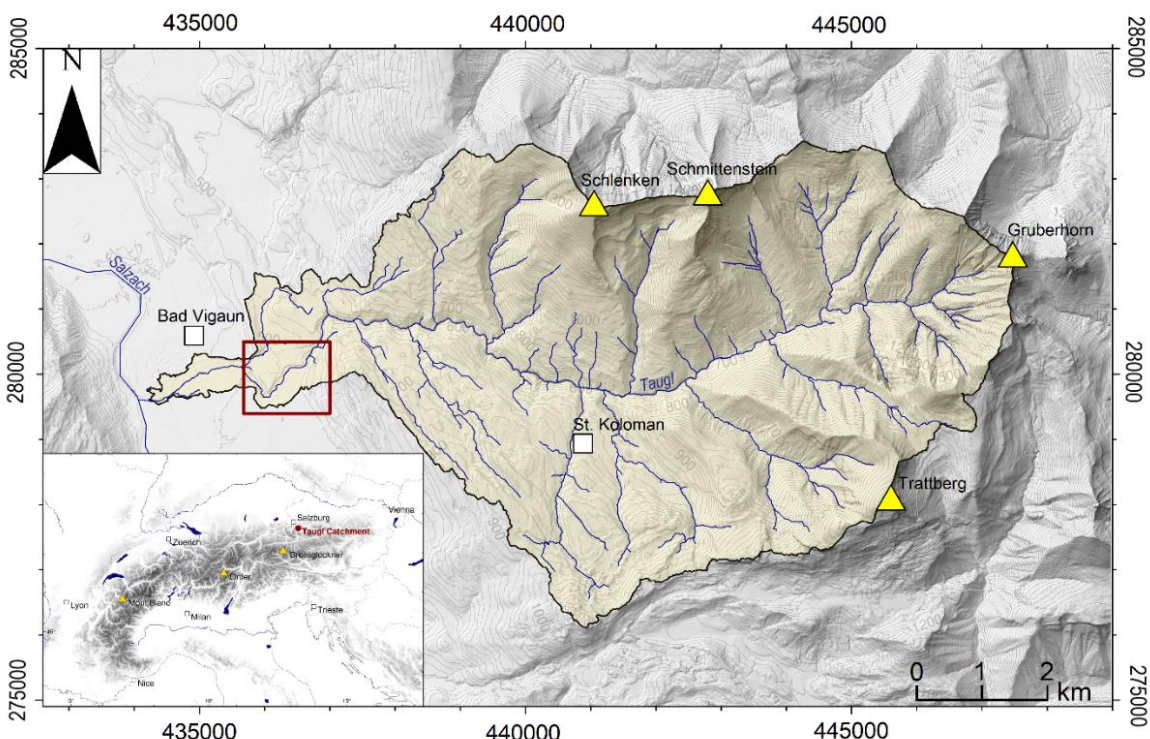


*Figure 3: Overview map showing the location of the AOI (red rectangle) within Taugl River catchment (yellow area). The drainage system is represented by blue lines. Yellow triangles represent mountain peaks located at the drainage divide. The Salzach River (receiving stream) and the municipality Bad Vigaun (white square) are shown for a better orientation. The inset indicates the position of the Taugl River catchment within the European Alps (hillshade derived from DEM 2013 provided by the state government of Salzburg; Streams are provided by data.gv.at).*

The difference in altitude between the origin and the confluence point is approximately 500 m, whereby the Taugl River emerges at an altitude of about 950 m.a.s.l. and the confluence with the Salzach River is at a height of approx. 460 m.a.s.l. (Figure 4) (Guttmann, 1997). Along the course from the headwaters to the confluence with the Salzach River, numerous tributaries discharge into the alpine river (Guttmann, 1997; Spiegeler, 1971). Those low order streams play an important role within the fluvial network, because they are significant sediment sources (Noss and Lorke, 2016). From its origin, the Taugl River flows over a distance of about 14 km before it reaches the so called Römer Brücke (Spiegeler, 1971), which marks the upstream limit of the AOI. On its way down, the alpine river has heavily incised into

its bedrock, so that 8 km of the course leads through a narrow gorge with steep, roughly 50 m high and almost vertical slopes (Guttmann, 1997, Hergarten et al., 2013).

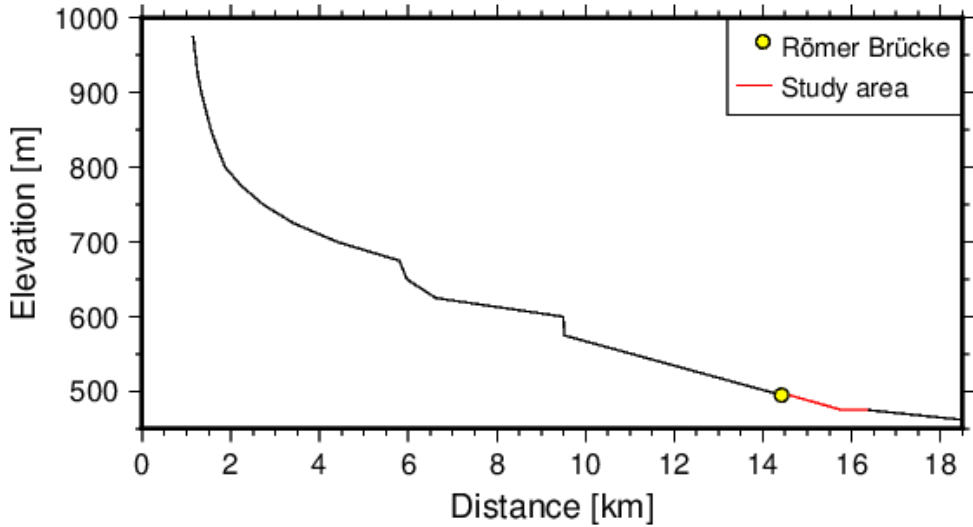


Figure 4: Flow length profile. The decline in elevation [m] with increasing distance [km] from the origin of the Taugl River (~ 950 m.a.s.l.) and the confluence point with the Salzach River (~ 460 m.a.s.l.) is represented by the line. The position of the Römer Brücke (yellow circle) is shown, marking the upstream limit of the study area, which extent is highlighted (red line).

The Römer Brücke (500 m.a.s.l.) marks the upstream limit of the study area. About 50 m downstream, the gorge ends where gently tipping limestone beds of the Oberalm formation are partly buried by alluvium (Guttmann, 1997). At the transition between the gorge and the alluvial segment, the channel is rather narrow and features deep scours (Spiegler, 1971, Janitz, 2012). Downstream, a huge low gradient alluvial cone stretches into the Salzach valley (Figure 5). Thereby, a wide riverbed with several temporally vegetated banks have developed (Guttmann, 1997, Janitz, 2012). Overall, the gorge has become a valley with a debris covered bed and incipient lateral erosion at its lower reach (Spiegler, 1971). In total, the AOI extends about 2 km in an east- west direction, but bedrock outcrops only in the first 800 m partially exposed at the surface.

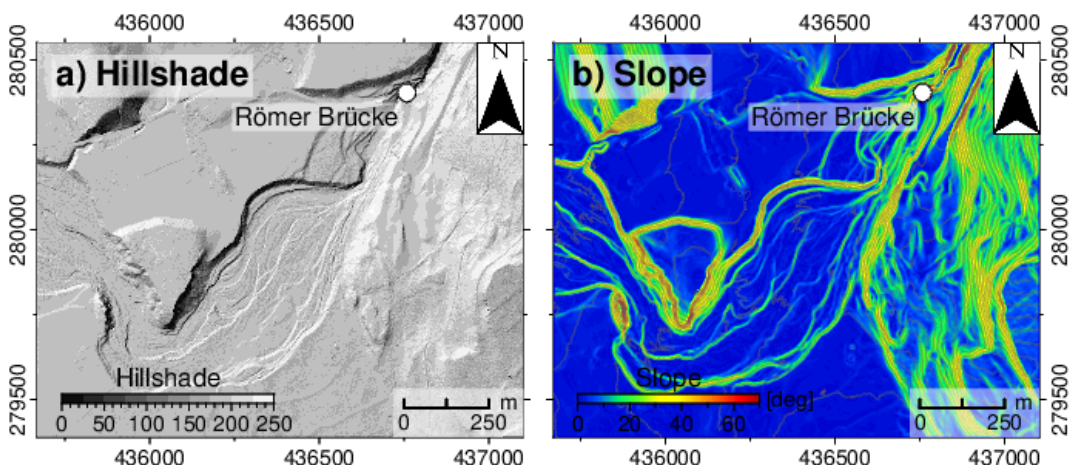


Figure 5: a) Hillshade and b) slope within the AOI. The Römer Brücke (white circle) marks the upstream limit of the study area (products derived from DEM 2013, provided by the state government of Salzburg).

### 3.1 Geology

The Taugl River catchment is located in the south- western edge of the Osterhorn Group and hence located in the Austroalpine unit of the Tirolikum (Guttmann, 1997). The majority of the exposed bedrock at the surface is limestone (Spiegler, 1971). Overall, the geological setting of the Taugl catchment area can be classified into four main formations, the Adnet strata, the Tauglboden strata, the Oberalm strata and the Schrambach strata (Guttmann, 1997; Rettenbacher and Rettenbacher-Höllwerth, 1982):

The Adnet strata, comprising red-coloured, bulbous limestone beds, is overlaid by the Tauglboden formations (Rettenbacher and Rettenbacher-Höllwerth, 1982, Guttmann, 1997). The Tauglboden is the landscape unit located in the proximity to the headwaters (Spiegler, 1971, Guttmann, 1997). The corresponding strata is mainly composed thin- beded, grey, siliceous and marl limestones. The Tauglboden formations are covered by the Oberalm strata of marl limestones and barmstone limestones. The (light) grey marl limestone comprise the main mass, in which the brown barmstone limestone is intercalated in four horizons (Rettenbacher and Rettenbacher-Höllwerth, 1982, Guttmann, 1997). The stratification of the marl limestones are flat, but thinner bed joints with softer calcareous marl are embedded between those in comparison harder beds. Clay beds are partially enclosed in the barmstone limestone (Rettenbacher and Rettenbacher-Höllwerth, 1982). Comparatively, the barmstone limestone is the hardest formation and is thereby more resistant to erosion than other rock types (Spiegler, 1971). The fourth main strata within the Taugl catchment is the Schrambach formation which partly covers the barmstone limestone (Rettenbacher and Rettenbacher-Höllwerth, 1982).

Figure 6a provides a general overview of the surface near lithology within the entire catchment. The AOI is located in the transition section between bedrock and alluvium. The dominant bedrock lithology for the whole Taugl catchment is carbonatic rock. Figure 6b shows the geological situation of the Taugl catchment in detail. Grey, banked limestone from the Oberalm formation dominates the bedrock. Within the AOI, the surface near lithology is composed of alluvial loam, silt, sand, gravel and partly stones, which is typical for floodplains and river deposits (Geologische Bundesanstalt, 2021).

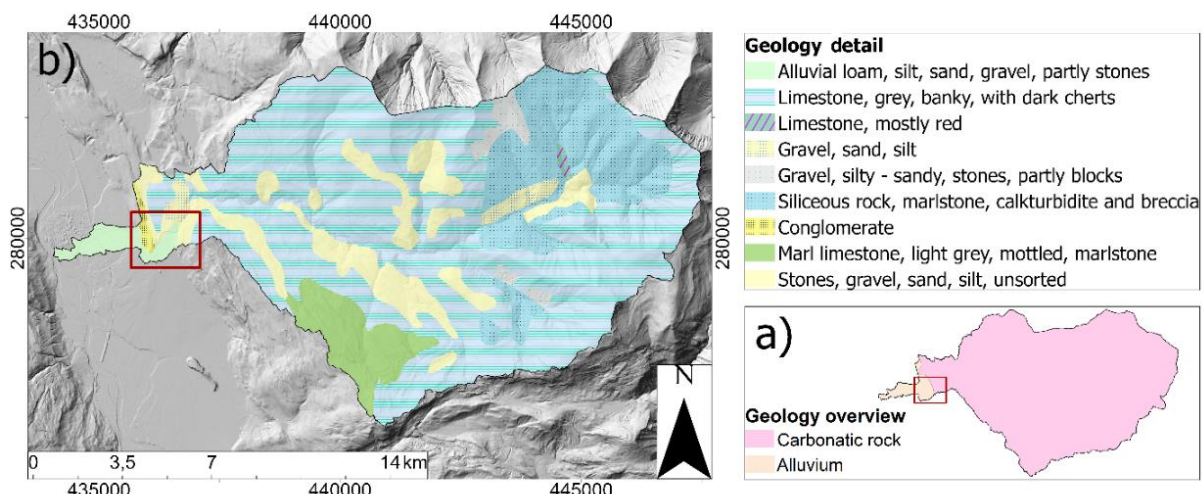
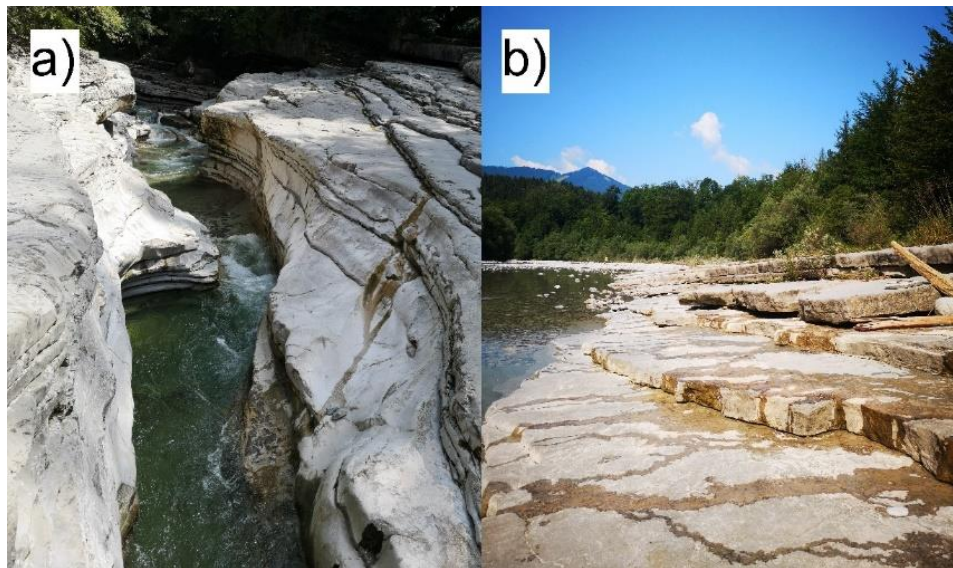


Figure 6: Geology in the Taugl River catchment. a) Overview map and b) detail map showing the geological setting within the study area (red rectangle) (data source: KM200 Salzburg – Geologie, Geologische Bundesanstalt; DEM 2013, state government of Salzburg).

### 3.2 Geomorphology

The Taugl River can develop almost without restraints, whereby it dynamically shapes the landscape it flows through (Tourismusverband Bad Vigaun, 2021). Within the AOI, mechanical bedrock erosion as well as sediment transport and deposition within the alluvium lead to the alteration of the riverine landscape. At the transition between the gorge and the alluvial segment, the gently tipping limestone beds are progressively buried by alluvium (Guttmann, 1997). However, mechanical erosion can only be initiated if the bedrock is not covered. For removing alluvial layers, flood events that are capable of uncovering the bedrock for a certain period of time are required. This may lead to erosive processes such as abrasion and plucking (Hurst et al., 2021), which are both observable within the study area.



*Figure 7: Mechanical bedrock erosion observed in the AOI. a) abrasion at the transition between the gorge and the alluvial segment and b) plucking limestone beds of the Oberalm formation before they are partly buried by alluvium. Photos taken in June 2021.*

Abrasions can be primarily observed in the narrow slot canyon (Figure 7a). The impact of smaller particles in suspension causes a smoothing effect via breaking off sharp edges and corners (Whipple et al., 2013). In contrast, plucking, the removal of entire blocks along intersection joint planes or banks (Kim et al., 2006, Venditti et al., 2014, Lamb et al., 2015, Larsen and Lamb, 2016, Hurst et al., 2021), can be observed well within the AOI. Especially the transition zone between the gorge and the alluvial cone, where the gently tipping bedrock is progressively covered with an alluvial layer, is susceptible for this erosive process (Figure 7b). Here, as well as in a smaller river section in the middle of the AOI, limestone beds are partly exposed at the surface. Depending on the discharge rate, the bedrock may also be uncovered in other areas. In comparison to abrasion, plucking appear in general less frequent but more efficient since a higher shear stress is required for the block entrainment (Dubinski and Wohl, 2013, Whipple et al., 2013, Hurst et al., 2021). Thus flood events, which frequently occur in the Taugl River, favour the initiation of plucking (Baynes et al., 2015). Crucial for the block entrainment is the rock strength and the joint orientation (Lamb and Dietrich, 2009). But also the protrusion height of blocks above the channel plays an important role (Lamb et al., 2015, Lapotre et al., 2016). The flat and jointed limestone beds favour thereby erosion by plucking (Rettenbacher and Rettenbacher-Höllwerth,

1982). This shows that the geological conditions have a significant influence on the fluvial processes and forms within the AOI (Spiegler, 1971, Leditzky, 1990).



*Figure 8: View from a gravel bank onto the main channel and the adjacent floodplain, partly covered with vegetation. Photo recorded in spring 2019.*

Within the alluvial cone, sediment transport and deposition determine the geomorphodynamics since alluvial rivers are self-formed (Church, 2006, Rhoads, 2020). In its gravel-bed, the Taugl River has developed a braided river system. This kind of river pattern is characterized by a system of multiple channels that are converging and diverging. Spatial and temporal variations in sediment transport capacity have caused a complex system of erosion and deposition as well as the establishment and dislocation of riverine bars (Bridge, 2016). Prerequisite for the development of a braided system is the supply of non-cohesive material or the emergence of the gravel-bed (Surian, 2015). Bars of different sizes separate the stream of the Taugl River (Figure 8). Due to erosion and deposition, they can generally alter in a short period of time (Bridge, 2016). Vegetation has established on some ones as well as on some parts of the floodplain (Tourismusverband Bad Vigaun, 2021). Their roots can significantly affect the channel geometry due to strengthening of material and reducing the flow velocity nearby banks (Millar, 2000, Gracchi et al., 2021). During periods with lower discharge rates e.g. due to increasing temperature within summer months, some channels may dry for a certain period of time. In general, the braiding intensity thus varies with the discharge rate (Peirce et al., 2018).

### **3.3 Climate and discharge**

Rivers morphology expresses the linkage between climate and erosion. Since precipitation is the main source of water, variations in its amount heavily affect the transport capacity of the rivers (Deal et al., 2018). For this reason, an analysis of the climate within the Taugl catchment is important. The hydrographic service of Salzburg provided temperature and precipitation data with different temporal resolutions from their measurement station St. Koloman. Temperature data are available since July 2004 and precipitation data since January 1993. However, a continuous measurement series does not exist due to some data gaps. The St. Koloman station is located about 6 km east of the AOI. Because of its position at an altitude of 1000 m, the data represents the climate in the Taugl catchment area well. In

addition, data regarding both the water level and the discharge of the Taugl River were provided. The gauging station was installed some tens of meters upstream the Römer Brücke in 1977, but was demounted in August 2015.

### Temperature and precipitation

The temperature data of the St. Koloman measuring station reflect the typical temperature trend of a seasonal climate (Figure 9). The highest mean monthly temperatures occur in July and August and reach approximately 16 to 18 °C. The maximum monthly average was reached in June 2019 with about 19.5 °C, which is just slightly higher than the monthly average temperature in July 2006 with 19.4 °C. The temperature decline from autumn to winter is mostly constant with only rare significant increases (e.g. in 2006 or 2017). The average temperatures are lowest from December to February. February 2012 was the coldest month in the measurement series with an average monthly temperature of about -6.6 °C. The value rise from spring to summer is also mostly constant. When analysing the annual average temperatures, a slightly increasing trend is noticeable. Nevertheless, it must be taken into account that the measurement series only includes 15 years (2005 - 2020) and also contains gaps (2009, 2010). Therefore, this measurement period does not provide a representative picture of the long-term temperature development in the study area making conclusions about climate change inaccurate. However, the last two years, 2019 and 2020, were the warmest with mean annual temperatures of just below 9 °C.

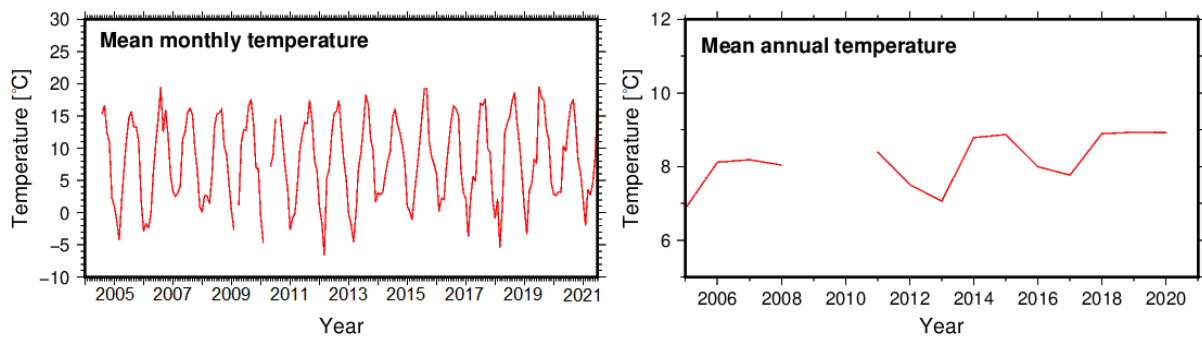


Figure 9: Mean monthly and annual temperature [°C]. Measured at the St. Koloman station during a period from 1.7.2004 to 1.7.2021. The pattern is typical for a seasonal climate. However the data contain some gaps.

The total annual precipitation from 1993 to 2021, recorded at the St. Koloman gauging station, reached its maximum in 1995 with about 2005 mm. The minimum was observed in 2003 with a yearly precipitation of only 1212 mm (Figure 10). Due to measurement gaps, there is no total precipitation data for the years 2004 and 2010. Based on this relatively short monitoring period, no clear rising or falling trend can be identified. Figure 10 also shows the total precipitation per month in a time series from 1993 to July 2021. The comparatively high values within the years 1997, 2002 and 2007 are striking. The total maximum occurred in July 1997 with 477 mm. Conversely, November 2011 was extraordinarily dry with no measured precipitation.

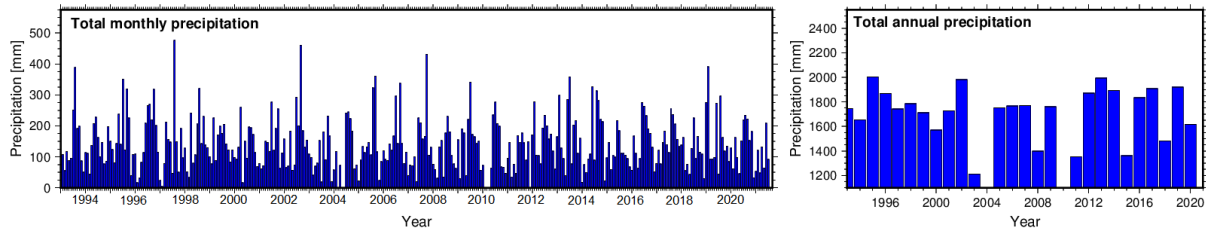


Figure 10: Total monthly and annual precipitation [mm]. Measured at the St. Koloman station during a period from January 1993 until July 2021. November 2011 is not a data gap but shows no precipitation.

## Discharge

When analysing the discharge data, it must be taken into account that the zero level of the gauging station has been lowered by about 20 m over the years (from 1977 at 520 m to about 502 m since 1988). The discharge measurement ended with the demounting of the gauging station in August 2015. In 2009, the maximum mean annual of water level and discharge rate was measured (Figure 11).

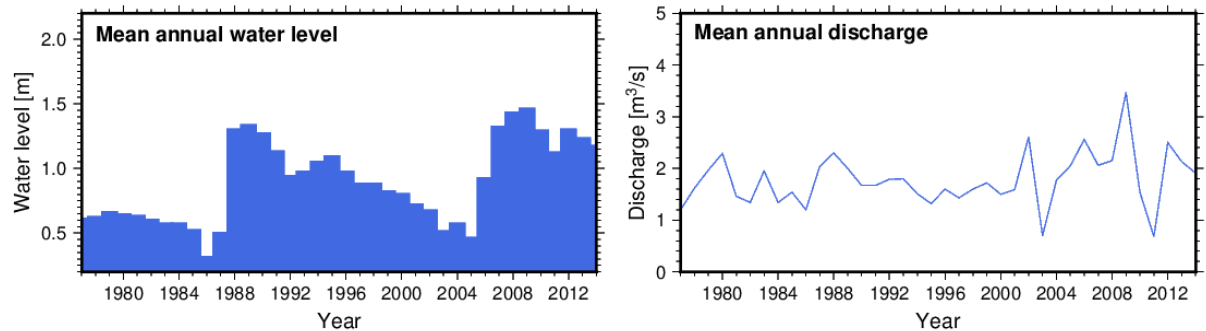
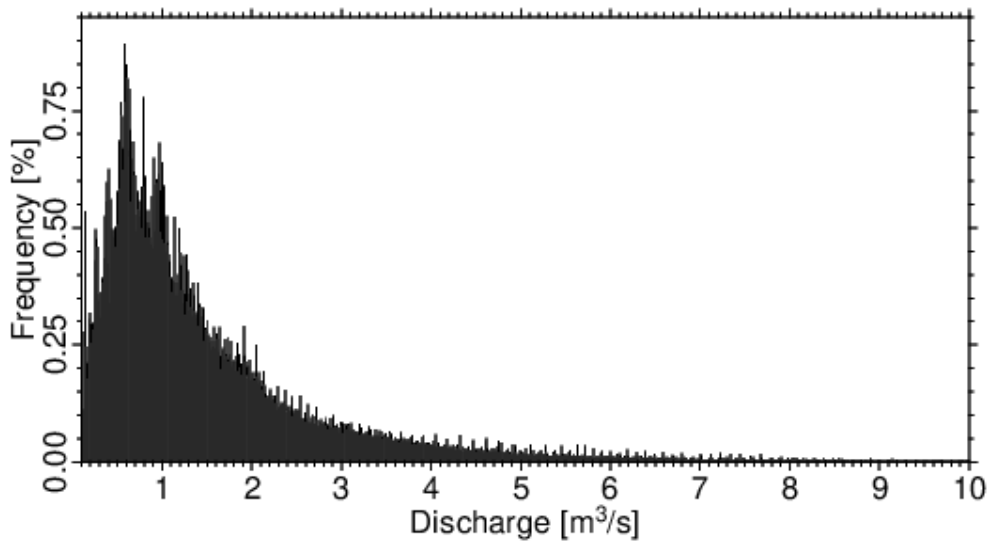


Figure 11: Averaged annual water level [m] and discharge [ $\text{m}^3/\text{s}$ ]. Measured at the gauging station Römer Brücke during a period from 1977 to 2014.

The average water level is about 147.6 m with a mean discharge of 3.47  $\text{m}^3/\text{s}$ . The minimum water level was measured in 1986 with only about 32 m. The lowest annual averaged discharge rate was recorded in 2006 with 0.68  $\text{m}^3/\text{s}$ . Despite the declining trend in the last few years, a slight overall increase in the annual mean water level and discharge rate can be observed. When analysing the data with a higher temporal resolution, the monthly maximum of the mean water level was measured in April 2009 with 1.71 m. In the same month, the discharge rates reached their maximum with an average of 13.12  $\text{m}^3/\text{s}$ . The monthly minimum of both parameters was measured in November 2005. The mean water level was just 0.13 m and the averaged discharge only 0.05  $\text{m}^3/\text{s}$ . In addition, the hydrographic service of Salzburg provided discharge data in an even higher temporal resolution. Thereby, the values were measured in a 15 min interval during a period from 1 January 1977 to 27 November 2006. Based on these records, it became apparent that the most frequently measured discharge rate is approx. 0.4  $\text{m}^3/\text{s}$ . The minimum value is 0.1  $\text{m}^3/\text{s}$  and the maximum approximately 75  $\text{m}^3/\text{s}$  (Figure 12).



*Figure 12: Section of the histogram showing the discharge rates in relation to the frequency. The data was recorded by the hydrographic service of Salzburg during a period from 1.1.1977 to 27.11.2006 (measurement interval 15 min). Although magnitudes of up to almost 75 m<sup>3</sup>/s were recorded, the section only shows the discharge rates of up to 10 m<sup>3</sup>/s, as the flood events with higher magnitudes occur at very low frequencies and are therefore hardly recognisable.*

### 3.4 Flora and fauna

The natural river dynamic is prevailed since there are hardly any riverbank and –bed obstructions. Thus, the Taugl River can develop almost without restraint, offering young habitats in the adjacent landscape (Janitz, 2012). Intact riverine landscapes with extensive gravel bars are a rarity in the province of Salzburg. Therefore, the AOI is part of an European natural reserve called Tauglgries (Janitz, 2012, Tourismusverband Bad Vigaun, 2021). The Römer Brücke is also marking the upstream limit of the Tauglgries, but with an extend of 2.4 km it stretches further downstream than the AOI (Figure 13) (Janitz, 2012). Since 2012, the total area of the natural reserve measures 50.65 ha. The Tauglgries is thus part of the European protected area network Natura 2000, which aims to preserve different rare habitats, e.g. alpine rivers with herbaceous riparian vegetation (Tourismusverband Bad Vigaun, 2021). In addition, rare animal species should also be protected. In order not to disturb the rare birds, which breed in the gravel, there is a temporary prohibition on entering the gravel area in parts of the Tauglgries from the first of April to the end of July (Janitz, 2012).

Rivers are important habitats for flora and fauna (Woodget et al., 2017). The correlation between vegetation and river morphodynamics is determining for the development of the river geometry as well as for geomorphological processes, which can be observed particularly well in the AOI. The establishment of vegetation is primarily dependent on soil suitability, water availability but also on the river regime (van Dijk et al., 2013). Sprouting, early growth and survival are strongly determined by discharge variability because both flooding and droughts affect the development of vegetation (Caponi et al., 2019). Thus, the ecological situation in the AOI is continuously changing, depending on flood frequency (Tourismusverband Bad Vigaun, 2021).

One of the pioneer plants are purple and lavender willows. They represent the plants from the first stage of an alluvial forest, with habitats on the gravel banks above the waterline. The willows are frequently

affected by flooding, but due to their high resistance they keep growing back (Janitz, 2012, Tourismusverband Bad Vigaun, 2021). Moreover, herbaceous and mountain plants are pioneers, since they develop on the frequently renewing soils. Alluvial forests have developed on both channel sides (Tourismusverband Bad Vigaun, 2021). The majority of adjacent forests are separated from the Taugl River by a break-off edge up to several meters. Those forests grew originally only slightly above the water level and referred to riparian forests. However, the removal of great amounts of gravel over about 40 years led to the lowering of the channel bed and to the decoupling of the forests. Thus, the typical renewal of riparian vegetation by flooding remained absent and the forests were able to develop into more mature stands (Janitz, 2012). Beside natural ravine and hillside forests, a beech forest has developed (Tourismusverband Bad Vigaun, 2021). Within the woods undergrowth, rare and protected flowers grow, e.g. the lady's slipper (orchid) (Tourismusverband Bad Vigaun, 2021). However, due to the establishment of vegetation in the AOI, wood is supplied to the riverine system. The entrainment of driftwood is controlled e.g. naturally by tree mortality, flooding or supply from tributaries (Welber, 2013). In addition, floods can (re-) mobilize deadwood that is already deposited in the riverbed (Hartlieb, 2015). As a result, branches or uprooted trees interact with the flow, influencing the direction, velocity and thereby the channel geometry (Welber, 2013, Kramer and Wohl, 2015).

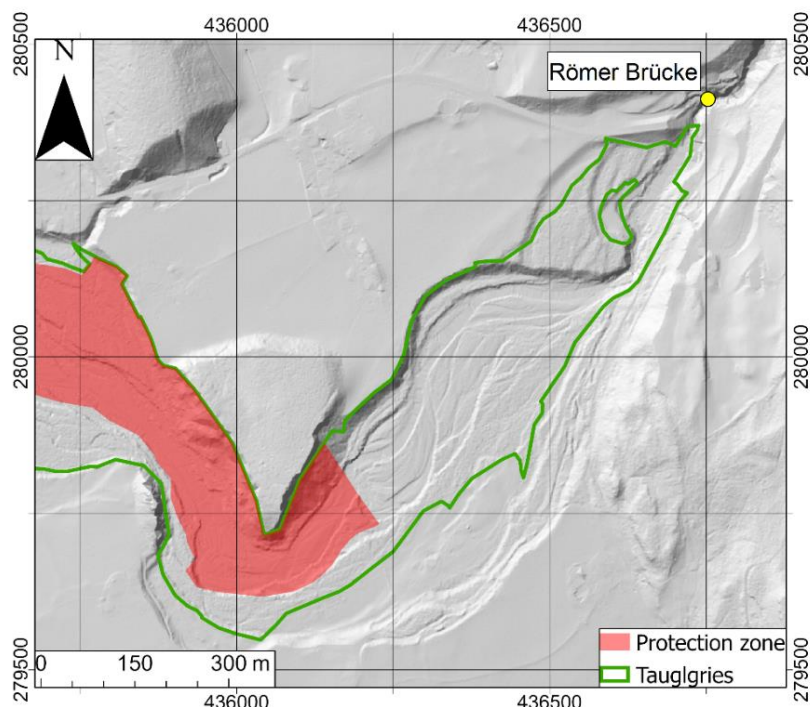


Figure 13: Tauglgries (marked in green) and European natural reserve (red area). The Römer Brücke (yellow circle) marks the upstream limit of the study area (data sources: Europaschutzgebiete FFH-RL; Europaschutzgebiete Schutzonen and DEM 2013 - all data provided by the state government of Salzburg )

## 4 Methods

In order to monitor the dynamically changing landscape, photogrammetry was used. Alterations in the riverine landscape were thus documented via DEM and orthophoto generation. By analysing the derived remote sensing data in dedicated areas along the river course, the results of the second method of this thesis, hydraulic modelling, are validated. Based on numerical simulations of single floods with varying magnitude several critical discharges were identified. This also required the prior calculation of thresholds for initial sediment motion and plucking. In order to subsequently present the results, maps and diagrams were generated by using the Generic Mapping Tools (GMT). The basemap for all created maps is a hillshade derived from the DEM 2013, provided by the state government of Salzburg.

### 4.1 Photogrammetry

Unmanned aerial vehicles (UAV) photogrammetry became a popular method in fluvial geomorphology in the last years (Gracchi et al., 2021). Through the developments in the performance of drones and the simultaneous advancements in photogrammetry new possibilities in remote sensing of rivers have emerged (Woodget et al., 2017). This makes acquiring high-resolution images and topographic data of riverine landscapes, in a flexible and cost efficient way, possible (Woodget et al., 2017, Gracchi et al., 2021). Digital photogrammetry methods enable a topographic analysis and the derivation of different products, like orthophotos or digital elevation models (DEM), fast and affordable (Gracchi et al., 2021). Moreover, the acquired topographic data serve as input for numerical models, also in the field of fluvial geomorphology (Brasington et al., 2012). The range of applications of photogrammetry has increased in recent years and it provides solutions for a wide variety of problems, such as quantifying fluvial erosion and deposition or determining substrate size in order to calculate the channel roughness (Brasington et al., 2012, Woodget et al., 2017). Long term monitoring of fluvial geomorphodynamics became more important than ever with respect to climate change and extreme events (Brasington et al., 2012). Especially in multi- temporal monitoring, UAV based photogrammetry provides a good alternative to traditional in situ measurements and is thus commonly used for analysing the alteration of riverine landscapes and the involved processes (Gracchi et al., 2021). In this study, UAV based photogrammetry was used in order to monitor the geomorphic changes within the riverbed. In the following chapter, a general overview of remote sensing using drones and digital photogrammetric techniques is given. This is followed by a description of how the surveys were conducted and how the collected data were processed.

#### 4.1.1 Drones and digital photogrammetry

Photogrammetry, the science of measuring in photos, is a remote sensing (RS) method to obtain quantitative and qualitative data from objects without being in physical contact with them (Linder, 2016). Thereby, the solar radiation reflected from the Earth's surface is detected, which makes it a passive RS method (Toth and Jutzi, 2017). In the past, satellites or aircrafts equipped with sensors were typically used for RS (Pajares, 2015). In recent years, advances in aviation and sensing technologies promoted the widespread use of UAVs (Pajares, 2015, Linder, 2016). A major advantage of these platforms is their comparatively greater flexibility and manoeuvrability. They are able to acquire data

in high spatial and temporal resolution based on their ability to fly in low altitudes and with reduced speeds (Pajares, 2015). In the field of fluvial geomorphology, e.g. space based systems are not well suited for frequent or flexible observations of small riverine landscapes because of their low temporal and spatial resolution. Thus, a quantitative as well as a qualitative analysis of alterations within the riverine landscapes can be better carried out by using frequent and cheap UAV based photogrammetry (Gracchi et al., 2021).

### **Components of drone systems**

Drone systems are composed out of at least one sensor that is mounted on an aircraft platform (Woodget et al., 2017). In so called multi-sensor systems, several sensors of identical or different types, such as multispectral cameras or small laser scanners, are installed. The sensor orientation can vary (Toth and Jutzi, 2017, Woodget et al., 2017). The functionality of the mounted photogrammetric cameras is basically the same as for amateur cameras. This shows that advances in photogrammetry are closely related to those in photography (Linder, 2016). Different kinds of drone platforms exist (Woodget et al., 2017). Their classification can be based on flight altitude, weight or on the distinction between fixed- and rotary wing systems (Nex and Remondino, 2014, Pajares, 2015, Woodget et al., 2017). The duration of the survey is always limited by the capability of the batteries (Pajares, 2015). When using fixed wing systems, comparatively longer flight times can be achieved with the same payload. In contrast, rotor supported platforms such as the quadro-, hexa- or octocopter can change their flight path and position more quickly and are therefore more flexible, even in difficult terrain. For this reason, these UAV platforms are preferably used for research purposes (Toth and Jutzi, 2017). Beside the sensor or camera and the platform, the third important part of a drone system is the navigation system (Toth and Jutzi, 2017, Woodget et al., 2017). GNSS (Global Navigation Satellite System) and MEMS (microelectromechanical) sensors are part of the so called Inertial Measurement Unit (IMU). This is used for navigation based on waypoints and for flight monitoring (Toth and Jutzi, 2017). In most cases, however, the orientation based on the sensor platform is only coarse, which is why georeferencing based on GCPs (Ground Control Points) is necessary (Nex and Remondino, 2014, Toth and Jutzi, 2017). During the survey, the platform is monitored by a Ground Control Station (GCS) (Nex and Remondino, 2014).

### **Geometrical basics**

The basis of the image recording is the model of the central projection of a pinhole camera (Toth and Jutzi, 2017). In order to reconstruct the scene and the coordinates of a point in the object space from the images, it is necessary to determine the position of the projection centre in relation to the image plane (inner orientation) and to the object space (outer orientation) (Linder, 2016, Luhmann and Maas, 2017). The geometry of the recorded images deviates from this ideal mathematical model of the central projection. This is caused by optical parameters, such as influences of the illumination (wavelength), medium (air, water, gas), lens (resolution), sensor (noise) and by camera internal signal processing (filter, colour mixing, compression). The parameters describing the divergence define the inner orientation of the projection centre (Figure 14a). The inner orientation defines the position of the projection centre to the image plane. The parameters include the position of the projection centre O' in the image coordinate system and the distortion errors. The position of O' results from the location of the

image main point  $H'$  ( $x'0, y'0$ ), which forms the perpendicular foot of  $O'$ , and the distance between the projection centre and the image plane, the camera constant  $c$  or the focal length  $f$ . Distortions are the result of varying degrees of refraction of solar rays of different wavelengths at the lens in the objective. The point  $P'$  thus deviates from the ideal position by  $\Delta x'$  and  $\Delta y'$ . These parameters, describing the inner orientation, can be determined by means of camera calibrations (Luhmann and Maas, 2017). The position of the camera at the time of taking the picture is called the outer orientation (Figure 14b) (Luhmann, 2010). It is determined by six parameters, where  $x, y, z$  represent the position of the projection centre in the coordinate system of the object space, Omega ( $\omega$ ), Alpha ( $\alpha$ ), and Kappa ( $\kappa$ ) the rotation angles of the  $x, y, z$  axes (Luhmann, 2010, Linder, 2016). For vertical recordings, so called nadir recordings,  $\omega$  and  $\alpha$  are  $0^\circ$ . If this is the case, the average image scale decreases with increasing height. A uniform scale can only exist for flat surfaces. Consequently, differences in relief lead to a varying scale, which means that it must be given as an average value or scale range (Linder, 2016).

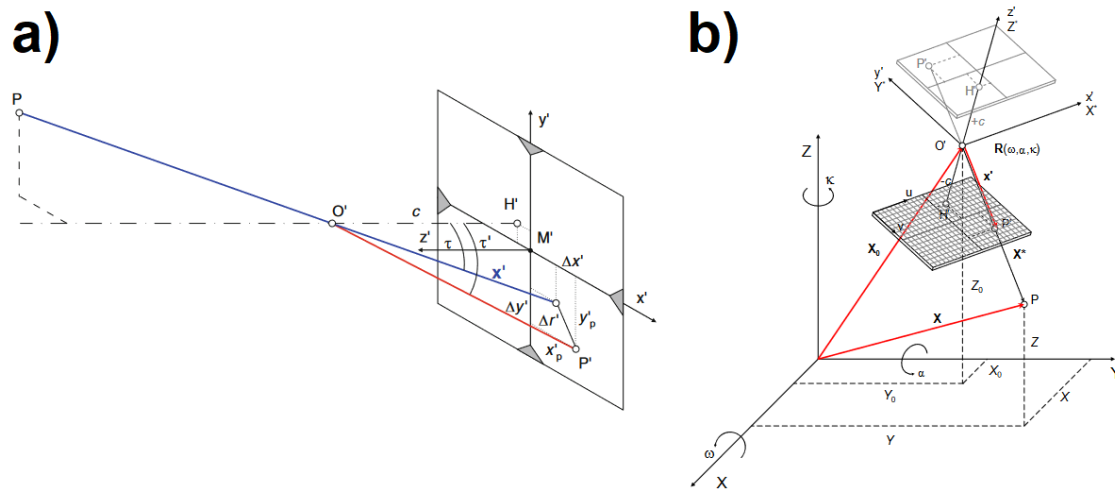


Figure 14: Geometrical basics of photogrammetry a) parameters of the inner orientation and/or the position of the projection centre to the image plane (Luhmann and Maas, 2017) and b) the outer orientation or the position of the projection centre to the object space (Luhmann, 2010).

For transferring the three-dimensional coordinates ( $x, y, z$ ) of a point in the physical object space into the two-dimensional coordinates ( $x', y'$ ) of the image plane, collinearity equations are used (13a and 13b). These include all parameters of the inner and outer orientation and are based on concepts of translation and rotation. The variable  $z$  is derived from the negative value of the focal length. For each of the three axes there is a rotation value ( $r_{123}$ ). These formulas are also the basis of linear systems of equations that can be used, for example, to calibrate the camera using several points with known coordinates in the object space (spatial backstepping) (Luhmann, 2010).

$$x' = x'_0 + z' \frac{r_{11}(X - X_0) + r_{21}(Y - Y_0) + r_{31}(Z - Z_0)}{r_{13}(X - X_0) + r_{23}(Y - Y_0) + r_{33}(Z - Z_0)} + \Delta x' \quad (13a)$$

$$y' = y'_0 + z' \frac{r_{11}(X - X_0) + r_{21}(Y - Y_0) + r_{31}(Z - Z_0)}{r_{13}(X - X_0) + r_{23}(Y - Y_0) + r_{33}(Z - Z_0)} + \Delta y' \quad (13b)$$

### Photogrammetric survey method

In order to obtain three-dimensional information from the images, the evaluation of at least two overlapping images is necessary. In general, a distinction can be made between two-image methods, such as classical stereo photogrammetry, and automated multi-image methods (Linder, 2016). In this study, Structure from Motion (SfM) was used as the survey method (Figure 15) (Westoby et al., 2012). This is an automated multi-image method that extracts the three-dimensional structures from multiple overlapping images of a moving camera (Westoby et al., 2012, Carrivick et al., 2016). A series of key points is identified by using the Scale Invariant Feature Transform (SIFT) algorithm in order to search for the same features in different images. Afterwards, so called bundle adjustments ensure that the positions of the individual images are relative to each other (Favalli et al., 2012, Nex and Remondino, 2014). This automatically generates a sparse 3D point cloud from the recorded scene, which can be densified using Multi- View Stereo (MVS) methods (Carrivick et al., 2016). However, the point cloud is situated in an image-space coordinate system and must thus be transformed into a real object-space system (Westoby et al., 2012). In most cases this transformation into an absolute coordinate system is achieved by using GCPs whose object space coordinates are known (Westoby et al., 2012, Carrivick et al., 2016). Normally, targets with a well-defined centre and a high contrast to the surrounding environment are distributed in the AOI before the survey. Their exact position is recorded by using GPS. However, it is also possible to define GCPs at a later stage. For this purpose, outstanding features are selected in the point cloud, whose coordinates are recorded during another ground survey (Westoby et al., 2012).

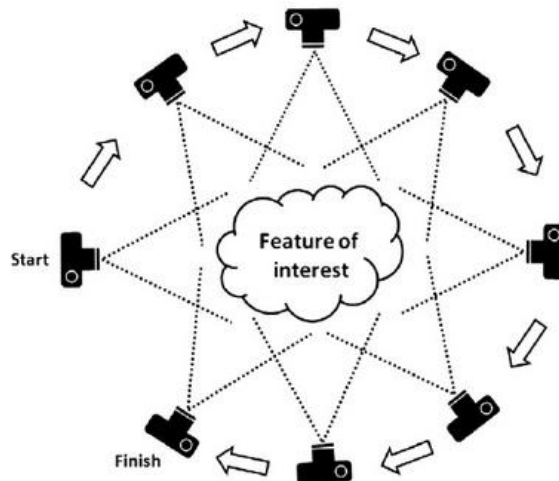


Figure 15: Structure from Motion (SfM) photogrammetric survey method. This automated multi-image method extracts the three-dimensional structures from multiple overlapping images of a moving camera (Westoby et al., 2012).

#### 4.1.2 Data acquisition

Several surveys were carried out over the AOI in order to obtain multi temporal data regarding the morphological changes within the riverbed. The flights were performed with a twinFOLD GEO drone (open category: UAS- class C3) (Figure 16). The data acquisition required a prior planning phase. For each flight, an optimal route was created by using the open source software *AurduPilot's Mission Planner*. Further, the camera parameters, flight altitude and the Ground Sample Distance (GSD) were

determined. When choosing the flight altitude, it was taken into account that the scale and the focal length depend on it (Nex and Remondino, 2014). By defining the waypoints, the centre points from a camera perspective, a flight plan was generated (Toth and Jutzi, 2017). A sufficiently large longitudinal and transversal overlap of at least 60 % to a maximum of 80 % was selected. Since the aim of the survey was to create accurate models in order to analyse the dynamic morphological changes, a high degree of overlap and a low GSD were necessary in order to obtain high resolution images (Nex and Remondino, 2014). The flight altitude varied thus between 70 to 80 meters. As a result, the surveys were more precise but also more time consuming. Since the flight duration was limited by the energy supplied by the rechargeable battery, the study area had to be covered by several flight plans (Toth and Jutzi, 2017).

During the preparations, the distribution of the GCPs, which were needed for georeferencing and scaling of the point cloud, was also planned (Carrivick et al., 2016). At least three GCPs are needed to ensure satisfying referencing results (Westoby et al., 2012, Nex and Remondino, 2014, Carrivick et al., 2016). But in order to achieve optimal results, 8 to 10 GCPs were distributed widely throughout the study area. Their exact locations were determined by using GPS (Carrivick et al., 2016). The UAV based survey flights were usually performed semi automatically. The data acquisition and the navigation along the defined waypoints were carried out automatically due to the implemented GNSS unit. During the flight, the platform was constantly monitored by the GCS, which displayed the real time flight data such as flight speed, altitude, battery status, etc. For ensuring safe take- off and landing on the rough gravel surface it was performed manually (Nex and Remondino, 2014).



Figure 16: TwinFOLD GEO drone (open category: UAS- class C3) was used for the surveys.

#### 4.1.3 Data processing

The collected data were processed with the commercial software Agisoft Metashape Professional with the aim to create orthomosaics and DEMs. A preprocessing was carried out beforehand in which the images were assessed with regard to their quality. Images with strong reflections or shadows, as well as with greatly varying brightness, were sorted out as they are unsuitable for photogrammetric evaluation (Carrivick et al., 2016). Processing in Agisoft Metashape Professional followed the workflow shown in Figure 17 for generating three-dimensional models of the visible surface as point clouds, polygonal models (mesh), DEMs and orthomosaics (Gracchi et al., 2021).

After the images were imported into Agisoft, they first had to be aligned with a maximum resolution (Agisoft, 2020). Homologous points on different images were identified and the camera positions were reconstructed (Favalli et al., 2012, Agisoft, 2020). The output was a sparse point cloud (Westoby et al., 2012). The definition of the coordinate system (WGS 84 EPSG: 4326) was automatically done by adding the GCPs, also called marker, since Agisoft assumes that their reference system matches the camera coordinates. As a result, all generated outputs were referenced to this coordinate system by default. Markers have to be set manually. However, since the positions of the GCPs were recorded in the field by using GPS, they were imported as a CSV file. After refining the marker location, the camera alignment parameters (inner and outer orientation) were optimised to minimise the projection and alignment errors. After refining the alignment, dense point clouds could be generated. From these, the vegetation was cut out and mesh models and the DEMs were derived. During rasterization to generate the DEM, both projection and resolution can be modified. Orthomosaics were generated from orthorectification of the original images. The modelled surface was based on the previously created DEMs. Using the option ‘*Fill Holes*’ allowed the creation of a continuous mosaic. Finally, all derived products were exported in the required format (Agisoft, 2020).

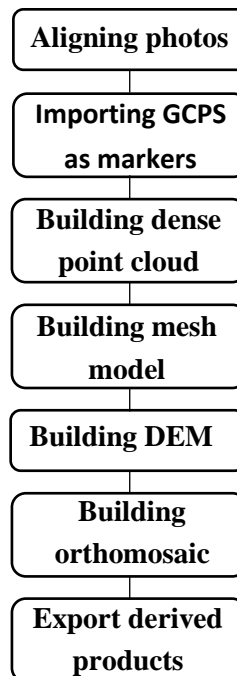


Figure 17: Workflow showing the main processing steps of aerial images using Agisoft Metashape Professional .

## 4.2 Hydraulic modelling

In the field of fluvial geomorphology, numerical models have become an important method for analysing key parameters and for understanding the alteration of riverine landscapes (Coulthard and Van De Wiel, 2013). In recent decades, progress in technology have led to the establishment of various two- and three- dimensional models (Darby and Van de Wiel, 2003, Coulthard and Van De Wiel, 2013). Because of the spatial and temporal multidimensionality, numerical models improved the physical description of fluvial processes (Kondolf et al., 2016). They vary in time, scale, complexity, algorithms

and in the reality to be simulated. A successful numerical model serves as a virtual laboratory in which the system variables are controlled by the developer. Thus, problems of traditional methods in fluvial geomorphology, like monitoring landscape evolution over long periods of time or over large areas and observing multiple interacting variables in a dynamic system, can be solved (Coulthard and Van De Wiel, 2013). In numerical models, time is discretized into appropriate steps (Kondolf et al., 2016). Spatial extent and resolution is defined by computational grids on which physical parameters like flow velocity, water depth or roughness are simulated as a series of discrete values (Darby and Van de Wiel, 2003, Kondolf et al., 2016).

#### 4.2.1 Numerical models in fluvial geomorphology

Simulating spatial and temporal alterations within streams is commonly performed by so called Computational Fluid Dynamic (CFD) models, which are in general based on the Cartesian coordinate system (x,y,z) (Coulthard and Van De Wiel, 2013, Kondolf et al., 2016). Using CFD models allows the calculation of different parameters, like water depth, flow velocity ( $u$ ) or basal shear stress (Coulthard and Van De Wiel, 2013). Generally, fluid motion is based on the assumption of mass and momentum conservation. Mass conservation means that no water is generated or destroyed during the flow (14) (Nelson et al., 2003, Coulthard and Van De Wiel, 2013).

$$\frac{\partial u_x}{\partial x} + \frac{\partial u_y}{\partial y} + \frac{\partial u_z}{\partial z} = 0 \quad (14)$$

The principle of conservation momentum is based on Newton's second law (law of motion) which states that variations in flow velocity are caused by the influence of external forces. Within a fluvial system those forces are gravitational acceleration ( $g$ ), pressure ( $p$ ), shear stress ( $\tau$ ), friction and the Coriolis force. The Navier- Stokes equations (3D) physically describe this principle:

$$\rho \left( \frac{\partial u_x}{\partial t} + u_x \frac{\partial u_x}{\partial x} + u_y \frac{\partial u_x}{\partial y} + u_z \frac{\partial u_x}{\partial z} \right) = - \frac{\partial p}{\partial x} + \frac{\partial \tau_{xx}}{\partial x} + \frac{\partial \tau_{xy}}{\partial y} + \frac{\partial \tau_{xz}}{\partial z} + F_x \quad (15a)$$

$$\rho \left( \frac{\partial u_y}{\partial t} + u_x \frac{\partial u_y}{\partial x} + u_y \frac{\partial u_y}{\partial y} + u_z \frac{\partial u_y}{\partial z} \right) = - \frac{\partial p}{\partial y} + \frac{\partial \tau_{xy}}{\partial x} + \frac{\partial \tau_{yy}}{\partial y} + \frac{\partial \tau_{yz}}{\partial z} + F_y \quad (15b)$$

$$\rho \left( \frac{\partial u_z}{\partial t} + u_x \frac{\partial u_z}{\partial x} + u_y \frac{\partial u_z}{\partial y} + u_z \frac{\partial u_z}{\partial z} \right) = - \frac{\partial p}{\partial z} + \frac{\partial \tau_{xz}}{\partial x} + \frac{\partial \tau_{yz}}{\partial y} + \frac{\partial \tau_{zz}}{\partial z} - \rho g + F_z \quad (15c)$$

Where  $\rho$  is the water density and  $F$  represents all other acting forces. However, some research questions only require 2D models (Coulthard and Van De Wiel, 2013). For this reason, the 3D Navier- Stokes equations can be reduced into a two- dimensional depth- averaged form, also known as Saint- Venant or shallow water equations (16) (Coulthard and Van De Wiel, 2013, Hergarten and Robl, 2015). Those are based on the assumption of a horizontal water layer which allows to ignore the vertical velocity but using depth averaged horizontal velocities ( $v_h$ ) causing a hydrostatic pressure instead of a vertical one (Grenfell, 2015, Hergarten and Robl, 2015). Thus, the horizontal pressure vector is similar to the gradient of the water layer. Shallow water equations can be expressed as:

$$\frac{\partial}{\partial t} v_h + (v_h * \nabla) v_h = gs - \frac{\tau}{\rho h_v |v_h|} \quad (16)$$

Where  $\nabla$  is the two-dimensional gradient operator. The second part of equation is a friction term, considering the shear stress  $\tau$  on the channel bed. The vertical flow depth is expressed by  $h_v$  (Hergarten and Robl, 2015).

#### 4.2.2 Model development

In this study, various single flood scenarios were simulated with the open source software system Gerris Flow Solver (GFS). GFS was developed by Stephane Popinet for numerical modelling of fluid mechanics (Keen et al., 2013, An et al., 2015). It uses the C programming language and contains a variety of object oriented functions that enables the realization of new models (Popinet, 2011, Keen et al., 2013). Initially, GFS was established in order to solve incompressible Euler equation, but was then enhanced to multiphase Navier-Stokes equations (15), spectral wave models and also shallow water equations (SWE) (16) (An et al., 2015). Today, several features for solving time dependent problems and linear as well as non-linear SWE are available (Keen et al., 2013). GFS utilizes dynamic adaptive mesh refinement (AMR) methods by relying on semi structured quadtree (2D) and octree (3D) mesh (Popinet, 2003, Popinet, 2011, Keen et al., 2013, An et al., 2015). This means that the simulation domain is spatially subdivided into hierarchically structured squares (or cubes in the case of a third dimension), following the scale and temporal development of the flooding (Popinet, 2003). By using this cell cutting method, high computational efficiency is achieved (An et al., 2015). AMR organize grids of different resolutions hierarchically by using established algorithms. The quadtree (or octree) method operates on a variety of levels of refinement based on finite-difference operators (Popinet, 2003). A variety of analytical functions can be implemented as modules. For simulating flooding in the Taugl River, the module *GfsRiver* was used, which is a two dimensional nonlinear SWE (Keen et al., 2013).

Different constant discharge rates with varying magnitudes were simulated. To ensure that a steady state can develop, the simulation was executed over a sufficiently long period of time, depending on the magnitude of the simulated discharge rate (Larsen and Lamb, 2016). An essential part of the physically based flood simulations conducted in this thesis are the thresholds for incipient sediment motion and plucking. Both critical values must be computed before implementing them into an executable flood simulation file.

##### 4.2.2.1 Calculation of thresholds for initial sediment motion and plucking

The calculation of both threshold values followed the approach of Larsen and Lamb (2016). Nevertheless, a calibration to the specific conditions within the AOI was required.

###### Threshold for incipient sediment motion

The determination of a critical value for incipient sediment motion requires the median grain size  $D_{50}$  (Kirchner et al., 1990, Johnson, 2014, Lamb et al., 2015). Thus, the intermediate diameter of clasts along representative profiles were measured. Moreover, a calculated roughness map, derived from the high resolution combined DEM, was also used to determine the median grain size, because hydraulic roughness is often calculated as an equal parameter to the riverbed grain size (Noss and Lorke, 2016).

The resulting median grain sizes were subsequently compared in order to evaluate the suitability of high resolution DEMs for grain size analyses.

The calculation of the threshold was based on the constant critical Shields number  $\tau_c^*$  for low gradient gravel- bed rivers. Thus,  $\tau_c^* = 0.045$  and the ascertained  $D_{50}$  were substituted into equation (9) (Larsen and Lamb, 2016). Since limestone is predominant in the study area, a corresponding value of 2500 kg/m<sup>3</sup> was used as sediment density  $\rho_s$  (Table 1) (Selby, 1993). Furthermore, the water density  $\rho$  (1000 kg/m<sup>3</sup>) and the gravitational acceleration  $g$  (9.81 m<sup>2</sup>/s) were required (Scherler et al., 2017). Once the critical shear stress for initial sediment motion has been calculated, it was implemented in the simulation file by dividing the applied bed shear stress in each cell of the domain by the threshold. Thus, the areas where incipient motion occurs can be visualized. In addition, the critical value and the exerted bed shear stress along the profiles and at the stations during different discharge values are to be compared. As a result of simulating flood events with several magnitudes and the analysis of the derived ratios between critical and basal shear stress, a threshold discharge for geomorphic activity of the river was determined. The river becomes geomorphological active by exceeding this discharge threshold.

### Critical shear stress for plucking of limestone bedrock

Mechanical bedrock erosion within the AOI is primarily driven by plucking the limestone beds. Here, block entrainment is a result of sliding. Thus, the determination of the critical shear stress for plucking  $\tau_{pc}$  is based on equation (11) (Lamb et al., 2015). The channel bed angle ( $\theta$ ) was set to 4° considering the overall inclination. The friction angle was assumed to be 30° with regard to the common value range (27° – 35°) of wet limestone (Selby, 1993). The ratio between block protrusion height and length ( $P/L$ ) was determined by measuring a representative amount of blocks in the field. The hydraulic lift  $F_L^*$  is a constant value of 0.85 (Lamb et al., 2015). The dimensionless local drag coefficient  $C_D$ , which depends on the Reynolds number, was set to a constant value of 1 (Lamb et al., 2015). Thereby, the effects of sediment shape and orientation as well as the roughness in relation to the flow conditions are only approximated (Hurst et al., 2021). This constant value was based on the assumption that no variation occurs, if  $Re > 100$  (Lamb et al., 2015). As experimental studies have shown, this is the case for most natural rivers (Hurst et al., 2021). The ratio between flow velocity and shear velocity ( $u/u_*$ ) was identified based on samples from flood simulations. Unfortunately, sidewall stress is difficult to determine and no constant value exists (Larsen and Lamb, 2016). Therefore, the critical Shields number for block entrainment by sliding was determined with a range of sidewall stresses based on field observations. By using equation (11), a lower and an upper critical Shields number  $\tau_{pc}^*$  for block entrainment has been calculated based on the described parameters. Through substituting the resulting values into equation (12) a range of critical shear stress for plucking of limestone bedrock could be derived. However, the average block size was also required, which was determined by measuring a representative amount of samples in the field. Finally, a comparison between the threshold range and the bed shear stress during different peak flows was conducted in order to determine a critical discharge and to identify potential areas for plucking.

#### 4.2.2.2 Setting up an executable flood simulation file

There are two main input files, which are needed for setting up the simulation file. A digital elevation model of the AOI as a physical representation of space (Darby and Van de Wiel, 2003) and a discharge time series file. Both files must be available in a Gerris readable format, thus the x, y, z coordinates of the DEM must be converted into a two dimensional, tree- indexed database (quadtree) called terrain database (Popinet, 2012). The DEM was provided by the state government of Salzburg and refer to the year 2013 with a spatial resolution of 1 m. In case of the discharge, a common grid file is required. Only one parameter file is needed for controlling the entire flood simulation (Robl, 2021). The executable flood simulation file used for this study can be found in the appendix. For setting up this file, four main steps (Figure 18) are needed that sequentially adapt the numerical model to real world conditions:

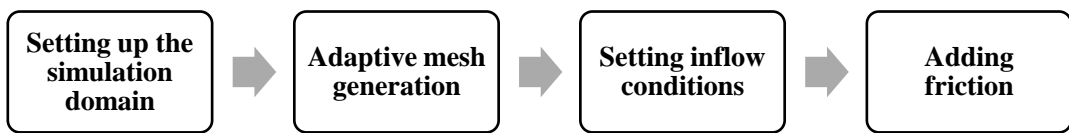


Figure 18: Main steps for setting up an executable parameter file for flood simulations using a module for 2D shallow water equations (*GfsRiver*) of the open source software system *Gerris Flow Solver* (*GFS*) developed by Stephane Popinet.

##### Setting up the simulation domain

At first, a simulation domain was created, the executive module *GfsRiver* was declared and the physical parameters were specified. By defining the gravitational acceleration in meters and seconds ( $9.81 \text{ m/s}^2$ ), these units are used as length and time units as defaults, respectively. Afterwards, the extent of the input DEM was defined as box size for the simulation. However, the bounding box must be adapted to the DEM by relocating the box's default centre to the lower left corner (*GfsGEdge*) and assigning the position (x,y) of this point to the lower left coordinates from the DEM (*MapTransform*). For stopping the simulation at an appropriate time, the last time step can be defined (*GfsTime*). Moreover, using the *GfsRiver* module requires the declaration of the boundary conditions (*GfsBox*) which is always the last code block of the parameter file (Popinet, 2012, Robl, 2021).

##### Adaptive mesh generation

Increasing computational efficiency was achieved by the implementation of an adaptive mesh (An et al., 2015). Refining is a step by step process in which the mesh is successively adapted and improved. Thus, a static mesh refinement was performed at first as the initial set up for subsequent adjustments. The prerequisite was the initiation of a terrain module (*GModule terrain*). Afterwards, the level of refinement was specified (*RefineTerrain*). Generally, a higher level causes an increase in the resolution but also in computing time (Popinet, 2012, Robl, 2021). A refinement level of 0 would be the root of a quadtree or the leaf cell since it has no children (Figure 19a and Figure 19b). Single cells may be the parents for four child cells. After starting at zero, new levels are reached by the discretisation of the cell into four children. Thus, Level 1 would be the separation of the square domain into four square cells (Popinet, 2003). After addressing the input DEM (*basename*), the terrain was refined to level 8. Thus, 256 x 256 square cells were defined (Popinet, 2012).

The first goal of optimizing the mesh refinement was to only define a high spatial resolution in relevant areas. This causes a reduction in the total number of cells and thereby a decrease in computational time. Since the position of water source ( $x, y$ ) represents a crucial area, a comparatively higher resolution was assigned to a circular area (25 m radius) around the inflow point. By definition, the level of refinement within the circle is 10 and outside 8 (Popinet, 2012, Hurst et al., 2021).

Until now, only *static mesh refinement* was performed (Popinet, 2012). Using *adaptivity* means, the spatial resolution is frequently adapting with respect on the development of the flood with time (An et al., 2015), causing an optimization in resolution and a decrease in computational time. Beside the inflow zone, all water covered areas are important for flood simulations. Consequently, the spatial resolution in wet areas should be significantly higher than in dry ones. This was achieved with mesh adaptivity (*AdaptFunction*). Under the condition that cells contain fluid, the mesh should be adapted in each time-step until the specified maximum level of refinement (9) is reached (Popinet, 2012). The distinction between wet and dry is based on a cost function (water depth  $>$  DRY), defining all areas as wet if the water depth is higher than a constant value specified by the variable  $DRY = 1e^{-3}$ . This means, if the water depth is less than about 1 mm, cells are counted as dry. In the case of higher depth values, the cells are wet and the mesh is further refined (Robl, 2021). However, the topographic data should always have the finest resolution. In order to prevent topography from interpolation to coarser cells, the data must be initialised and assigned to a separate variable ( $Zb$ ) (Popinet, 2012, Robl, 2021).

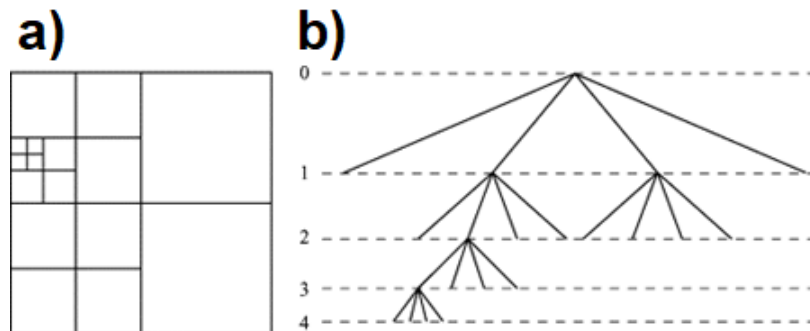


Figure 19: Subdivision of a) a quadtree and the corresponding b) tree representation for four levels of refinement (Popinet, 2003).

### Setting inflow conditions

A valid flood simulation file requires the specification of the inflow conditions (*GfsSourceFlux*). Like a spring, the point ( $x, y$ ) of water source was specified. The inflow point was set a few meters below the Römer Brücke (Figure 20). Afterwards, implementing various discharge time series files was possible (Popinet, 2012, Robl, 2021).

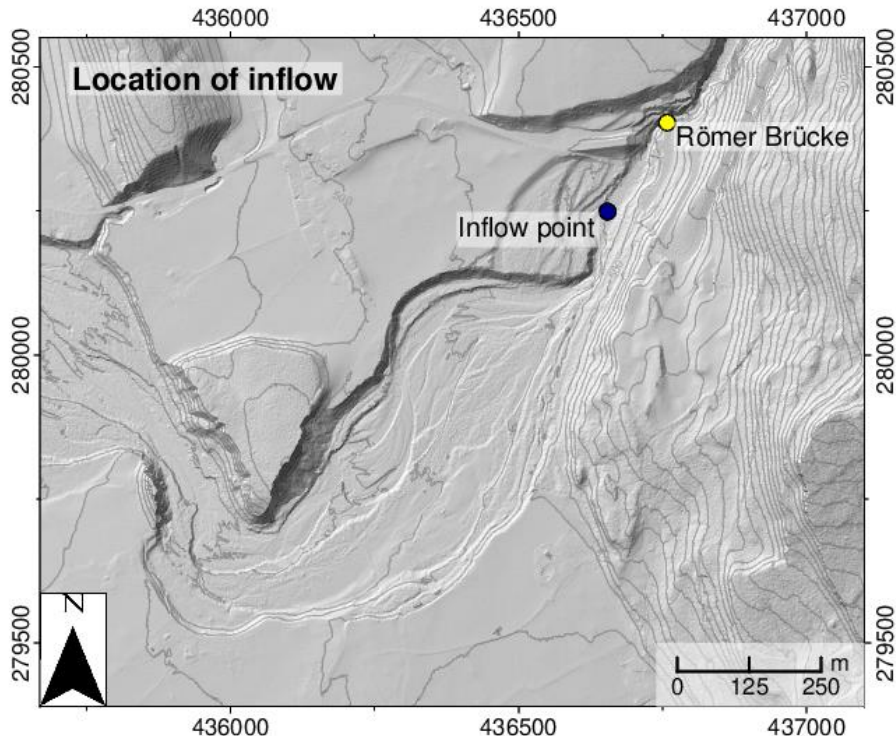


Figure 20: Location of inflow. The position of the Römer Brücke (yellow circle) and of the inflow point (blue circle at 436654 E 280248 N, MGI GK M31) are marked within the simulation domain.

### Adding friction

In order to adapt the simulation to real-world conditions, friction must be implemented. As already explained in chapter 2.1, different friction models based on various roughness coefficients exist (Grenfell, 2015). Here, the Smart, Duncan and Walsh (2002) (SDW) friction model was implemented in order to reproduce the flow pattern consistently. It is based on spatial and temporal variations in the flow velocity, the water depth and in the hydraulic roughness parameter  $Z_0$  (Popinet, 2012). The friction factor  $r$  depends on the ratio between the hydraulic roughness and flow depth (Noss and Lorke, 2016). In total, the flow resistance increases with flow velocity but decreases with flow depth. The hydraulic roughness ( $Z_0$ ) can be either constant or variable (Popinet, 2012, Robl, 2021). However, a variable roughness parameter representing the grain size distribution would adapt the flow resistance better to the real world conditions (Smart et al., 2002, Robl, 2021). Therefore, a roughness map that approximates the channel bed roughness, was derived from a combined DEM. The majority of the DEM is based on the DEM 2013 provided by the state government of Salzburg with a spatial resolution of 1m, which also serves as the topographic foundation for the simulation. The second part was generated in 2018 in the context of the UAV based monitoring period. It only covers an area of a few meters after the transition to the alluvial cone, but achieves a resolution of 0.05 m. A combination of those DEMs was necessary because the entire AOI could not be surveyed within the scope of this Master's thesis in order to generate high spatial resolution data due to time constraints. By implementing the DEM with a higher resolution into the other, the accuracy of the elevation model was partially increased. By using a moving window, the highest and lowest values were identified and the derived outputs were saved as new grids. Subsequently, the difference between the minimum and the maximum elevation was calculated in order to generate a roughness grid (Busse et al., 2017). The output was a roughness map that has been assigned

to the roughness parameter  $Z0$  in order to implement the variable hydraulic roughness (Popinet, 2012, Robl, 2021).

#### 4.2.2.3 Implementing physical parameters, thresholds and virtual data loggers

Water depth and flow velocity are default variables of the *GfsRiver* module, but bed shear stress and shear velocity must be computed separately. The basal shear stress is strongly dependent on the flow resistance and the flow velocity (Larsen and Lamb, 2016, Scherler et al., 2017). In the previously defined flood simulation file, the flow resistance is based on the SDW friction model (Smart et al., 2002, Popinet, 2012). Consequently, the dimensionless friction coefficient  $r$  is used for the calculation of the bed shear stress  $\tau_b$  (17) (Smart et al., 2002). It is expressed as a quadratic function of the ratio between the flow velocity [m/s] and the flow resistance, multiplied by the constant water density  $\rho$  (1000 kg/m<sup>3</sup>) (Scherler et al., 2017).

$$\tau_b = \left(\frac{V}{r}\right)^2 * \rho \quad (17)$$

Once, the calculation of the bed shear stress was implemented, the shear velocity could be derived from it (Smart et al., 2002). Based on equation (4), it is the result of the root of the basal shear stress divided by the density of water. After the water depth, flow and shear velocity as well as the bed shear stress have been successfully included, the previously calculated thresholds for initial sediment motion and plucking of limestone bedrock were also implemented.

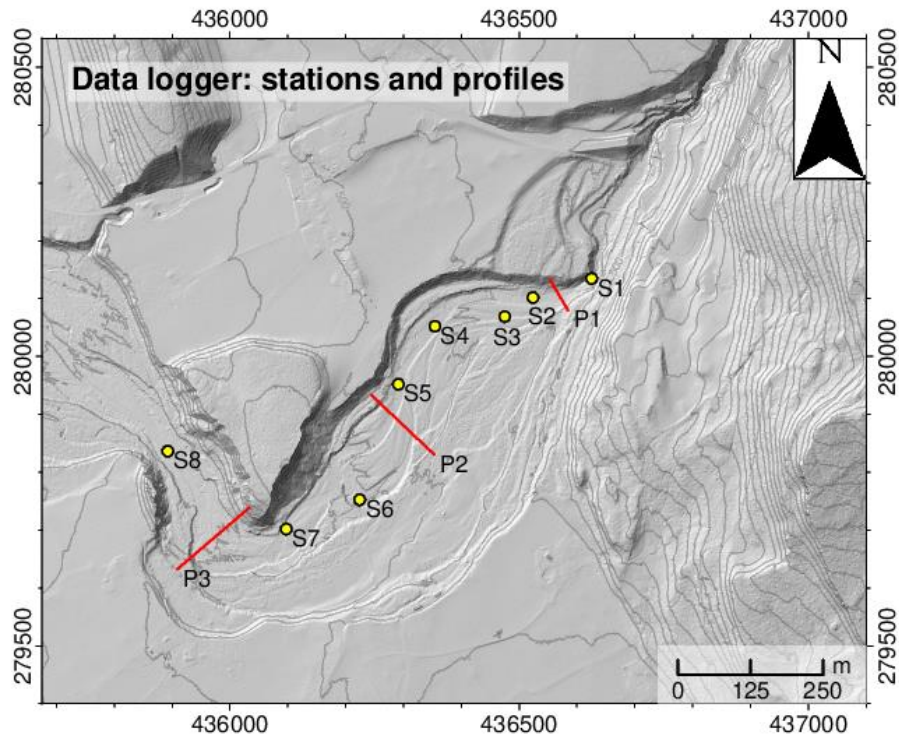


Figure 21: Virtual data loggers. The position of the punctual data loggers (yellow circles) and profiles (red lines) is shown. Data logger and profiles are annotated by S1 – S8 and P1 to P3, respectively.

It is advantageous to know the exact values of various physical parameters at important locations when it comes to the analysis of susceptible sites for initial sediment motion and plucking. For this purpose, virtual data loggers were set as point and vector data using the GRASS GIS software (Figure 21). They were positioned widely distributed in the simulation domain for monitoring the progressively extending flooding during the flood simulations. Subsequently, the virtual data loggers were included in the flood simulation parameter file in order to generate output at each of them.

## 5 Results

The main results are 1) monitoring alterations within the riverine landscape, 2) the determination of thresholds for incipient sediment motion within the gravel- bed, 3) the calculation of a critical shear stress range for plucking of limestone beds, and 4) modelling single flood events with different magnitudes.

### 5.1 Monitoring

The fact that the Taugl dynamically shapes the landscape becomes clear when comparing the orthomosaics from 2018 and 2019, as they show two entirely different situations. A wide, single thread river is recognisable in the orthophoto of 2018 (Figure 22a). The tipping limestone beds at the orographic right side are buried by alluvium only a few meters downstream of station 2. Here, detached blocks are deposited. On the left channel side bedrock is only uncovered in the first meters of the orthomosaic. Along profile 1 as well as on the same level of station 3 but on the right channel side, the limestone beds are punctually exposed at the channel bed. Station 2 is positioned on laterally protruding bedrock, which is covered by a sediment layer. Driftwood is deposited widely distributed on the gravelled surface and vegetation, which partly borders the right channel side, has established. Furthermore, low stage vegetation cover has established on the gently tipping bedrock in the vicinity of station 2. At the downstream limit of the orthomosaic section, the channel branches out.

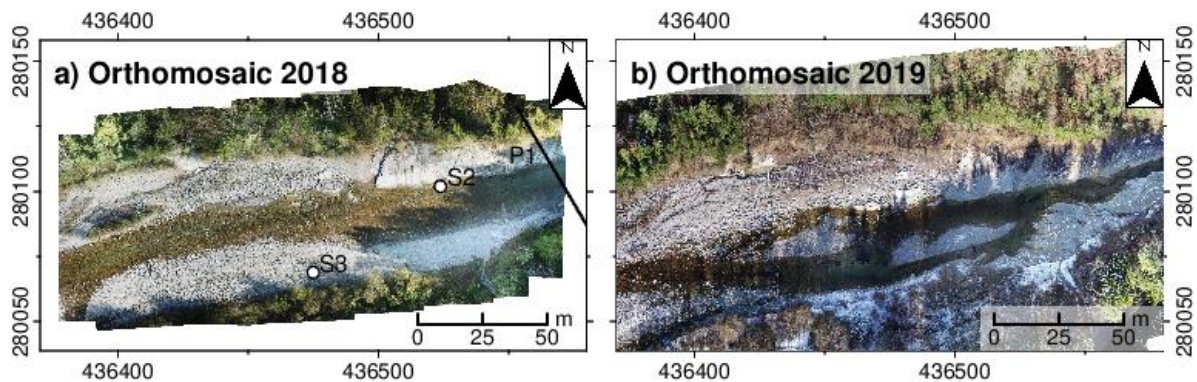
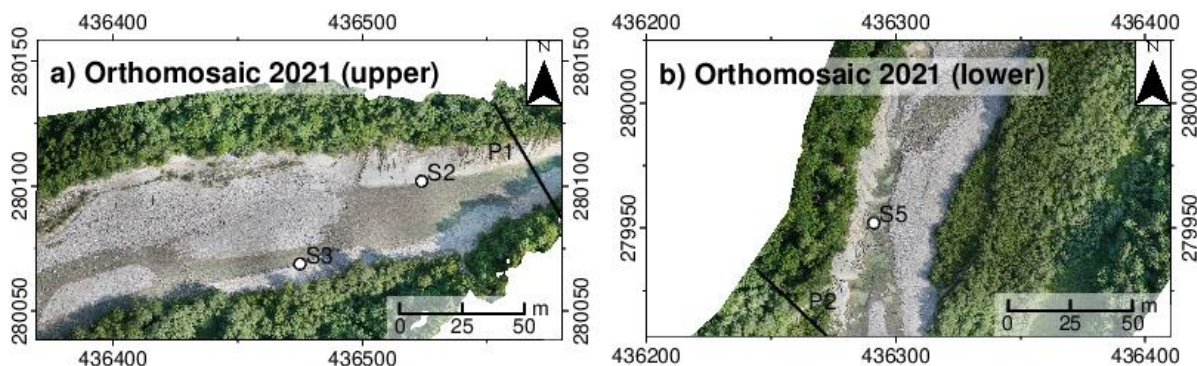


Figure 22: Sections of the orthomosaics derived by drone surveys from a) 23.04.2018 and b) 04.12.2019. The position of the virtual data loggers S1 and S2 (white circles) as well as the profile P1 (black line) is shown in a).

In contrast, the channel in 2019 is rather narrow and branches out rapidly. Bedrock is visible on both sides. The bedded limestone on the left channel side is buried by alluvium after about 50 m within the section of the orthomosaic shown in Figure 22b. At the right, the position where the bedrock is buried by alluvium has not changed compared to 2018. Again, sediments deposited on the protruding bedded limestone can be observed in the vicinity of station 2. The established vegetation in this site remains, too. The channel is buried by alluvium between the bedrock boundaries except in a small channel section downstream of profile 1 where the bedrock is un- or only slightly covered. As soon as the gently tipping limestone beds are buried by alluvium, the river branches out and the stream is separated by two sequential unvegetated gravel banks. Except towards the downstream limit of the orthophoto no major vegetation cover has established. In contrast, driftwood was deposited widely distributed within the

floodplain. Since the survey was conducted in winter, bedrock and alluvium are partially covered by snow. In the vicinity to the adjacent forest, several broken branches are deposited scattered on the bedded limestone (e.g. above station 2). Furthermore, both orthomosaics of 2018 and 2019 show a large shadow cast by the forest on the orographic left. This causes darkening larger areas.

The survey of 2021 showed that the fluvial landscape has changed again (Figure 23a). The gently tipping bedrock on the orographic left is buried by alluvium at approx. the level of station 2. Compared to the situation in 2018 and 2019, the extent of the uncovered limestone beds on the right channel remains unchanged. After the bedrock is buried by alluvium, the channel initially widens considerably, but narrows abruptly in the vicinity of station 3. Subsequently, the channel branches out. While it is still laterally bordered by gently tipping limestone beds, the channel bed is already covered with sediments. Shortly before the limestone beds are buried by alluvium at the left channel side, the uncovered area increases for some meters. Nevertheless, the proportion of uncovered bedrock on the left channel side is lower compared to 2019. Deposited driftwood is distributed on the alluvium as well as on the bedded limestone. On the orographic right of the floodplain, extensive lateral vegetation has established roughly in parallel to the adjacent forest. Vegetation on the gently tipping bedrock, which was monitored already in 2018, has persisted until 2021. Moreover, the forest on the orographic left side casts shadows.



*Figure 23: Sections of the orthomosaic derived via drone survey from 23.07.2021. In a) the position of the virtual data loggers S2 and S3 (white circle) as well as the profile P1 (black line) is shown. The section in b) is situated further downstream and thus the position of the data logger S5 (white circle) and the profile P2 (black line) is marked.*

Since the survey in 2021 covers a comparatively larger area, uncovered bedrock over approx. 100 m at the right channel side can be identified (Figure 23b). The stream is on direct contact with the limestone beds. Additionally, bedrock is partly uncovered within the channel bed in the vicinity of station 5. The channel is separated by gravel banks up- and downstream of the bedrock site. No vegetation has established on the alluvium, but partly extends far out onto the bedrock. The floodplain on the left is relatively wide and borders an overgrown area. This site is separated from the adjacent woodland by a narrow strip without vegetation.

Elevation changes indicate the varying cover of bedrock by alluvium. By using SfM photogrammetry, DEMs were derived from the data collected during the surveys (Figure 24b - 24d). While a spatial resolution of 0.05 m was achieved in 2018 and 2019, an even higher one of 0.01 m was attained in 2021. High resolution enable an analysis of elevation changes within the alluvium, vegetation and bedrock. In addition to the self-generated DEMs, a further one with a spatial resolution of 1 m was provided by the state government of Salzburg. These data were obtained in 2016 via ALS (airborne laser scanning)

survey (Figure 24a). Differences in spatial resolution are clearly reflected in the visualization. In high-resolution images, deposited drift wood is detectable based on its higher elevation values in an elongated form compared to the surrounding area (Figure 24b-d). Punctual increasing elevation values can represent both larger blocks and isolated vegetation. Unusually high values at the margin of the floodplain originate from the adjacent forest. While at a resolution of 0.05 m to 0.01 m even the single grains are identifiable, at 1 m not even deposited driftwood is clearly recognisable. Nevertheless, bedrock can be well distinguished from alluvium in 2016. This is based on the identification of the bedded bedrock structure, which is reflected by elevation changes. It can therefore be assumed that the position where the gently tipping limestone beds on the right channel side are buried by alluvium is similar to 2018.

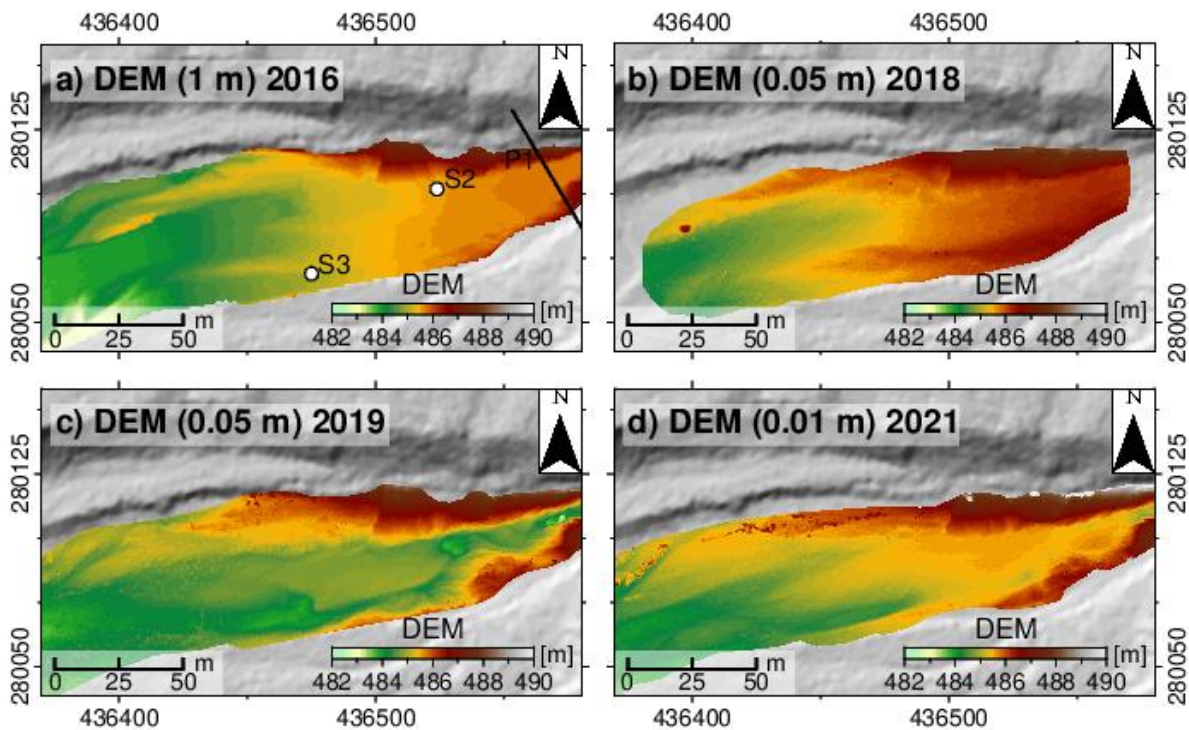


*Figure 24: Sections of the DEMs from 2016 to 2021 (irregular measuring interval) at the transition from bedrock to alluvium. The DEM (1 m) 2016 (a) was provided by the state government of Salzburg. The DEMs 23.04.2018 (b), 04.12.2019 (c) and 23.07.2021 (d) were processed with SfM photogrammetry and acquired via drone surveys. The DEMs 2018 and 2019 have a resolution of 0.05 m and 2021 0.01 m. The position of the virtual data loggers S1 and S2 (white circles) as well as the profile P1 (black line) is shown in a).*

For the years 2016 and 2021, elevation data also exist further downstream (Figure 25). In the generated DEM of 2021, the influence of vegetation is apparent. Significantly higher values than those measured within the channel (approx. 480 – 483 m), as observable e.g. on the orographic left floodplain, indicated vegetation cover. But also at the downstream limit of the uncovered bedrock site, identified on the corresponding orthophoto, high elevation values indicated vegetation.

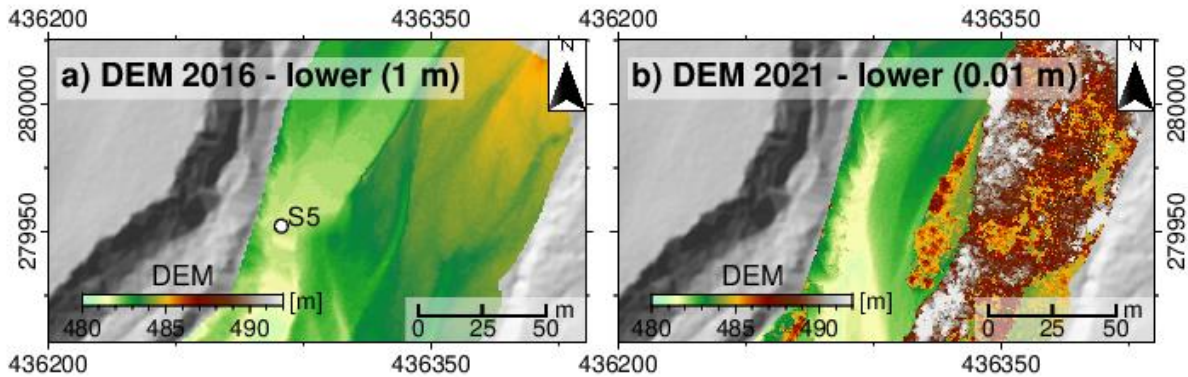


Figure 25: Sections of the DEM 2016 and 2021 in the middle of the AOI. The DEM (1 m) 2016 (a) was provided by the state government of Salzburg with a spatial resolution of 1 m and b) was derived from SfM photogrammetry method with data obtained from a drone survey on 23.07.2021. The position of the data logger S5 (white circle) is shown in a).

## 5.2 Critical shear stresses

The calculation of the critical shear stress for incipient sediment motion and plucking limestone beds are based on equation (9) and (12), respectively. The results of the parameters required for the computation and the derived thresholds are presented below (Table 3).

Table 3: Critical bed shear stresses required for initial sediment motion and plucking limestone beds . Additionally, information about the corresponding critical Shields numbers is listed.

<b>Initial sediment motion</b>	
Critical Shields number $\tau_c^*$	0.045 [ ]
Critical bed shear stress $\tau_b^*$	46.35 [Pa]
(based on $D_{50} = 0.07 \text{ m}$ )	
Critical bed shear stress $\tau_b^*$	66.21 [Pa]
(based on $D_{50} = 0.1 \text{ m}$ )	
<b>Block entrainment by sliding</b>	
Critical Shields number $\tau_{pc}^*$	0.059 – 0.083 [ ]
Critical bed shear stress $\tau_{pc}$	486 – 684 [Pa]

### Threshold for initial sediment movement

The calculation of the threshold for initial sediment motion required the determination of the median grain size  $D_{50}$ . The results of the field measurements along five 3 m long profiles, where 210 sediments were recorded, showed  $D_{50} = 0.07 \text{ m}$  (Figure 26a). The smallest grain size is 0.01 m, the largest 0.34 m. Clasts with a diameter of 0.04 m were measured most frequently (approx. 17 %). The frequency of the small sized clasts is thus comparatively high and decreases due to rising grain diameter. However, a slight increase in coarser sediments is noticeable. Nevertheless, the total proportion of finer clasts is significantly higher.

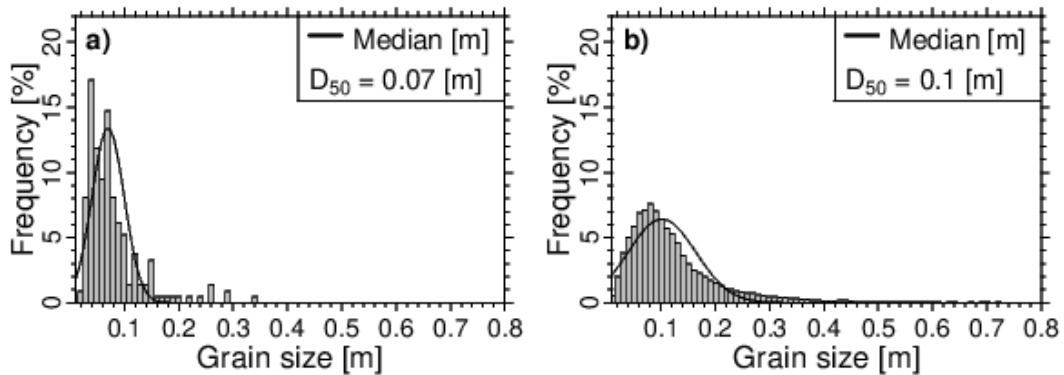


Figure 26: Comparison of the grain size [m] count based on a) field measurements and b) statistical evaluation of the calculated roughness map.

In contrast, based on the statistical evaluation of representative areas of the roughness map (Figure 27) a higher median,  $D_{50} = 0.1$  m, resulted (Figure 26b). Here, the measured grain sizes in dedicated areas (251017 z- values served as samples) range from 0.01 to 0.8 m. Again, it is noticeable that the proportion of finer particles is significantly higher. Most of the recorded clasts measure 0.08 m (approx. 7.5 %), 0.04 m greater than in the field measurements. The increase up to this maximum value is steep. Subsequently, the frequency tends to decrease with rising grain diameter. When comparing the sediment size counts, it is important to note that significant more clasts were recorded for the evaluation of the roughness map than in the field measurements.

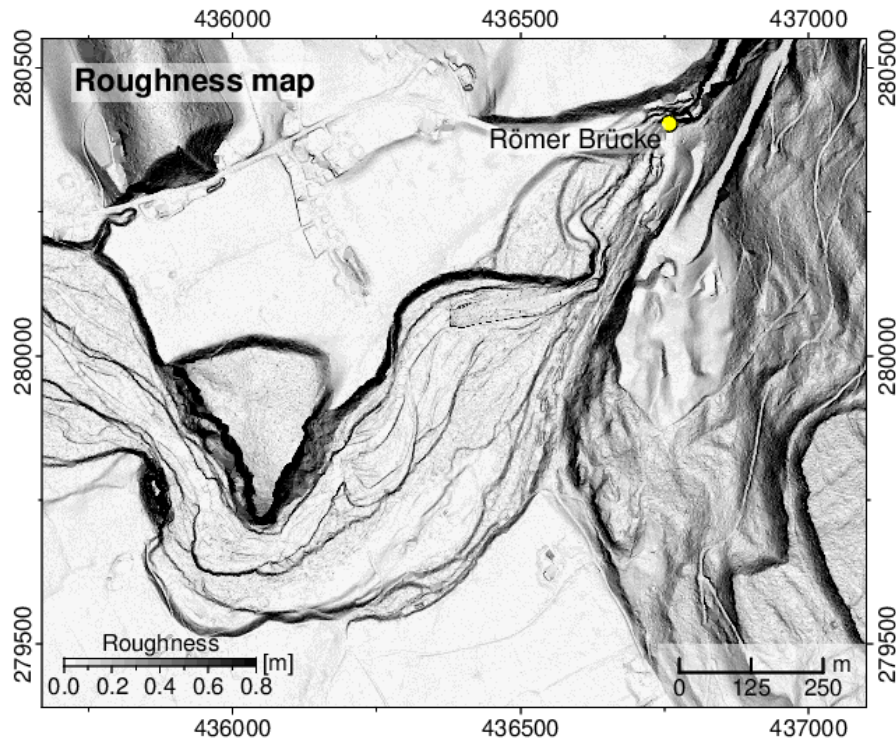


Figure 27: Roughness map showing the riverbed grain size. The position of the Römer Brücke (yellow circle) is marked.

The resulting critical shear stress for incipient sediment motion  $\tau_b^*$ , derived by using a constant critical Shields number  $\tau_c^* = 0.045$  for low gradient gravel- bed rivers and the ascertained median grain size

derived from field measurements  $D_{50} = 0.07$  m, is 46.35 Pa. Due to the higher median grain diameter based on the statistical evaluation of the roughness map,  $D_{50} = 0.1$ , a slightly higher threshold value of 66.21 Pa resulted (Table 3). Concurrently with the rising median grain diameter, the critical value for initial movement increased by 20 Pa, while all other parameters were kept constant. To investigate the dependency between median grain size and the threshold value more precisely, both variables were plotted against each other (Figure 28). Thereby, a linear relationship is revealed. It is apparent, that an increase in median diameter causes a rising basal shear stress which is required for initial sediment movement.

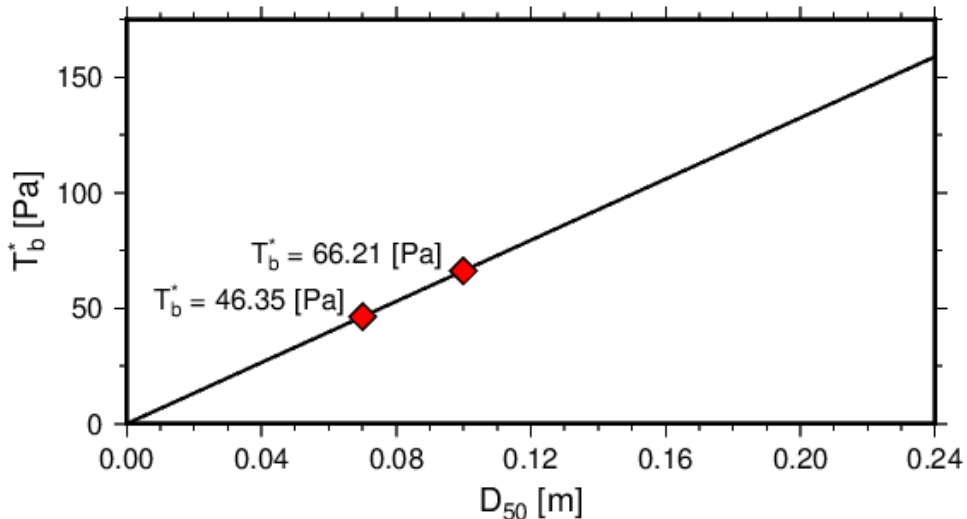


Figure 28: Linear correlation between the median grain size  $D_{50}$  and the critical shear stress for incipient sediment motion  $\tau_b^*$  [Pa]. While the median diameter  $D_{50}$  is varied, all other parameters were held constant at  $\tau_c^* = 0.045$  [ ],  $2500$  [ $\text{kg}/\text{m}^3$ ],  $\rho_s = 2500$  [ $\text{kg}/\text{m}^3$ ],  $\rho = 1000$  [ $\text{kg}/\text{m}^3$ ] and  $g = 9.81$  [ $\text{m}^2/\text{s}$ ]. The resulting thresholds for initial sediment motion based on the calculated median grain sizes 0.07 m and 0.1 m are marked in red.

### Threshold for plucking limestone beds

The ratio  $P/L$ , derived from field records (i.e. 50 blocks were measured), was set to 0.26, indicating that the block length is larger in relation to the protrusion height (Figure 29). The resulting ratio between flow and shear velocity  $u/u_*$ , based on 100 samples resulting from flood simulations, is 6. As a consequence, the flow velocity is significantly higher than the shear velocity. The critical sidewall stress range between 0 and 0.1. These values were based on field observations, since primarily widely open cracks corresponding to a sidewall stress of 0 were observed, as well as small, non-cohesive sediment accumulations and partly vegetation within the cracks with a sidewall stress of about 10 % of the block weight per unit area. By inserting the determined values into equation (11), a critical Shields number  $\tau_{pc}^* = 0.059$  was calculated under the assumption of a dimensionless sidewall stress  $\tau_w^* = 0$ . For  $\tau_w^* = 0.1$  with the remaining parameter values kept constant, the resulting  $\tau_{pc}^* = 0.083$ . Besides the critical Shields number, the averaged block diameter is necessary to calculate the critical shear stress for block entrainment by sliding. Based on 50 measured blocks in the field, the determined averaged block diameter  $D = 0.56$  m. Thereby a lower and an upper critical shear stress for plucking  $\tau_{pc}$  jointed limestone was calculated, which is 486 Pa and 684 Pa, respectively (12) (Table 3).

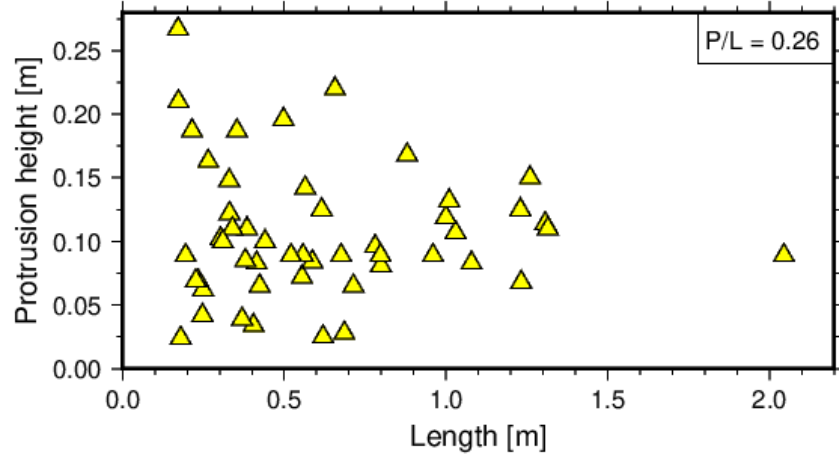


Figure 29: Ratio between protrusion height  $P$  [m] and block length  $L$  [m]. Based on the measurement of 50 blocks (yellow triangles), the resulting ratio was set to 0.26.

Varying the ratio between block protrusion height and length shows that the critical Shields number decreases significantly with increasing relative protrusion (Figure 30a). At  $P/L > 0.5$  m, the decreasing trend is still constant but flatter. In contrast, with increasing sidewall stress of the block, the critical Shields number rises as well (Figure 30b). However, the increase is flatter at lower sidewall stresses but significantly rises when approximating  $\tau_w^* \sim 1$ .

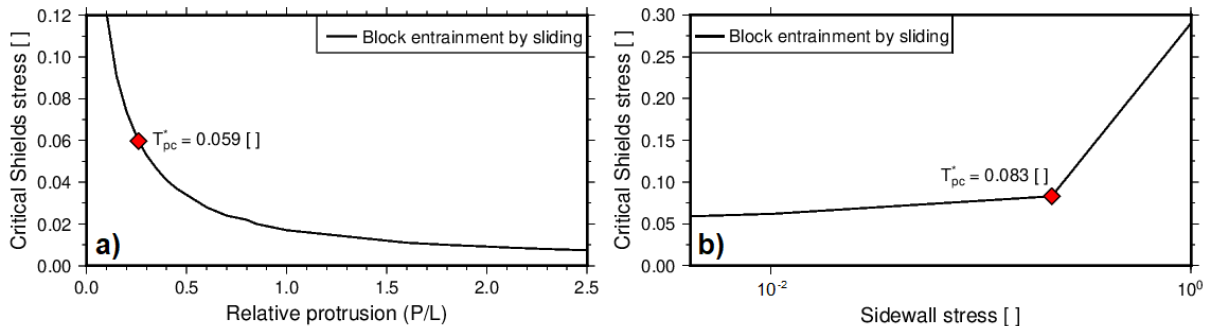
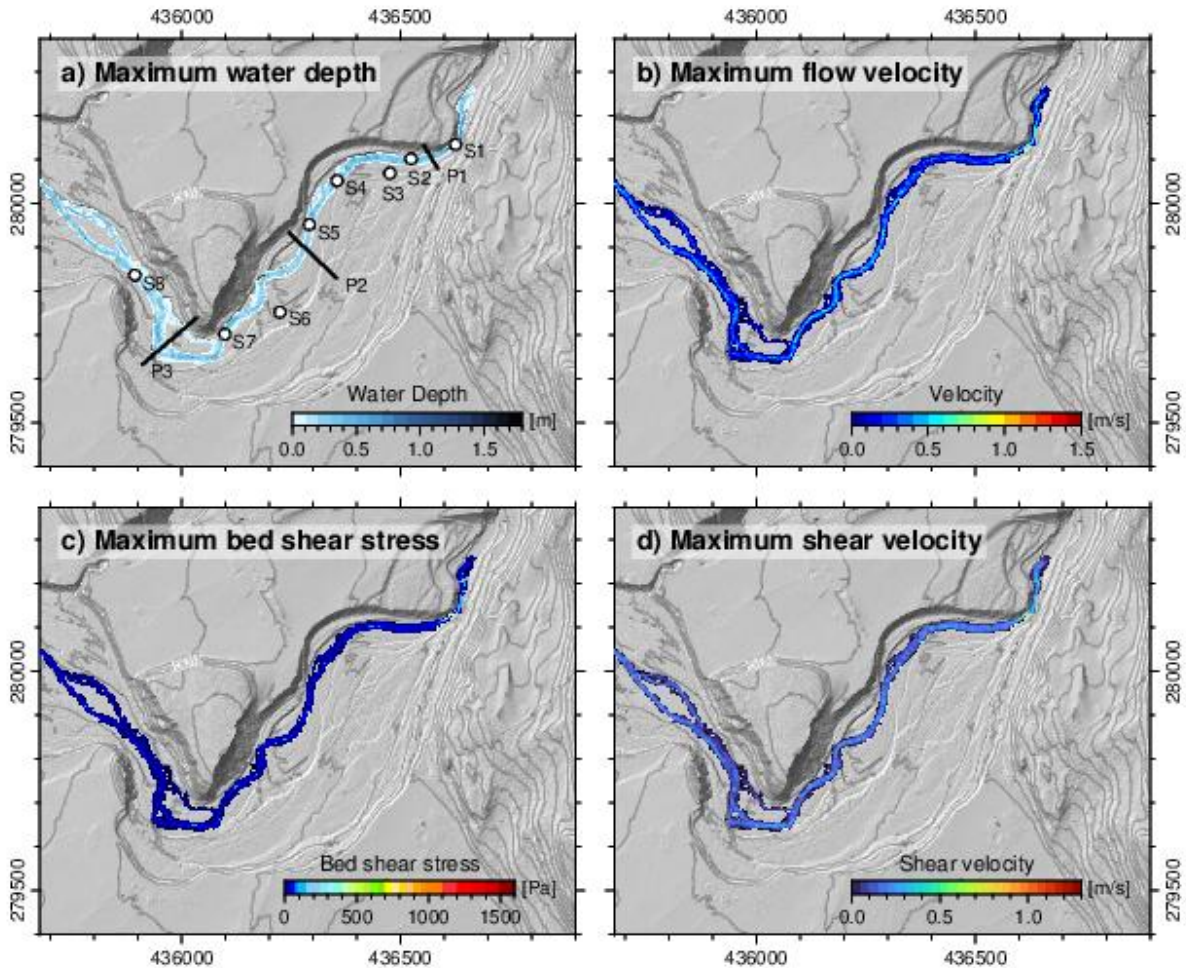


Figure 30: Varying critical Shields stress [ ] for block entrainment by sliding. a) Variable relative protrusion (ratio between block protrusion height and length) and b) dimensionless sidewall stress versus dimensionless critical Shields number  $\tau_{pc}^*$  [ ]. All other values were held constant at  $u/u_* = 6$ ,  $\tau_w^* = 0$ ,  $F_L^* = 0.85$ ,  $C_D = 1$ ,  $\theta = 4^\circ$ ,  $\phi = 30^\circ$ ,  $P/L = 0.26$  and  $\tau_w^* = 0$  based on equation 11. The resulting critical Shields numbers  $\tau_{pc}^* = 0.059$  and  $\tau_{pc}^* = 0.083$  are marked in red.

### 5.3 Simulating floods of different magnitudes

Based on the evaluation of the discharge data of the hydrographic service of Salzburg from January 1976 to June 2006, the average daily discharge is about 1 m<sup>3</sup>/s. Simulating this discharge rate constant until a steady state is reached results in a maximum water depth of ~1.7 m, flow velocity of ~1.4 m/s, shear velocity of ~1.2 m/s, and bed shear stress of ~1530 Pa in the whole simulation domain (Figure 31). All maximum values are located in the vicinity of station 1, where the channel forms a narrow slot canyon. Downstream of the first profile, at the transition from the gorge to the low gradient alluvial cone, all parameter values are comparatively low. Moreover, station 3 is positioned in the remaining dry area of the floodplain. Further downstream, between the stations 4 and 7, the parameter values rise again. However, the values are clearly lower than their maxima. The channel section crossing the second

profile is rather narrow and single-threaded. In addition to station 3, the station 6 and its vicinity is also not inundated. Across profile 3, three channels are recorded. Here, two streams are separated from their main channel by gravel banks of different sizes. Downstream of station 8, the river splits and merges again.



*Figure 31: Peak flow of 1 m<sup>3</sup>/s modelled with the Gerris flow solver. The images a), b), c) and d) are showing the maximum values of water depth [m], flow velocity [m/s], bed shear stress [Pa] and shear velocity [m/s] that are reached during a constant inflow until a steady state has established. The position of all stations (white circles) and profiles (black lines) are shown in a).*

In order to identify the discharge rate that is necessary to inundate the stations 3 and 6, rising magnitudes were simulated. Figure 32 displays the increasing water depth at both stations caused by discharge rates of different magnitude. Station 3 is flooded from a discharge of about 13 m<sup>3</sup>/s onwards. The water depth initially rises steeply, but from about 30 m<sup>3</sup>/s the increase in flow depth becomes shallower. Station 6 is inundated by exceeding a discharge of approx. 25 m<sup>3</sup>/s. The increase in water depth is similar to that at station 3, although the measured water levels are always lower here. According to the hydrographic service Salzburg, a peak flow of 25 m<sup>3</sup>/s corresponds to an annual recurrence interval.

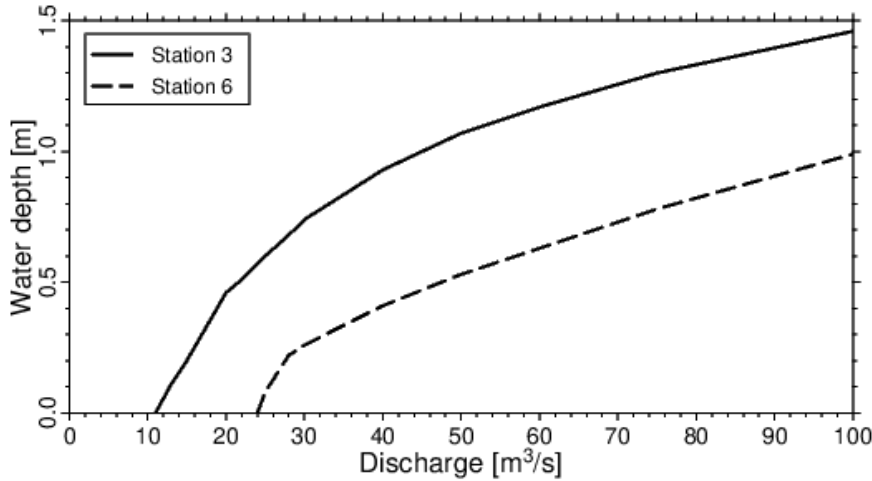


Figure 32: Water depth at the stations 3 (solid line) and 6 (scattered line) during increasing discharge rates.

The varying water depths resulting from floods with increasing magnitudes are also recorded across the three profiles (Figure 33). During a peak flow of  $25 \text{ m}^3/\text{s}$ , high values are already measured in the channel at profile 1 with a maximum of about 1.20 m. The rise of the discharge rate to  $50 \text{ m}^3/\text{s}$  results in a strong increase of the water depth to about 1.56 m, and at a magnitude of  $75 \text{ m}^3/\text{s}$  the maximum water depth is 1.82 m. In addition to the increase in water depth, the water also spreads out laterally. As a result, larger parts of the floodplain are inundated during rising discharge rates. Interestingly, only one meter on the orographic left side of profile 1 is affected by this expansion. This can be observed during the increase in magnitude from  $25$  to  $50 \text{ m}^3/\text{s}$ . In contrast, a discharge of  $25 \text{ m}^3/\text{s}$  is not yet sufficient to flood the entire floodplain across the second profile. It is apparent that the floodplain between the two channels on the orographic right is already inundated at a discharge of  $25 \text{ m}^3/\text{s}$ . However flooding the entire floodplain without remaining dry spots requires a discharge rate of  $75 \text{ m}^3/\text{s}$ . At a peak flow of  $75 \text{ m}^3/\text{s}$ , the maximum water depth is 1.60 m. The floodplain along profile 3 is almost completely inundated at a discharge rate of  $25 \text{ m}^3/\text{s}$ . However, increasing the discharge rate to  $30 \text{ m}^3/\text{s}$  results in a complete flooding. Consequently, the further rise in magnitude to  $50 \text{ m}^3/\text{s}$  and  $75 \text{ m}^3/\text{s}$  primarily caused a change in the water depth. The maximum water depth at a discharge of  $75 \text{ m}^3/\text{s}$  is 1.50 m.

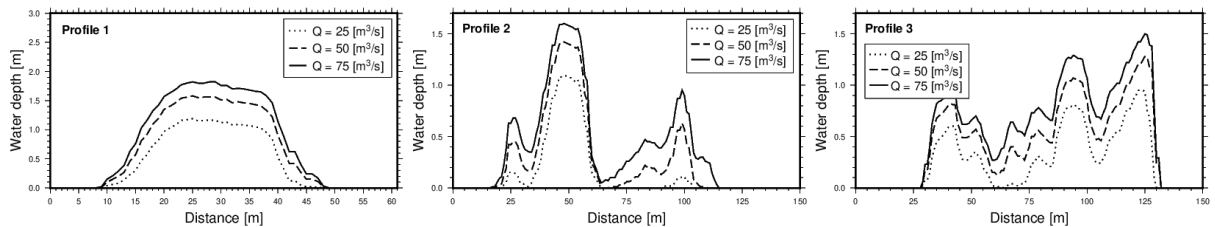


Figure 33: Water depth [m] across the three profiles during peak flows of increasing magnitude ( $Q = 25, 50, 75 \text{ m}^3/\text{s}$ ).

Moreover, the maximum water depth is visualized as 2D- raster datasets for different discharge rates (Figure 34). From a magnitude of  $25 \text{ m}^3/\text{s}$  onwards, the stations 3 and 6 are flooded, but dry areas are visible in the immediate vicinity to the west of station 3. Further non inundated areas are detectable downstream of station 5 on both sides of the channel, which also affects the second profile and the area north of the sixth station. In the area of the third profile, dry spots are discernible in the middle of the flood plain. The same can be observed further downstream.

Compared to a discharge rate of 1 m<sup>3</sup>/s, it is noticeable that the gravel bank between the divided river arms downstream of station 8 is now also flooded. The water depth is here considerably shallower than in the main channels. This phenomenon can be observed throughout the entire simulation domain, making it easy to distinguish between the main channels and the inundated floodplain. Due to the increase of the discharge rate to 50 m<sup>3</sup>/s, the flooded channel sections have spread further. This also includes the area between station 4 and 5. Nevertheless, there are still some dry spots distributed throughout the simulation domain e.g. large parts in the vicinity to station 6. However, this area is largely submerged at 75 m<sup>3</sup>/s. In this scenario, the active width has also widened considerably between station 3 and profile 2. There are hardly any areas on the flood plain that remain dry, only between stations 4 and 5. However, even after the increase to 100 m<sup>3</sup>/s, which corresponds to a recurrence interval of hundred years according to the hydrographic Service of Salzburg, the floodplain is not completely inundated in that area. It is apparent, that primarily changes in the water depth take place since the water has not significantly spread further into the floodplain.

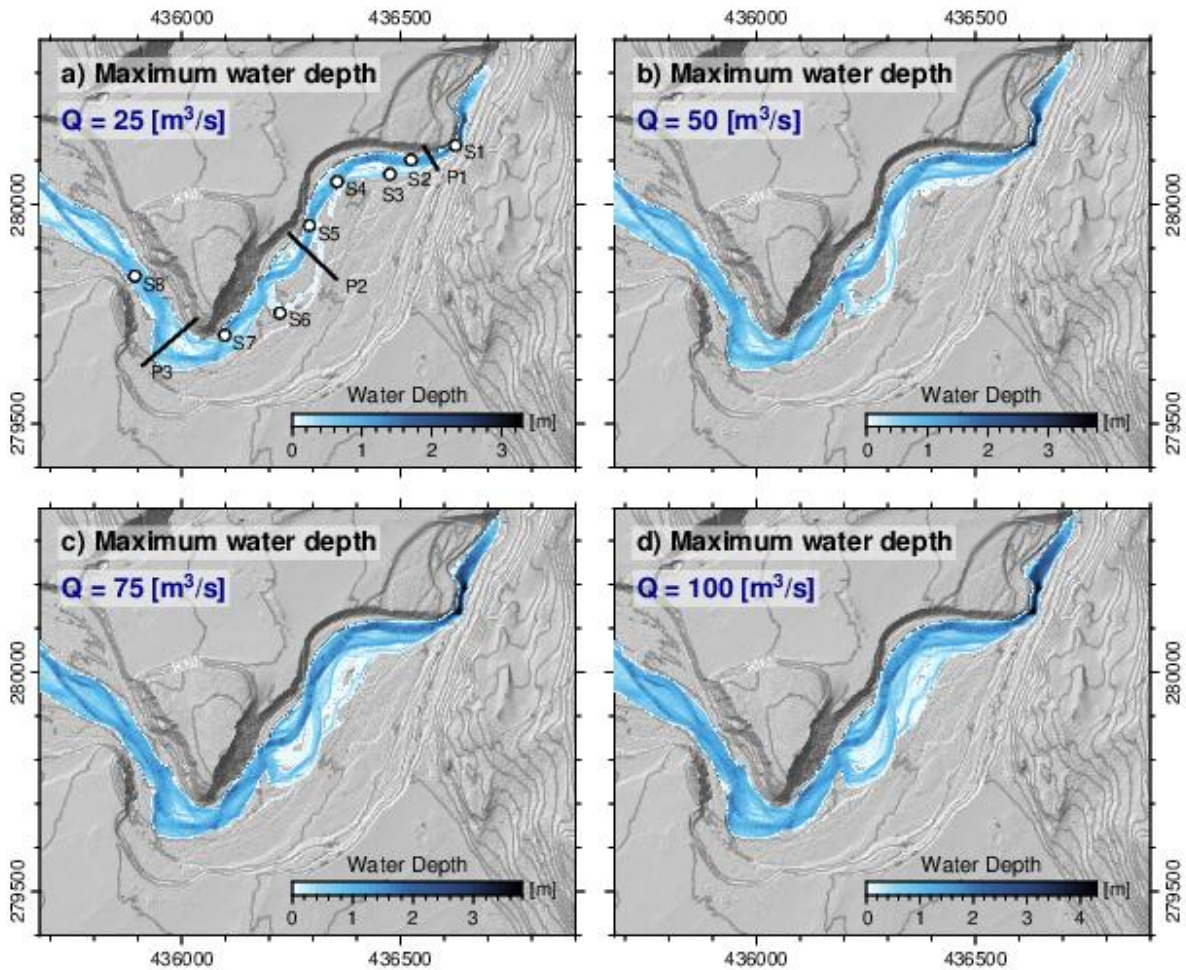


Figure 34: Evolution of maximum water depth [m] during rising discharge rates ( $Q = 25, 50, 75$  and  $100 \text{ m}^3/\text{s}$ ). The position of all stations (white circles) and profiles (black lines) are shown in a).

In addition to the water depths, Figure 35 displays maximum flow velocities of the corresponding discharge rates. Again, the highest values within the simulation domain are reached in the adjacency of station 1. In a downstream direction, the flow velocities initially decrease. Nevertheless, spatial limited rising values are recorded between the stations 5 and 7, but downstream the velocities decrease again until the downstream limit of the domain is reached. In general, higher flow velocities are measured in the main channels compared to the values on the inundated floodplain. This is particularly evident when comparing the spatial varying values in the adjacency to the stations 3 and 6. Furthermore, it is apparent that the flow velocities decrease towards the channel margins. This phenomenon is clearly visible along the profiles.

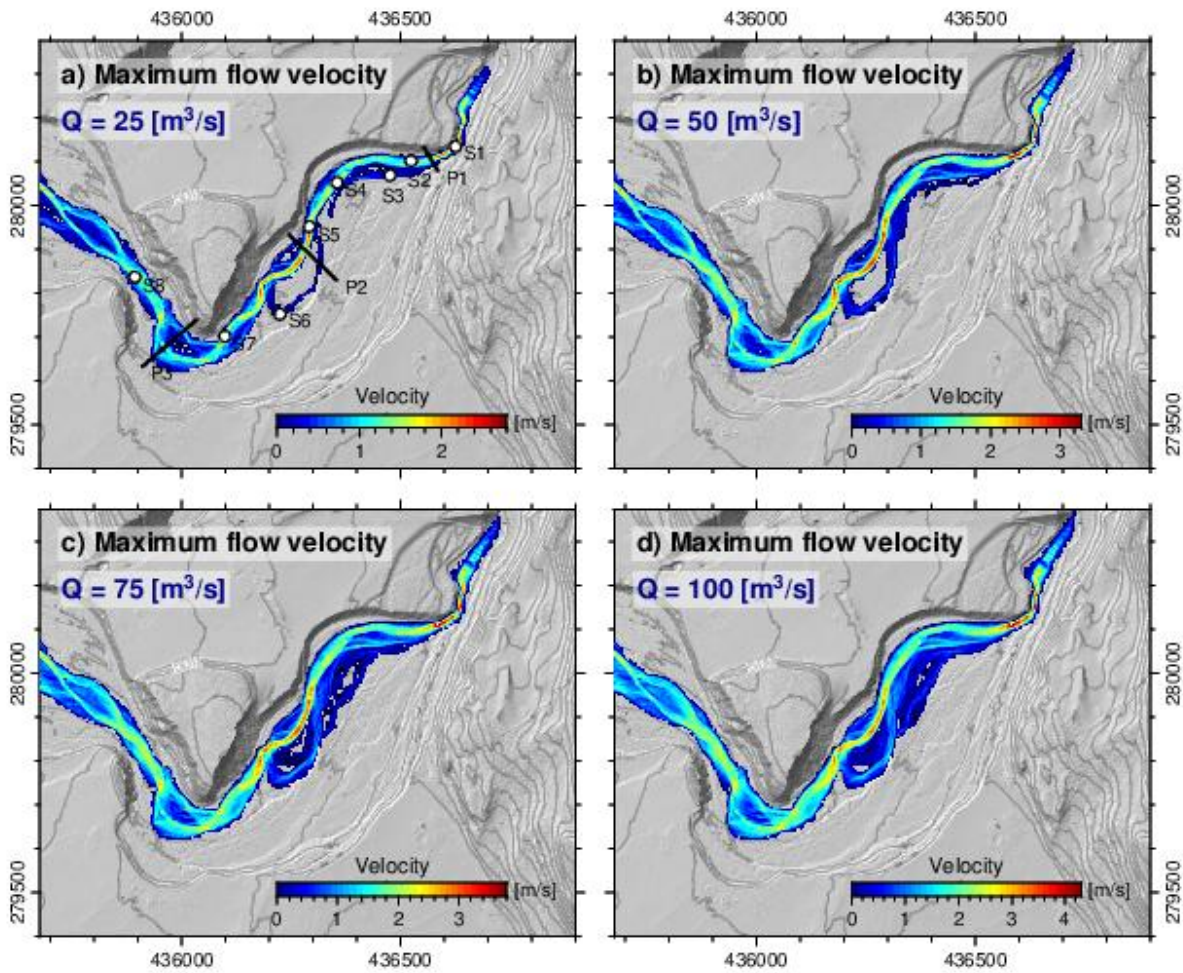


Figure 35: Alteration in maximum flow velocity [m/s] during increasing peak flows rates ( $Q = 25, 50, 75$  and  $100 \text{ m}^3/\text{s}$ ). The position of all stations (white circles) and profiles (black lines) are shown in a).

Beside water depth and flow velocity, the maximum bed shear stress is shown for four different discharges ( $Q = 25, 50, 75$  and  $100 \text{ m}^3/\text{s}$ ) (Figure 36). Like the maximum values of the other physical parameters, the highest values are measured in the vicinity of station 1. The exerted bed shear stress decrease towards station 5. Downstream, the values rise marginally within a short channel section but the shear stress here does not approximate its maximum. A stronger increase is not recorded. Similar to the flow velocities, the exerted basal shear stress is comparatively higher in the main channels than on

the inundated floodplain (e.g. in the vicinity of station 3). In addition, the maximum bed shear stress decrease towards the channel margins.

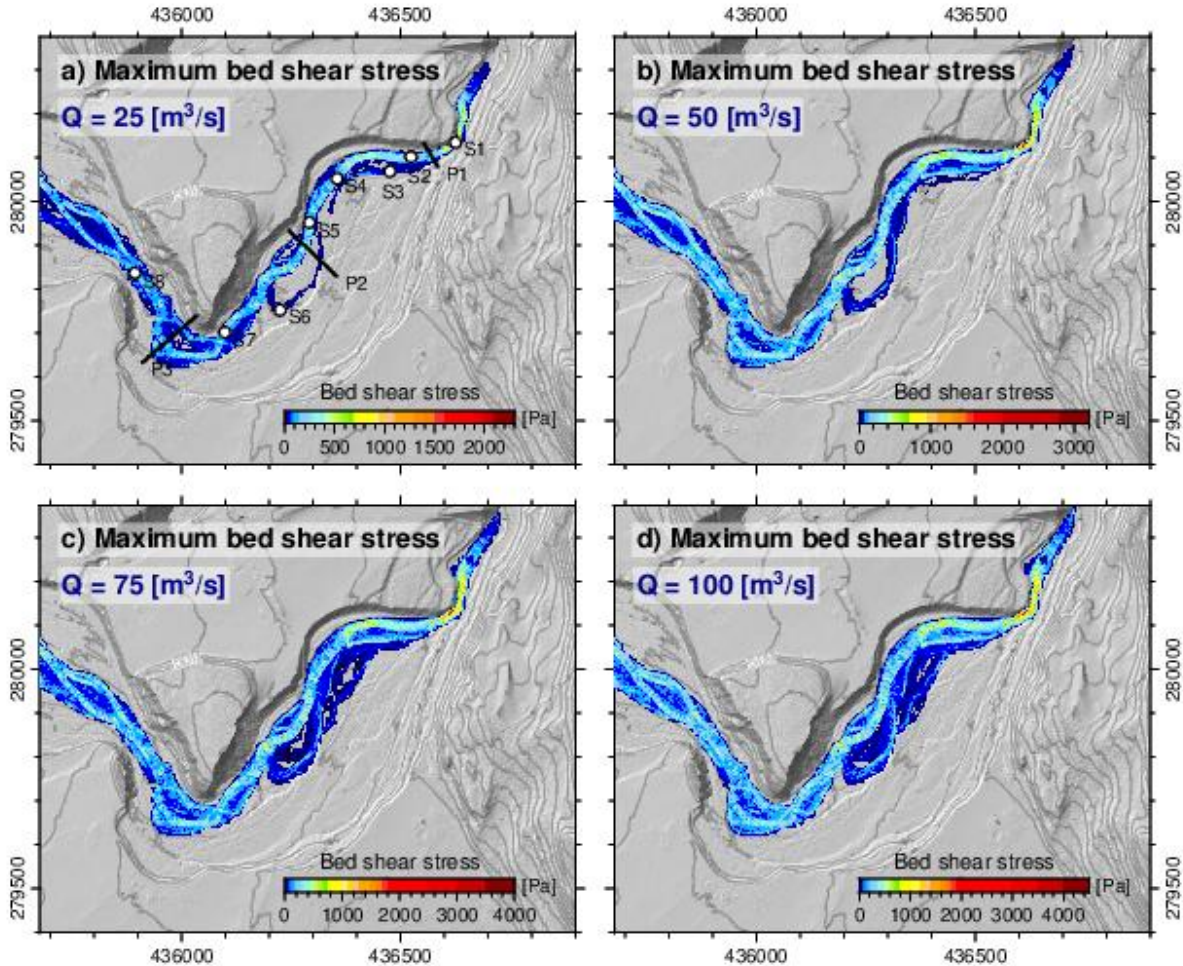


Figure 36: Exerted maximum bed shear stress [Pa] during rising discharge rates ( $Q = 25, 50, 75$  and  $100 \text{ m}^3/\text{s}$ ). The position of all stations (white circles) and profiles (black lines) are shown in a).

Plotting the maximum values of the four physical parameters (water depth, flow- and shear velocity as well as bed shear stress) within the whole simulation domain against rising discharge rates reveals different correlations (Figure 37). The water depth initially increases strongly until about  $25 \text{ m}^3/\text{s}$ . Afterwards, a slower but steady upward trend can be observed. Followed by a comparatively stronger increase at first, the flow velocities are also rising continuously. Analysing the upward trend of the maximum bed shear stress in parallel to increasing flood magnitudes shows approximately a linear correlation. The same is observed with shear velocity. Hence shear velocity is derived from basal shear stress, it was to be expected that both trends are quite alike (Smart et al., 2002).

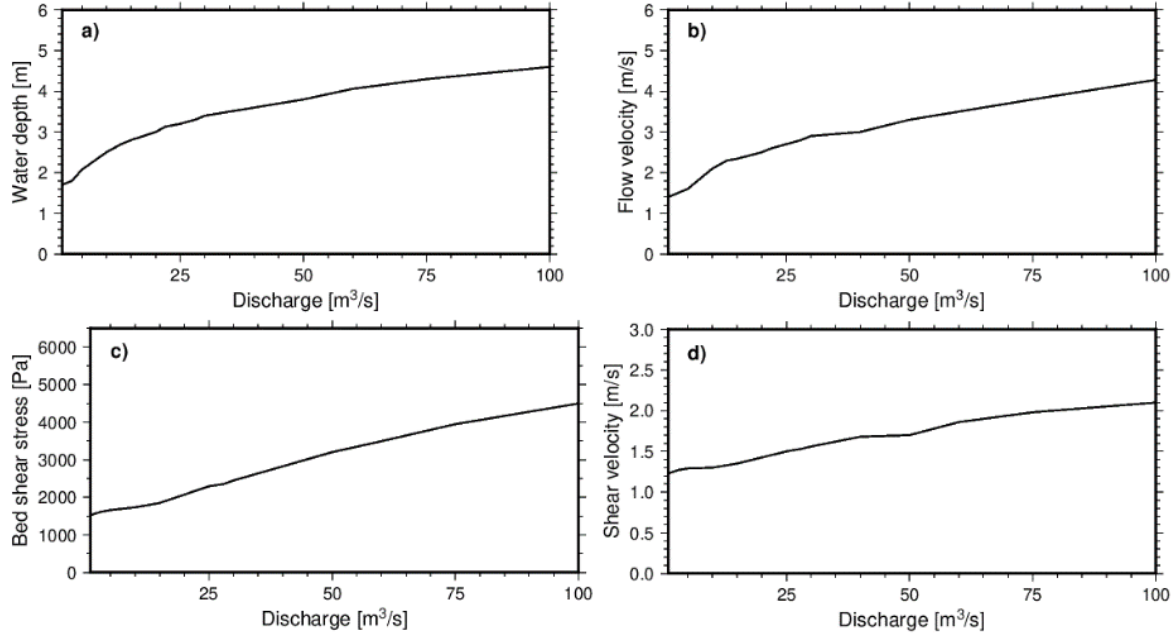


Figure 37: Relationship between variable discharge rates and the maximum values of the main physical parameters a) water depth [m], b) flow velocity [m/s], c) bed shear stress [Pa] and d) shear velocity [m/s].

## 5.4 Initial sediment motion

In order to cause incipient sediment motion, the bed shear stress exerted by the flux must exceed the critical threshold value (Whipple et al., 2013, Larsen and Lamb, 2016). Thus, both parameters were set in relation to each other. To analyse the effects of the variation in median diameter, the basal shear stress was divided by both  $\tau_b^* = 46.35 \text{ Pa}$  and  $\tau_b^* = 66.21 \text{ Pa}$ . Figure 38 reveals thereby where initial movement is triggered within the channel during different discharge rates. In order to generate the necessary basal shear stress, floods of a certain magnitude are required. For this reason, the ratio between bed and critical shear stress is visualized during discharge rates of  $1 \text{ m}^3/\text{s}$  and at  $3 \text{ m}^3/\text{s}$ . Assuming a magnitude of just  $1 \text{ m}^3/\text{s}$  and  $\tau_b^* = 46.35 \text{ Pa}$ , the bed shear stress surpasses the threshold before the transition into the gravel cone as well as in smaller areas on the alluvial surface. Although geomorphological activity is widely distributed, there are still large areas where initial motion does not occur. Presuming  $\tau_b^* = 66.21 \text{ Pa}$ , the critical threshold is only surpassed over a larger contiguous channel section before entering the alluvial surface. Further downstream, incipient sediment motion occurs only in a few isolated cases. Overall, the Taugl River conducts only marginal or highly distributed geomorphologic work within the alluvial plain during a discharge of  $1 \text{ m}^3/\text{s}$ . Rising the magnitude to  $3 \text{ m}^3/\text{s}$  causes a coincident increase in the exerted bed shear stress. As a consequence, the critical value is surpassed in the majority of the AOI. Compared to the results at a discharge rate of  $1 \text{ m}^3/\text{s}$ , sediment movement now also occurs widely distributed within the alluvial plain under the assumption of  $\tau_b^* = 66.21 \text{ Pa}$ . Movement is initiated almost continuously up to station 4 under the assumption of a discharge rate of  $3 \text{ m}^3/\text{s}$ , no matter at which threshold. Assuming  $\tau_b^* = 46.35 \text{ Pa}$ , this phenomenon even extends to about the seventh station. Further downstream from the respective stations, a decrease of initial sediment movement in certain areas can be observed. During this discharge scenario it is noticeable that the basal shear stress tends to exceed the critical one in the middle of the channel. At the margins incipient sediment motion does usually not occur. This phenomenon is apparent in both ratios e.g. between stations 2 and 4.

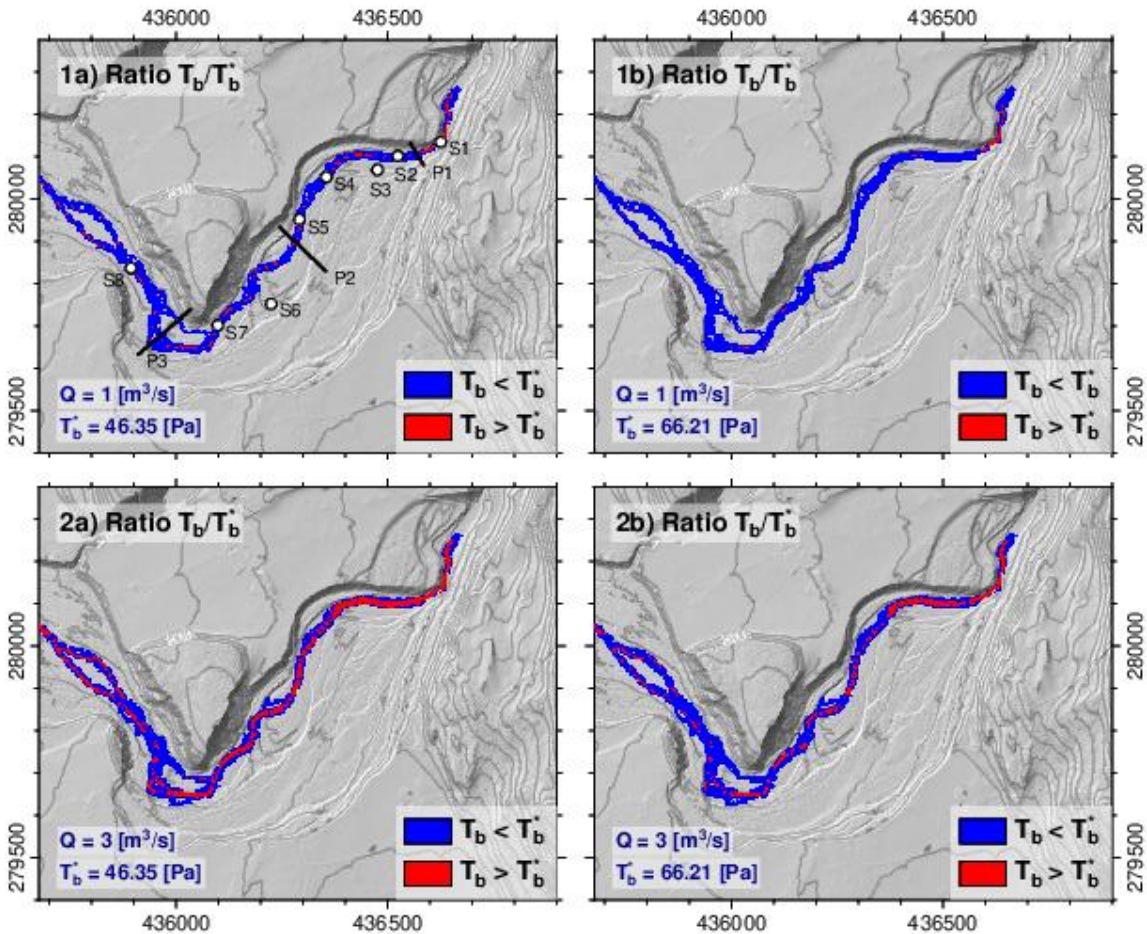


Figure 38: Ratio between the maximum applied bed shear stress and the lower and upper threshold for initial sediment motion. a) 46.35 Pa is based on the resulting median grain size from field measurements  $D_{50} = 0.07 \text{ m}$ , and b) 66.21 Pa results from  $D_{50} = 0.1 \text{ m}$ , derived from statistical evaluation of the roughness map. Both thresholds are calculated by using a dimensionless critical Shields number of 0.045. In 1) the peak flow is  $1 \text{ m}^3/\text{s}$ , in 2)  $3 \text{ m}^3/\text{s}$ . A ratio greater than 1 (depicted in red) indicates that the actual basal shear stress surpasses the threshold value ( $\tau_b^* > \tau_b$ ). In contrast, if the bed shear stress is smaller than the threshold for incipient sediment motion ( $\tau_b^* < \tau_b$ ), the ratio is smaller than 1 (depicted in blue). The position of all stations (white circles) and profiles (black lines) are shown in 1a).

The values along the profiles are decreasing towards the channel margins. Consequently, the critical values are not exceeded there. Figure 39 displays the bed shear stress along the profiles during rising discharge rates. The maximum bed shear stress achieved along profile 1 at a discharge rate of  $25 \text{ m}^3/\text{s}$  is about 622 Pa. The smaller the magnitude, the lower the applied shear stress, whereby a discharge of  $1 \text{ m}^3/\text{s}$  is not sufficient to surpass the threshold range. Consequently, the Taugl River remains inactive. However, even a slight increase in magnitude to  $3 \text{ m}^3/\text{s}$  causes incipient sediment motion, as the thresholds are mostly exceeded along the first profile (Table 4). Only at the local minimum  $\tau_b^* = 66.21 \text{ Pa}$  is not surpassed. As a result of a further increase of the discharge rate to  $25 \text{ m}^3/\text{s}$ , both thresholds are clearly surpassed. With an increasing magnitude it can also be observed how the applied bed shear stress rises laterally. While values are recorded between 16 m and 40 m at a peak flow of  $1 \text{ m}^3/\text{s}$ , they are measured between 13 m and 41 m at  $3 \text{ m}^3/\text{s}$  and from 9 m to 48 m at  $25 \text{ m}^3/\text{s}$ . However, as the laterally exerted bed shear stress is comparatively low, initial motion does not occur at the channel margins, which corresponds to the observations made previously.

While profile 1 is located at the transition to the alluvial surface and is approx. the downstream limit of

the narrow slot canyon, the second profile is located in the wide debris cone. Due to rising discharge rates, bed shear stress is also exerted on newly inundated channels or parts of the floodplain. During discharge rates of 1 m<sup>3</sup>/s and 3 m<sup>3</sup>/s bed shear stresses are recorded from 41 m to 59 m along the second profile (Figure 39). Assuming 1 m<sup>3</sup>/s, incipient sediment motion only occurs at certain points under the condition of  $\tau_b^* = 46.35$  Pa, while  $\tau_b^* = 66.21$  Pa is not surpassed at all. At a magnitude of 3 m<sup>3</sup>/s, the exerted stress is greater than both thresholds (Table 4). However, this is limited to a small area. As a result of the increase in discharge rates to 25 m<sup>3</sup>/s, the area in which the bed shear stress exceeds the thresholds is expanding. The measured maximum is about 293 Pa. During a peak flow of 25 m<sup>3</sup>/s bed shear stresses are obtained between 22 m and 63 m and from 91 m to 103 m, but initial movement is only triggered from approx. 35 m to 60 m.

The situation along the third profile is again different. Even at low discharge rates, the measured bed shear stresses reflect the braided river system. Three local maxima are observed (Figure 39). In between there are one or two minima. However, at a magnitude of 1 m<sup>3</sup>/s, the exerted bed shear stresses are too low to surpass either of the critical threshold values. During a discharge rate of 3 m<sup>3</sup>/s, they are greater than  $\tau_b^* = 46.35$  Pa at the second and the third maxima. However,  $\tau_b^* = 66.21$  Pa is not surpassed. Under the assumption of a magnitude of 25 m<sup>3</sup>/s and  $\tau_b^* = 46.35$  Pa, the sections susceptible to sediment movement have considerably enlarged. In addition, the bed shear stresses at the three maxima are greater than  $\tau_b^* = 66.21$  Pa for the first time across the third profile (Table 4). The highest value during a discharge rate of 25 m<sup>3</sup>/s is about 132 Pa. At 1 m<sup>3</sup>/s and 3 m<sup>3</sup>/s, values are recorded between 37 m and 46 m, 83 m and 101 m and between 107 m and 129 m. At a magnitude of 25 m<sup>3</sup>/s, bed shear stresses are measured between 29 m and 129 m. This shows the greatest expansion of the bed shear stresses along the profiles.

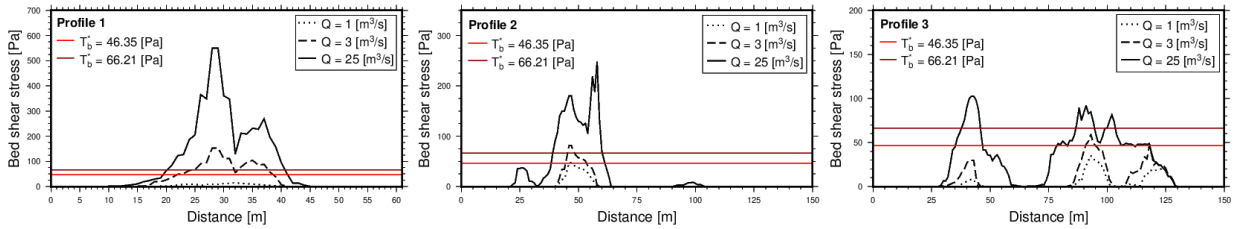


Figure 39: Maximum bed shear stress [Pa] plotted against the distance of the profiles during rising peak flows ( $Q = 1, 3$  and  $25 \text{ m}^3/\text{s}$ ). The distances starting from 0 m at the orographic right sight. The thresholds for initial sediment motion  $\tau_b^* = 46.35$  Pa and  $\tau_b^* = 66.21$  Pa are marked red. Sediment movement occur along the profiles if the bed shear stress surpasses the critical threshold.

For a further analysis, the increase in the exerted maximum bed shear stresses measured at the eight stations during rising discharge rates were examined (Figure 40). It is noticeable that at station 1 both threshold values were already exceeded below a peak flow of 1 m<sup>3</sup>/s. At this low magnitude, initial sediment movement at stations 2 and 5 are predicted, but only under the condition of  $\tau_b^* = 46.35$  Pa. The maximum bed shear stress applied at station 8 is only barely insufficient to surpass the lower threshold value at this discharge rate. Thus, initial sediment motion occurs here, as well as at the stations 4 and 7, from a discharge of 3 m<sup>3</sup>/s. Under the assumption of  $\tau_b^* = 66.21$  Pa, initial motion starts at the stations 2, 4, 5 and 8 from a magnitude of about 3 m<sup>3</sup>/s. At the seventh station, a discharge rate of 5 m<sup>3</sup>/s is necessary to exceed the higher threshold value. Overall, the threshold discharges required to trigger initial movement of sediment at the data loggers are summarized in Table 4.

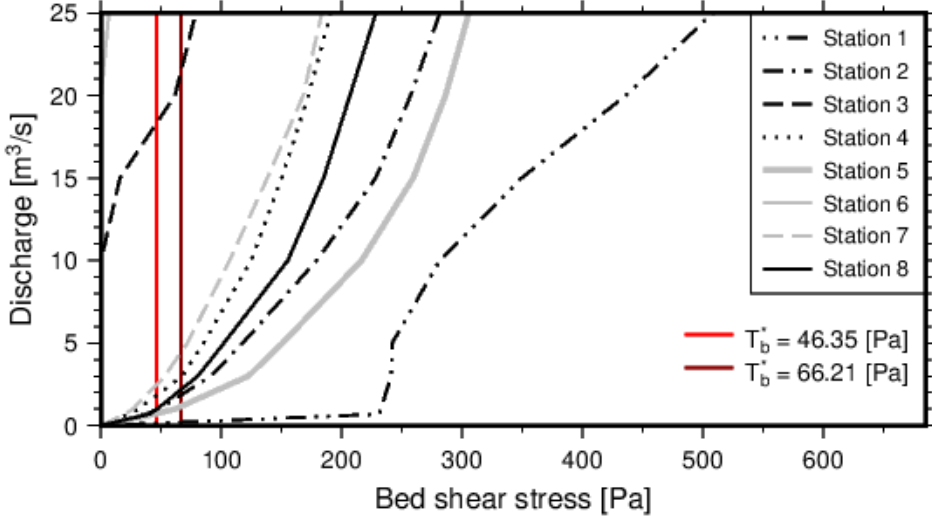


Figure 40: Increasing maximum bed shear stress [Pa] during rising peak flows at the eight stations. The thresholds for initial sediment motion,  $\tau_b^* = 46.35 \text{ Pa}$  and  $\tau_b^* = 66.21 \text{ Pa}$  in dependency of the median grain size, are marked in red.

As the stations 3 and 6 are positioned outside the main channel, significantly higher magnitudes are required to exceed both  $\tau_b^* = 46.35 \text{ Pa}$  and  $\tau_b^* = 66.21 \text{ Pa}$  (Table 4). However, as already shown in Figure 32, station 3 is initially inundated at a magnitude of about  $13 \text{ m}^3/\text{s}$ , and at station 6 at approximately  $25 \text{ m}^3/\text{s}$ . A discharge of  $25 \text{ m}^3/\text{s}$  leads to bed shear stresses at station 3 that are greater than both threshold values. At station 6, the lower critical value is surpassed at a peak flow of  $50 \text{ m}^3/\text{s}$ . There, even a discharge rate of  $100 \text{ m}^3/\text{s}$  under the condition of  $\tau_b^* = 66.21 \text{ Pa}$  is not sufficient to trigger sediment movement, as only a maximum bed shear stress of  $60.25 \text{ Pa}$  is recorded. Thus, significantly higher magnitudes than at the stations within the main channel are required.

Table 4: Critical discharge rates necessary to cause initial sediment motion at the virtual data loggers. The required magnitudes for both the lower,  $46.35 \text{ Pa}$  based on a median grain diameter of  $0.07 \text{ m}$ , and upper shear stress,  $46.35 \text{ Pa}$  based on a median grain diameter of  $0.07 \text{ m}$ , are listed. The stations and profiles are annotated by S1 - S8 and P1 – P3, respectively.

Data logger	$D_{50} = 0.07$	$D_{50} = 0.1$
	$\tau_b > \tau_b^*$	$\tau_b > \tau_b^*$
S1	$1 \text{ m}^3/\text{s}$	$1 \text{ m}^3/\text{s}$
S2	$1 \text{ m}^3/\text{s}$	$3 \text{ m}^3/\text{s}$
S3	$20 \text{ m}^3/\text{s}$	$25 \text{ m}^3/\text{s}$
S4	$3 \text{ m}^3/\text{s}$	$3 \text{ m}^3/\text{s}$
S5	$1 \text{ m}^3/\text{s}$	$3 \text{ m}^3/\text{s}$
S6	$50 \text{ m}^3/\text{s}$	$> 100 \text{ m}^3/\text{s}$
S7	$3 \text{ m}^3/\text{s}$	$5 \text{ m}^3/\text{s}$
S8	$3 \text{ m}^3/\text{s}$	$3 \text{ m}^3/\text{s}$
P1	$3 \text{ m}^3/\text{s}$	$3 \text{ m}^3/\text{s}$
P2	$1 \text{ m}^3/\text{s}$	$3 \text{ m}^3/\text{s}$
P3	$3 \text{ m}^3/\text{s}$	$25 \text{ m}^3/\text{s}$

## 5.5 Critical shear stress for plucking

Figure 41 displays the ratio between the maximum bed shear stress and the lower and upper critical shear stress for plucking during different peak flows. The areas where the basal shear stress exceeds the threshold value are marked in red. It is recognizable that for both ratios the potential sites of plucking increase in parallel to rising discharge rates. At a discharge rate of 25 m<sup>3</sup>/s, under the precondition of the lower threshold, there are only isolated potential areas for plucking in the first half of the AOI. This particularly affects the areas adjacent to stations 1, 2 and 4 as well as to profile 1. Assuming  $\tau_{pc} = 684$  Pa, bedrock erosion is only possible before entering the gravel plain. On the gravel cone, the discharge does not cause the required bed shear stress to trigger block entrainment by sliding at any point. Consequently, larger magnitudes are demanded. However, even after doubling the discharge rate to 50 m<sup>3</sup>/s, the critical value is only occasionally exceeded under the condition of  $\tau_{pc} = 684$  Pa.

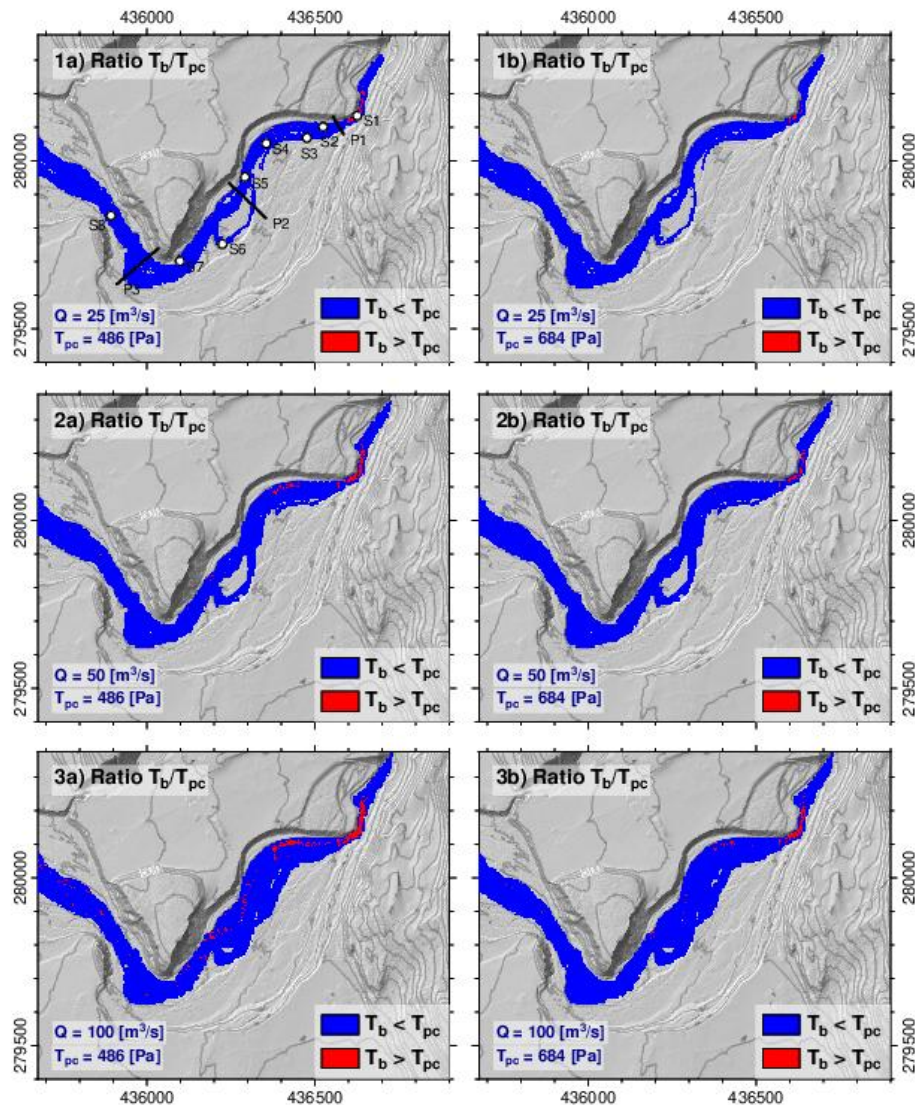


Figure 41: Ratio between maximum bed shear stress and the a) lower (486 Pa) and b) upper (684 Pa) critical shear stress for plucking jointed limestone during peak flows of 25, 50 and 100 m<sup>3</sup>/s. A ratio greater than 1 (depicted in red) indicates that the basal shear stress surpasses the threshold value ( $\tau_{pc} > \tau_b$ ). In contrast, if the bed shear stress is smaller than the threshold for plucking ( $\tau_{pc} < \tau_b$ ), the ratio is smaller than 1 (depicted in blue). The position of all stations (white circles) and profiles (black lines) are shown in 1a).

Potential sites for plucking are only situated in the upper part of the simulation domain up to about station 4. It is noticeable that the situation is comparable to that with a discharge of 25 m<sup>3</sup>/s and a threshold value of  $\tau_{pc} = 486$  Pa. If the magnitude is increased to 50 m<sup>3</sup>/s under the assumption of the lower critical value, an expansion of the potential areas for plucking is recognizable. In addition, the exerted bed shear stress also exceeds the threshold downstream of station 4. However, these are widely distributed punctual spots. The simulation of a flood event with a magnitude of 100 m<sup>3</sup>/s under the condition of  $\tau_{pc} = 486$  Pa shows that the potential areas for block entrainment have finally increased on the gravel surface. Now, enlarged potential areas can also be observed in the adjacency of station 5. Nevertheless, the most susceptible zones are located near station 1 and between stations 2 and 4. Assuming the same magnitude but  $\tau_{pc} = 684$  Pa, the exerted basal shear stress exceeds the threshold value at many fewer locations. Compared to a discharge rate of 50 m<sup>3</sup>/s and  $\tau_{pc} = 684$  Pa, the potential areas have nevertheless increased. This particularly affects the area near station 1 and the channel section above station 4. However, the bed shear stress also surpasses the critical value between stations 5 and 6 at some isolated points. Sporadically, at station 8 and downstream, the threshold value is exceeded again.

Overall, the two thresholds cause large differences in the prediction of the critical discharge. The bed shear stress exceeds the lower threshold in significantly more channel sections. The most susceptible areas are located before and during the transition to the gravel surface. Therefore, the situation along the first profile is examined in more detail (Figure 42). Here, the bed shear stress is compared in relation to  $\tau_{pc} = 486$  Pa and 684 Pa during three peak flows of 25 m<sup>3</sup>/s, 50 m<sup>3</sup>/s and 100 m<sup>3</sup>/s. The lower critical value is already surpassed at a magnitude of 25 m<sup>3</sup>/s, but only over a width of 3 m at the right channel side (Table 5). As a result of increasing the discharge to 50 m<sup>3</sup>/s this area is considerably enlarged and the upper threshold is now also exceeded. During a magnitude of 100 m<sup>3</sup>/s, the potential areas widen further. At this discharge rate, the critical shear stress  $\tau_{pc} = 486$  Pa is now also surpassed on the left channel side as well as  $\tau_{pc} = 684$  Pa in a comparatively smaller channel section. It is apparent that a local minimum of the maximum exerted bed shear stress is at about 32 m. The threshold range is not exceeded there even at a discharge rate of 100 m<sup>3</sup>/s.

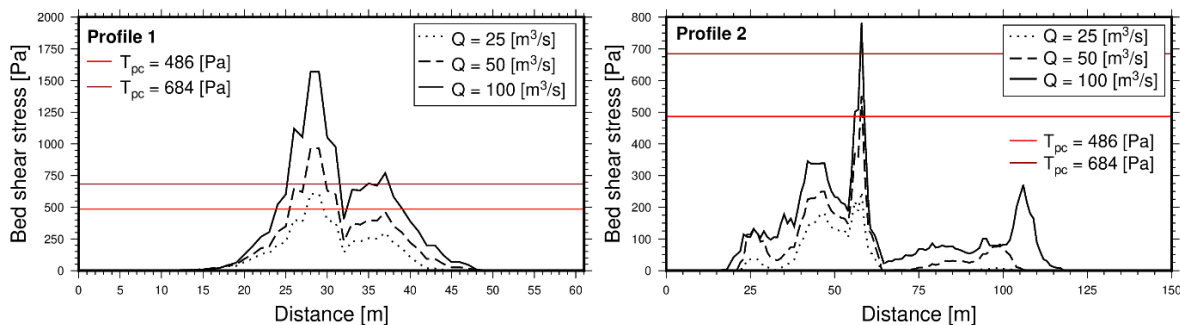


Figure 42: Maximum bed shear stress [Pa] plotted against the distance of a) profile 1 and b) profile 2 during rising peak flows ( $Q = 25, 50$  and  $100$  m<sup>3</sup>/s). The distance is starting from 0 m at the orographic right sight. The lower and upper threshold for plucking  $\tau_{pc}$ ,  $486$  Pa and  $684$  Pa, are delineated in red.

Figure 42 also shows the exerted maximum bed shear stress across the second profile, as potential areas for plucking were previously identified in this area. In comparison to the first profile, significantly lower basal shear stresses are reached. Consequently, the threshold range is exceeded in much smaller channel sections. At a discharge rate of 25 m<sup>3</sup>/s not even  $\tau_{pc} = 486$  Pa is surpassed at any point. Along a narrow

channel section, approximately between 55 m and 60 m, the lower threshold value is exceeded at a magnitude of 50 m<sup>3</sup>/s. In the same area,  $\tau_{pc} = 684$  Pa is also surpassed as a result of the increase in discharge rates to 100 m<sup>3</sup>/s. In general, the recorded maximum bed shear stresses along both profiles reflect the observations made in Figure 41 that larger potential areas for plucking are located in the upper part of the AOI.

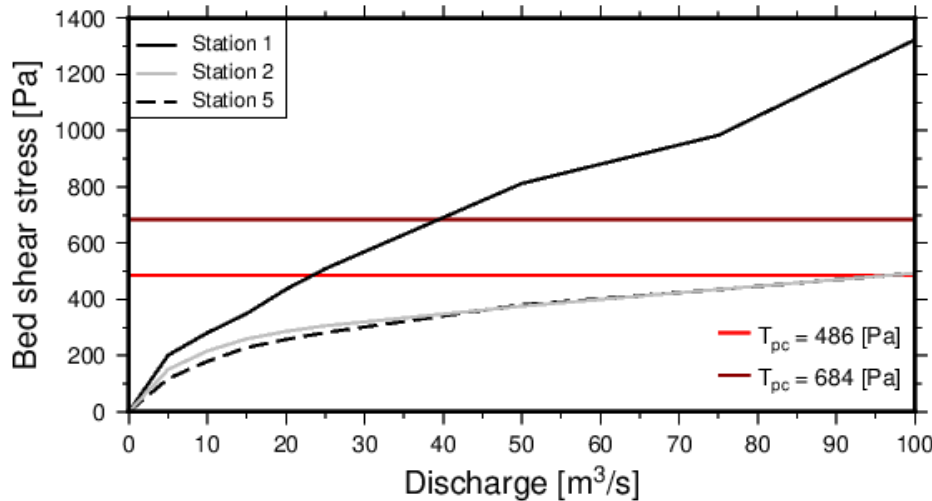


Figure 43: Increasing maximum bed shear stress [Pa] during rising peak flows at the three susceptible stations starting from 25 m<sup>3</sup>/s to 100 m<sup>3</sup>/s. The upper and lower threshold for plucking limestone, 486 and 684 Pa, are marked in red.

Figure 41 revealed that especially the area adjacent to station 1, as well as the channel section near the stations 2 and 5 at higher magnitudes, are susceptible for plucking. Thus, in Figure 43 the exerted maximum bed shear stresses, recorded at those virtual data loggers, are visualized during increasing discharge rates. It is apparent that the exerted bed shear stress at station 1 already surpasses the lower threshold at a magnitude of about 25 m<sup>3</sup>/s (Table 5). As a result of rising the peak flow to 40 m<sup>3</sup>/s, the upper threshold is also exceeded. In contrast, large discharge rates are necessary to cause a sufficiently high basal shear stress at the stations 2 and 5. While the lower critical value is surpassed at both stations just below a discharge rate of 100 m<sup>3</sup>/s (Table 5), the upper threshold is never exceeded. These results prove that the region near station 1 is much more susceptible to plucking, as comparatively low magnitudes can cause block entrainment.

Table 5: Critical discharge rates necessary to cause bed shear stresses that surpass at least the lower threshold for block entrainment by sliding.  $\tau_{pc} = 486$  Pa at the sites, where uncovered limestone beds were monitored. The stations and profiles are annotated by S1, S2 and S5 as well as by P1 – P2, respectively.

Data Logger	$\tau_b > \tau_{pc}$
S1	25 m <sup>3</sup> /s
S2	100 m <sup>3</sup> /s
S5	100 m <sup>3</sup> /s
P1	25 m <sup>3</sup> /s
P2	50 m <sup>3</sup> /s

## 6 Discussion

In this section the results are critically discussed. The main findings are the prediction of a critical discharge rate required for 1) the emergence of overbank floods, 2) initial sediment motion and 3) plucking limestone beds.

### 6.1 Overbank floods

As a consequence of increasing discharge rates, the capacity of main channels is exhausted, which leads to the progressive inundation of floodplains (Fernandes, 2021). The results from simulating single floods with varying magnitude have shown that the stations 3 and 6, which are positioned outside of the main channel within the floodplain, are inundated by exceeding a discharge rate of approx. 25 m<sup>3</sup>/s (Figure 32). During this magnitude, significantly higher water depths, flow velocities and bed shear stresses were recorded in the main channel than in the inundated floodplain (Figure 34, Figure 35 and Figure 36), which is according to several studies (e.g., Riahi-Madvar et al., 2011, Fernandes, 2021) a characteristic of the complex flow pattern during overbank floods. These spatial differences in water depth and flow velocity are important topics in recent studies (e.g., Fernandes, 2020, Fernandes, 2021), as they cause a shear layer that affect the transport capacity.

Several studies (e.g., Nicholas and Mitchell, 2003, Wilson and Atkinson, 2005) have emphasized the strong impact of the input relief on the progressive flooding of floodplains, which is also observed in the results of this thesis. Since the DEM used as the topographic foundation for the numerical flood simulations has a resolution of 1 m, local changes in elevation can influence the expansion of the inundation. According to Nicholas and Mitchell (2003), this effect would be even more apparent by using DEMs with a higher spatial resolution. In the simulation results, the impact of the topographic foundation is observed e.g. along the third profile. Here, marginal spots remain dry at a discharge rate of 25 m<sup>3</sup>/s, which are already inundated when increasing the discharge rates to 30 m<sup>3</sup>/s. The later flooding in those parts of the alluvium is caused by local increased relief values. However, Bridge (2003) states that the inundation of floodplains depends not only on the relief (e.g. sediment accumulations or depressions), but also on the floodplain width. The simulation results have shown that the alluvial cone is progressively flooded during rising discharge rates. In contrast, increasing magnitudes from 25 m<sup>3</sup>/s leads along the first profile primarily to variations in water depth rather than to a lateral expansion, as there is only a minor enlargement of the inundated area on the orographic left channel side (Figure 34). Examining that side of profile 1 on the orthophotos generated in 2018, 2019 and 2021 reveals that it correlates with the zone in which the bedrock is temporarily covered by sediments (Figure 22 and Figure 23). In line with Bridge (2003), the floodplain width is the reason for the predominant variation in water depth and less in inundated width in the mentioned site, because the first profile is positioned between gently tipping bedrock and poorly developed floodplains.

Overall, the results of the numerical simulations provided important information about the hydraulic parameters, water depths, flow velocity and bed shear stress within the floodplain (Figure 34, Figure 35 and Figure 36). These could not be obtained through monitoring in the field due to the risks during high magnitude flood events (Nicholas and Mitchell, 2003). Information about the hydraulic parameters in

the floodplain is particularly important in braided river systems, as the morphological active width, or the lateral expansion of bedload transport, rises during overbank floods but is still rather discontinuous and show a high spatial variability. Overbank floods represent thus important morphological events in gravel- bed rivers, as they trigger changes in sediment erosion and deposition during a single flooding (Peirce et al., 2018). The determination of the required discharge rate to cause overbank floods is consequently important. However, its definition within the study area is particularly challenging due to the topographic impact regarding the input DEM. Although the data loggers outside the main channel (station 3 and 6) are flooded from a magnitude of  $25 \text{ m}^3/\text{s}$  onwards (Figure 32) and a mainly wide channel with high (main channel) and low (floodplain) water depths, flow velocities and bed shear stress has formed in the alluvial cone, which is a characteristic of overbank floods according to Riahi-Madvar et al. (2011), there are still dry spots within the wide alluvial plain (Figure 34). Nevertheless, it can be assumed that overbank floods occur from a discharge rate  $\geq 25 \text{ m}^3/\text{s}$  in the study area. It is important to state that the results are heavily dependent on the topographical basis. Changes in sediment deposition and erosion have been occurred over time due to dynamic alterations in the riverine landscape. This can cause changes in the progressive inundation of the floodplain, making some sections more and some less susceptible to flooding. The threshold discharge for overbank flood is thus merely an approximation and must be continuously adapted to the new situations in the AOI in order to minimize uncertainties. Nonetheless, according to the hydrological service of Salzburg, a discharge rate of  $25 \text{ m}^3/\text{s}$  corresponds to a flood recurrence interval of one year. This interval is in line with the typical recurrence interval of overbank floods between approx. one to two years, in accordance with various studies (e.g., Bridge, 2003, DiBiase and Whipple, 2011, Rhoads, 2020).

## 6.2 Initial sediment motion

The prediction of incipient sediment movement is considered to be amongst the most elementary issue in the field of geomorphology (Lamb et al., 2008). The threshold calculation in this study is based on the median grain size, which was calculated not only by field measurements but also derived from a roughness map. This chapter thus discusses the impact of the uncertainties in the median as well as the advantages and disadvantages of its determination based on a roughness map. According to Phillips and Jerolmack (2016), predicting the initial sediment motion is fundamental for understanding alterations in the riverine landscape. Therefore, the critical discharge rate required for the Taugl River to become geomorphological active within the study area is also assessed.

### 6.2.1 Advantages and potential errors of determining the median grain diameter based on the calculated roughness map

The calculation of a threshold for incipient sediment motion  $\tau_b^*$  requires the determination of the median grain diameter  $D_{50}$  (9) (Larsen and Lamb, 2016). The resulting median diameters, derived from field measurements ( $D_{50} = 0.07 \text{ m}$ ) and statistical evaluation of the roughness map ( $D_{50} = 0.1 \text{ m}$ ) differ by  $0.03 \text{ m}$ . As a consequence, the calculated threshold values for incipient sediment movement ( $\tau_b^* = 46.35 \text{ Pa}$  and  $\tau_b^* = 66.21 \text{ Pa}$ ) deviate by  $20 \text{ Pa}$ . The results of the ratio between the median and the critical shear stress for initial movement even show a linear correlation (Figure 28). Thereby, the median grain size

could be identified as one of the key controlling factors for initial sediment motion, in accordance with previous studies (e.g., Lamb et al., 2015).

Several advantages of the calculation of the median grain size based on roughness maps exist. One among others is that more samples can be taken in a shorter period of time compared to field measurements. Even though the grain size distributions of both approaches are similar (Figure 26), the number of recorded sediments ( $z$ - values) is significantly higher when calculating the median based on the roughness map. Due to the higher amount of samples, the result could be more accurate. Another benefit compared to field based measurements is that the natural structure in the river landscape is not disturbed (Scheingross et al., 2013).

However, there are also disadvantages in median grain size calculations via roughness map. According to Bunte and Abt (2001) errors can occur when the median axis of sediments is not oriented to match the elevation values on the roughness map or due to clasts embedment. However, this would cause a decrease in the median compared to the result of the field measurements. In the results of this thesis, however, the median based on the roughness map is comparatively higher. The reason for the higher value could be the alluvial wood deposited on the floodplain, which was not taken into account for the calculation. According to Vázquez-Tarrío et al. (2017), this is one of the main reasons for errors in UAV based roughness maps, as the roughness values refer not only to sediments but also to deadwood.

### 6.2.2 Sediment remobilization

Due to the variations in the obtained median grain sizes, a threshold range for initial motion of sediments ( $\tau_b^* = 46.35 - 66.21 \text{ Pa}$ ) within the study area was calculated to approximate the real value. This threshold range is lower compared to the results of Larsen and Lamb (2016), whose approach was followed for the threshold calculation. However, the values of some parameters for the calculation differ due to the differences between the areas of interest. In the study area of Larsen and Lamb (2016), e.g. the calculated median grain size is higher ( $D_{50} = 0.15 \text{ m}$ ), which explains the higher critical bed shear stress for initial movement.

The calculation of the threshold range for incipient movement of sediments in this thesis is based on a constant critical Shields number ( $\tau_c^* = 0.045$ ), which is according to several studies (e.g., Church, 2006, Lamb et al., 2008, Scheingross et al., 2013) valid for low gradient gravel- bed rivers. However, Mueller et al. (2005) stated, biases in the critical Shields number can lead to an inaccurate determination of initial sediment movement. In order to evaluate the resulting critical threshold range in this thesis, future studies should calculate thus the exact value of the critical Shields number. In numerous studies (e.g., Church and Hassan, 2002, Aristide Lenzi et al., 2006, Scheingross et al., 2013) the maximum grain size transported during a flood event is used to determine the critical Shields number (8). The calculation consequently also requires the maximum exerted bed shear stress during the flooding (Scheingross et al., 2013). Since a pressure probe was installed a few metres downstream of the Römer Brücke as part of this thesis, whose operating principles are explained elsewhere, discharge data are available for future flood events that can serve as input for numerical simulations. Thereby, the maximum exerted bed shear stress during the flood event can be calculated. Moreover, by continuing the UAV based monitoring series within the study area, the largest transported grain size during a flooding could be identified based

on the derived products. However, this would require surveys before and after the event. Overall, all requirements to calculate the exact critical Shields number in the study area are achievable.

Based on the results of the modelled ratios between the threshold range for incipient sediment movement and the exerted maximum bed shear stress during different discharge rates, two different situations can be identified in the study area (Figure 38). Firstly, it is apparent that until the downstream limit represented by profile 1, sediments are remobilised even at very low discharge rates ( $Q = 1\text{m}^3/\text{s}$ ) (Table 4). Secondly, initial sediment motion occurs only sporadically at similar discharge rates in the alluvial segment further downstream. Thereby it can be concluded that the exerted bed shear stress in the channel section upstream of profile 1 is higher than downstream. This assumption is confirmed by the simulation results (Figure 34). It is conspicuous that the channel section where the higher bed shear stress values are recorded corresponds to the form of a narrow slot canyon. In contrast, the stream is bordered by wide floodplains within the alluvial cone downstream of profile 1. This demonstrates that the channel width causes spatial and quantitative differences in the basal shear stress (Figure 36), in line with statements of Lamb et al. (2015). Because of its importance, the effects of channel width on the basal shear stress are recently discussed in more detail in various studies (e.g., Cook et al., 2020).

The analysis of the orthophotos indicate that bedrock is partly exposed in the channel section upstream of profile 1 with spatial and temporal variations (Figure 22 and Figure 23). As stated above, sediment remobilisation takes place in this site at a discharge rate of  $1\text{ m}^3/\text{s}$  (Figure 38). Due to the evaluation of the discharge data provided by the hydrographic service of Salzburg, it is known that the average daily discharge corresponds to this discharge rate. At station 1, however, maximum basal shear stresses high enough to trigger incipient motion of sediments are measured even at lower discharge rates (e.g. a discharge rate of  $0.7\text{ m}^3/\text{s}$  conducts to a maximum bed shear stress of approx.  $231\text{ Pa}$ ) (Figure 40). It can therefore be assumed that the limestone beds are exposed or only covered by a thin alluvial layer during most of the time, which is according to Whipple et al. (2000) one of the characteristics of bedrock rivers. Consequently, the described section of the Taugl River can be classified as a bedrock channel.

Transport and re- deposition of sediments heavily contribute to the surface shape (Yang et al., 2019). For monitoring alterations within the study area a prediction of a discharge thresholds triggering incipient movement of sediments is thus important. The simulated flood scenarios predict initial motion of sediments within the alluvial cone over large, continuous areas from a critical discharge of  $\geq 3\text{ m}^3/\text{s}$  (Figure 38). As already mentioned sediment remobilization within the narrow slot canyon is triggered at lower discharge rates ( $< 1\text{ m}^3/\text{s}$ ) (Table 4). In total, the magnitude of the threshold discharge for the incipient motion of sediments with respect to the discharge rates with a temporal resolution of 15 min, provided by the hydrographic service of Salzburg, tends to be low in contrast to the relatively high frequency (Figure 12). However, various studies (e.g., Mao et al., 2017) pointed out that biases occur when using the discharge to predict initial sediment movement without accounting the spatial variation of different grain sizes. Grain hiding is according to Scheingross et al. (2013) a result of the higher drag and decreased friction angle of bigger clasts due to their higher protrusion from the channel bed. By neglecting the effects of grain hiding in this thesis, local variations in the critical Shields number are not taken into account (Scheingross et al., 2013), which causes uncertainties in the prediction of incipient sediment movement in the study area.

### 6.3 Flood induced bedrock incision due to plucking

Consistent with the results presented by Lamb et al. (2015), the model results show that block entrainment by sliding is dependent on varying relative protrusion and dimensionless sidewall stress (Figure 30). In line with other studies (e.g., Coleman et al., 2003), the results show that critical Shields number decreases with increasing protrusion but rises with decreasing block length (Figure 30a). Besides, the plotted ratio between the critical Shields number and the dimensionless sidewall stress indicates that the block sidewall stress must correspond to a high proportion of block weight per sidewall unit, or according to Lamb et al. (2015),  $\tau_w^*$  must approximate 1, in order to increase the resistance of blocks from entrainment (Figure 30b).

Due to the uncertainties regarding the dimensionless block sidewall stress ( $\tau_w^* = 0 - 0.1$ ), a critical bed shear stress value range for plucking by sliding ( $\tau_{pc} = 486 - 684$  Pa) was obtained. This threshold range is roughly in concordance with the results of Larsen and Lamb (2016) ( $\tau_{pc} = 467 - 751$  Pa), whose approach was followed for the calculation. A major reason for the slightly different results is the lithology. In the study area of Larsen and Lamb (2016) basalt dominates, whose friction angle as well as the density is slightly higher than that of limestone (Table 1 and Table 2). Different studies (e.g., Lamb et al., 2015) have already pointed out, that the block friction angle has an impact on the erosion rates through plucking by sliding.

The simulated sites susceptible to plucking are located in the vicinity of the stations 1, 2 and 5 as well as around the profiles 1 and 2 (Figure 41). The results of the simulated ratios between the applied maximum basal shear stress and the threshold range for plucking can be validated based on the analysis of the orthophotos, as exposed bedrock was monitored in those sites (Figure 22 and Figure 23). As many previous studies (e.g., DiBiase and Whipple, 2011, Johnson, 2014, Beer and Turowski, 2015, Hurst et al., 2021) have pointed out, incision can only take place if bedrock is not buried by alluvium, as otherwise the erosion rate is influenced by the so called cover effect (i.e. covering sediments act like a shield). According to Johnson (2014), it is thus important to estimate the extent of the sediment layer at sites where bedrock incision is expected. Based on the results of incipient sediment motion discussed above, the channel section in the vicinity of station 1 to the downstream limit of profile 1 was classified as a bedrock channel with only a minor sediment layer. The simulation results show that plucking is triggered here at a discharge of  $25 \text{ m}^3/\text{s}$  (Figure 43 and Table 5). This magnitude is significantly higher than that required for sediment remobilization within the same channel section (Table 4). The prediction for bedrock incision by plucking in the area described is thus realistic for discharges  $\geq 25 \text{ m}^3/\text{s}$ .

Bedrock incision is a key driver for the development of riverine landscapes, as the erosive process defines the erosion limits for mountain slopes (Hurst et al., 2021). In order to monitor the morphological alterations in the study area, it is therefore important to determine the critical discharge rate that triggers bedrock erosion. The simulation results have shown that the threshold discharge for plucking limestone beds is  $\geq 25 \text{ m}^3/\text{s}$ , when potential sites were observed for the first time within the narrow slot canyon. In contrast, plucking within the alluvial cone requires higher discharge rates (Figure 41). However, this threshold discharge is only an approximation, due to uncertainties in the calculation of the critical bed shear stress. Besides the varying sidewall stress, the drag coefficient was assumed to be 1, as in most studies of plucking by sliding (e.g., Lamb and Dietrich, 2009, Lamb et al., 2015, Larsen and Lamb,

2016). However, recent studies (e.g., Hurst et al., 2021) have focused on a more accurate determination of the drag coefficient, which enables a more precise determination of the critical bed shear stress and consequently of the threshold discharge for plucking.

As stated by DiBiase and Whipple (2011), the critical discharge for bedrock erosion is commonly equated with that for overbank floods in alluvial rivers. This can be confirmed by the results of this thesis, as the threshold discharge rates for both plucking and overbank floods is 25 m<sup>3</sup>/s. The fact that this discharge rate recurs at intervals of one year, according to the hydrographic service of Salzburg, indicates that plucking is not a continuous but an irregular process, occurring during flood events with high magnitude but low frequency (Figure 12), which is generally confirmed (e.g., Snyder et al., 2003, Lamb et al., 2015, Langston and Temme, 2019).

## 7 Conclusion

The aim of this thesis was to predict the triggering discharge rates for incipient sediment motion and mechanical bedrock erosion through plucking and evaluate them in terms of their frequency and magnitude. To accomplish this, the effects of single flood events with varying discharge rates were investigated with regard to the threshold exceedance. This required the calculation of the critical bed shear stress for incipient sediment motion and plucking as well as the development of a physically based fluid dynamic model to simulate single floods of different magnitudes. In order to evaluate the simulation results, remote sensing data derived from a UAV based monitoring series were analysed in dedicated areas along the river course.

The resulting threshold for initial movement of sediments ranges between 46.35 Pa to 66.21 Pa, while the critical bed shear stress for plucking through block entrainment by sliding ranges from 486 Pa to 684 Pa. By simulating the ratio between the corresponding threshold range and the exerted maximum bed shear stress during single floods with different magnitudes, the corresponding threshold discharges were identified. With regard to incipient sediment motion, the Taugl River is geomorphologically active at  $\geq 3 \text{ m}^3/\text{s}$  in most channel parts within the study area. By evaluating this threshold discharge in terms of magnitude and frequency, a discharge time series indicate that initial sediment motion occurs at low magnitude events but with a relatively high frequency. The obtained threshold discharge for plucking limestone beds is  $\geq 25 \text{ m}^3/\text{s}$ . This exemplifies that plucking is not a continuous but an irregular process that occurs during high magnitude but low frequency flood events.

By modelling floods with different peak flows, overbank floods were determined and susceptible sites for initial sediment motion and plucking were located during events of various magnitudes. These areas were comprehensively verified via DEM and orthophoto analysis, both products derived from remote sensing data. The flood simulation results showed that at a discharge of  $\geq 25 \text{ m}^3/\text{s}$  the main criteria for an overbank flood are fulfilled. Thus, the discharge threshold is similar to that for plucking. Based on the susceptible sites for sediment remobilisation and plucking, the Taugl River can be divided into two channel sections in the study area. The first section is situated in a narrow canyon slot and the other is located downstream in an alluvial cone. In the upstream channel section, the maximum values of the hydrological parameters water depth, flow and shear velocity as well as bed shear stress were recorded within the results. The critical bed shear stress for initial sediment motion is thus exceeded during magnitudes smaller than the threshold discharge, whereby it can be assumed that the tipping limestone beds are exposed most of the time or are only covered by a thin alluvial layer. As a result, this section was classified as a bedrock channel, which is highly susceptible to plucking, since the bedrock is not protected from incision by a huge sediment cover.

Although the detailed analyses performed in this Master thesis are related to a channel section of the Taugl River, the chosen methodology and equations can also be used for research in similar study areas. The results of this thesis thus contribute to the research in fluvial geomorphology by predicting flood induced riverbed changes in an alpine environment during single floods. Since the bed shear stress during overbank floods and the critical shear stresses in torrents are not well explored yet, the results provide important contributions for a systematic characterisation of morphological activity in torrents at different discharge conditions.

## References

- AGISOFT 2020. Agisoft Metashape User Manual: Professional Edition, Version 1.6.
- AN, H., YU, S., LEE, G. & KIM, Y. 2015. Analysis of an open source quadtree grid shallow water flow solver for flood simulation. *Quaternary International*, 384, 118-128.
- ARISTIDE LENZI, M., MAO, L. & COMITI, F. 2006. When does bedload transport begin in steep boulder-bed streams? *Hydrological Processes*, 20, 3517-3533.
- BARTELS, G. K., CASTRO, N. M. D. R., COLLARES, G. L. & FAN, F. M. 2021. Performance of bedload transport equations in a mixed bedrock–alluvial channel environment. *CATENA*, 199, 105108.
- BAYNES, E. R. C., ATTAL, M., NIEDERMANN, S., KIRSTEIN, L. A., DUGMORE, A. J. & NAYLOR, M. 2015. Erosion during extreme flood events dominates Holocene canyon evolution in northeast Iceland. *Proceedings of the National Academy of Sciences*, 112, 2355-2360.
- BEER, A. R. & TUROWSKI, J. M. 2015. Bedload transport controls bedrock erosion under sediment-starved conditions. *Earth Surf. Dynam.*, 3, 291-309.
- BRASINGTON, J., VERICAT, D. & RYCHKOV, I. 2012. Modeling river bed morphology, roughness, and surface sedimentology using high resolution terrestrial laser scanning. *Water Resources Research*, 48.
- BRIDGE, J. S. 2003. Floodplains. *Rivers and floodplains: forms processes and sedimentary record*. UK: Blackwell Science.
- BRIDGE, J. S. 2016. The interaction between channel geometry, water flow, sediment transport and deposition in braided rivers.
- BUNTE, K. & ABT, S. R. 2001. *Sampling surface and subsurface particle-size distributions in wadable gravel- and cobble-bed streams for analyses in sediment transport, hydraulics, and streambed monitoring*, United States Department of Agriculture, Rocky Mountain Research Station, Fort Collins, CO. , 428.
- BUSSE, A., THAKKAR, M. & SANDHAM, N. D. 2017. Reynolds-number dependence of the near-wall flow over irregular rough surfaces. *Journal of Fluid Mechanics*, 810, 196-224.
- CAPONI, F., KOCH, A., BERTOLDI, W., VETSCH, D. F. & SIVIGLIA, A. 2019. When Does Vegetation Establish on Gravel Bars? Observations and Modeling in the Alpine Rhine River. *Frontiers Environmental Science*.
- CARRIVICK, J. L., SMITH, M. W. & QUINCEY, D. J. 2016. *Structure from Motion in the Geosciences*, John Wiley & Sons,
- CHURCH, M. 2006. Bed material transport and the morphology of alluvial river channels. *Annu. Rev. Earth Planet. Sci.*, 34, 325-354.
- CHURCH, M. & HASSAN, M. A. 2002. Mobility of bed material in Harris Creek. *Water Resources Research*, 38, 19-1-19-12.
- COLEMAN, S. E., MELVILLE, B. W. & GORE, L. 2003. Fluvial Entrainment of Protruding Fractured Rock. *Journal of Hydraulic Engineering*, 129, 872.
- COOK, K. L., TUROWSKI, J. M. & HOVIUS, N. 2020. Width control on event-scale deposition and evacuation of sediment in bedrock-confined channels. *Earth Surface Processes and Landforms*, 45, 3702-3713.
- COULTHARD, T. J. & VAN DE WIEL, M. J. 2013. Numerical Modeling in Fluvial Geomorphology. In: SHRODER, J. F. (ed.) *Treatise on Geomorphology*. San Diego: Academic Press, 694-710.

- DARBY, S. E. & VAN DE WIEL, M. J. 2003. Models in fluvial geomorphology. In: KONDOLF, G. M. & PIEGAY, H. (eds.) *Tools in fluvial geomorphology*. he Atrium, Southern Gate, Chichester, West Sussex PO19 8SQ, England: John Wiley & Sons, 501-537.
- DEAL, E., BRAUN, J. & BOTTER, G. 2018. Understanding the role of rainfall and hydrology in determining fluvial erosion efficiency. *Journal of Geophysical Research: Earth Surface*, 123, 744-778.
- DIBIASE, R. & WHIPPLE, K. 2011. The influence of erosion thresholds and runoff variability on the relationships among topography, climate, and erosion rate. *AGU Fall Meeting Abstracts*, 116, 06.
- DUBINSKI, I. M. & WOHL, E. 2013. Relationships between block quarrying, bed shear stress, and stream power: A physical model of block quarrying of a jointed bedrock channel. *Geomorphology (Amsterdam, Netherlands)*, 180-181, 66-81.
- FAVALLI, M., FORNACIAI, A., ISOLA, I., TARQUINI, S. & NANNIPIERI, L. 2012. Multiview 3D reconstruction in geosciences. *Computers & Geosciences*, 44, 168-176.
- FERGUSON, R. 2007. Flow resistance equations for gravel- and boulder-bed streams. *Water Resources Research*, 43.
- FERNANDES, J. N. 2020. Incorporating Apparent Shear Stress in the Roughness to Improve the Discharge Prediction in Overbank Flows. In: FERNANDES F., M. A., CHAMINÉ H. (ed.) *Advances in Natural Hazards and Hydrological Risks: Meeting the Challenge*. Springer, Cham.
- FERNANDES, J. N. 2021. Apparent roughness coefficient in overbank flows. *SN Applied Sciences*, 3, 696.
- GEOLOGISCHE BUNDESANSTALT. 2021. *KM200 Salzburg - Geologie*.
- GRACCHI, T., ROSSI, G., TACCONI STEFANELLI, C., TANTERI, L., POZZANI, R. & MORETTI, S. 2021. Tracking the Evolution of Riverbed Morphology on the Basis of UAV Photogrammetry. *Remote sensing (Basel, Switzerland)*, 13.
- GRENFELL, M. C. 2015. Modelling Geomorphic Systems: Fluvial. In: COOK, S. J., CLARKE, L. E. & NIILD, J. M. (eds.) *Geomorphological Techniques (Online Edition)*. London: British Society for Geomorphology.
- GUAN, M., CARRIVICK, J. L., WRIGHT, N. G., SLEIGH, P. A. & STAINES, K. E. H. 2016. Quantifying the combined effects of multiple extreme floods on river channel geometry and on flood hazards. *Journal of Hydrology*, 538, 256-268.
- GUTTMANN, M. 1997. *Das Tauglgebiet in der südwestlichen Osterhorngruppe*.
- HANCOCK, G., ANDERSON, R. & WHIPPLE, K. 1998. Beyond Power: Bedrock River Incision Process and Form. *Washington DC American Geophysical Union Geophysical Monograph Series*, 35-60.
- HARTLIEB, A. 2015. Schwemmholtz in Fließgewässern. *Lehrstuhl und Versuchsanstalt für Wasserbau und Wasserwirtschaft der Technischen Universität München*.
- HERGARTEN, S. & ROBL, J. 2015. Modelling rapid mass movements using the shallow water equations in Cartesian coordinates. *Nat. Hazards Earth Syst. Sci.*, 15, 671-685.
- HERGARTEN, S., ROBL, J. & STÜWE, K. 2013. Extracting topographic swath profiles across curved geomorphic features. *Earth Surface Dynamics*, 2.
- HURST, A. A., ANDERSON, R. S. & CRIMALDI, J. P. 2021. Toward Entrainment Thresholds in Fluvial Plucking. *Journal of Geophysical Research: Earth Surface*, 126, e2020JF005944.
- JANITZ, G. 2012. Managementplan Natur- und europaschutzgebiet "Tauglgries". In: EB&P UMWELTBÜRO GMBH, S. (ed.). Salzburg: Land Salzburg, Abteilung 13, Naturschutz.

- JOHNSON, J. P. L. 2014. A surface roughness model for predicting alluvial cover and bed load transport rate in bedrock channels. *Journal of Geophysical Research: Earth Surface*, 119, 2147-2173.
- KEEN, T. R., CAMPBELL, T. J., DYKES, J. D. & MARTIN, P. J. 2013. Gerris Flow Solver: Implementation and Application. NAVAL RESEARCH LAB STENNIS DETACHMENT STENNIS SPACE CENTER MS OCEANOGRAPHY DIV.
- KIM, J. Y., HOEY, T., BISHOP, P. & KIM, J.-Y. 2006. Erosion processes in bedrock river -A review with special emphasize on numerical modelling. *Korea Journal of Quaternary Research*, 20, 11-29.
- KIRCHNER, J. W., DIETRICH, W. E., ISEYA, F. & IKEDA, H. 1990. The variability of critical shear stress, friction angle, and grain protrusion in water worked sediments. *Sedimentology*, 37, 647-672.
- KONDOLF, G. M., PIÉGAY, H. & ASAHI, K. 2016. *Tools in fluvial geomorphology*, Chichester, UK : Hoboken, NJ : Wiley Blackwell,
- KRAMER, N. & WOHL, E. 2015. Driftcretions: The legacy impacts of driftwood on shoreline morphology. *Geophysical Research Letters*, 42.
- LAMB, M. P. & DIETRICH, W. E. 2009. The persistence of waterfalls in fractured rock. *Geological Society of America, GSA Bulletin* 121, 1123 - 1134.
- LAMB, M. P., DIETRICH, W. E. & VENDITTI, J. G. 2008. Is the critical Shields stress for incipient sediment motion dependent on channel-bed slope? *Journal of Geophysical Research: Earth Surface*, 113.
- LAMB, M. P., FINNEGAN, N. J., SCHEINGROSS, J. S. & SKLAR, L. S. 2015. New insights into the mechanics of fluvial bedrock erosion through flume experiments and theory. *Geomorphology*, 244, 33-55.
- LANGSTON, A. L. & TEMME, A. J. A. M. 2019. Bedrock erosion and changes in bed sediment lithology in response to an extreme flood event: The 2013 Colorado Front Range flood. *Geomorphology*, 328, 1-14.
- LAPOTRE, M. G. A., LAMB, M. P. & WILLIAMS, R. M. E. 2016. Canyon formation constraints on the discharge of catastrophic outburst floods of Earth and Mars. *Journal of Geophysical Research: Planets*, 121, 1232-1263.
- LARSEN, I. J. & LAMB, M. P. 2016. Progressive incision of the Channeled Scablands by outburst floods. *Nature*, 538, 229-232.
- LEDITZKY, H. P. 1990. Hydrologie des Tauglkessels. In: PLÖCHINGER, B. (ed.) *Erläuterungen zu Blatt 94 Hallein*. Wien: Geologische Bundesanstalt.
- LINDER, W. 2016. *Digital Photogrammetry: A Practical Course*, Berlin, Heidelberg, Berlin, Heidelberg: Springer Berlin / Heidelberg,
- LUHMANN, T. 2010. Erweiterte Verfahren zur geometrischen Kamerakalibrierung in der Nahbereichsphotogrammetrie. *Deutsche Geodätische Kommission bei der Bayerischen Akademie der Wissenschaften*.
- LUHMANN, T. & MAAS, H.-G. 2017. Industriephotogrammetrie. In: HEIPKE, C. (ed.) *Photogrammetrie und Fernerkundung: Handbuch der Geodäsie, herausgegeben von Willi Freeden und Reiner Rummel*. Berlin, Heidelberg: Springer Berlin Heidelberg, 105-155.
- MAO, L., DELL'AGNESE, A. & COMITI, F. 2017. Sediment motion and velocity in a glacier-fed stream. *Geomorphology*, 291, 69-79.
- MILLAR, R. G. 2000. Influence of bank vegetation on alluvial channel patterns. *Water Resources Research*, 36, 1109-1118.

- MUELLER, E. R., PITLICK, J. & NELSON, J. M. 2005. Variation in the reference Shields stress for bed load transport in gravel-bed streams and rivers. *Water Resources Research*, 41.
- NELSON, J. M., BENNETT, J. P. & WIELE, S. M. 2003. Flow and Sediment- transport Modeling. In: KONDOLF, G. M. & PIEGAY, H. (eds.) *Tools in Fluvial Geomorphology*. he Atrium, Southern Gate, Chichester, West Sussex PO19 8SQ, England: John Wiley & Sons
- NEX, F. & REMONDINO, F. 2014. UAV for 3D mapping applications: a review. *Applied Geomatics*, 6, 1-15.
- NICHOLAS, A. P. & MITCHELL, C. A. 2003. Numerical simulation of overbank processes in topographically complex floodplain environments. *Hydrological Processes*, Wiley InterScience.
- NIÑO, Y., LOPEZ, F. & GARCIA, M. 2003. Threshold for particle entrainment into suspension. *Sedimentology*, 50, 247-263.
- NOSS, C. & LORKE, A. 2016. Roughness, resistance, and dispersion: Relationships in small streams. *Water Resources Research*, 52, 2802-2821.
- PAJARES, G. 2015. Overview and current status of remote sensing applications based on unmanned aerial vehicles (UAVs). *Photogrammetric Engineering & Remote Sensing*, 81, 281-330.
- PEIRCE, S., ASHMORE, P. & LEDUC, P. 2018. The variability in the morphological active width: Results from physical models of gravel-bed braided rivers. *Earth Surface Processes and Landforms*, 43, 2371-2383.
- PHILLIPS, C. B. & JEROLMACK, D. J. 2016. Self-organization of river channels as a critical filter on climate signals. *Science*, 352, 694-697.
- POPINET, S. 2003. Gerris: a tree-based adaptive solver for the incompressible Euler equations in complex geometries. *Journal of Computational Physics*, 190, 572-600.
- POPINET, S. 2011. The Gerris Tutorial.
- POPINET, S. 2012. *Karamea flood tutorial* [Online]. Available: [http://gfs.sourceforge.net/wiki/index.php/Karamea\\_flood\\_tutorial](http://gfs.sourceforge.net/wiki/index.php/Karamea_flood_tutorial) [Accessed 03.07.2021 2021].
- RETTENBACHER, A. & RETTENBACHER-HÖLLWERTH, B. 1982. *Chronik von St. Koloman in der Taugl*, St. Koloman in der Taugl : Eigenverl. der Gemeinde St. Koloman in der Taugl,
- RHOADS, B. L. 2020. *River Dynamics: Geomorphology to Support Management*, Cambridge, Cambridge University Press,
- RIAHI-MADVAR, H., AYYOUBZADEH, S., NAMIN, M. & SEIFI, A. 2011. Uncertainty Analysis of Quasi-Two-Dimensional Flow Simulation in Compound Channels with Overbank Flows. *Journal of Hydrology and Hydromechanics*, 59, 171-183.
- ROBL, J. 2021. Angewandte numerische Verfahren in der Geologie. *Vorlesungsunterlagen*.
- SCHEINGROSS, J. S., WINCHELL, E. W., LAMB, M. P. & DIETRICH, W. E. 2013. Influence of bed patchiness, slope, grain hiding, and form drag on gravel mobilization in very steep streams. *Journal of Geophysical Research: Earth Surface*, 118, 982-1001.
- SCHERLER, D., DIBIASE, R. A., FISHER, G. B. & AVOUAC, J.-P. 2017. Testing monsoonal controls on bedrock river incision in the Himalaya and Eastern Tibet with a stochastic-threshold stream power model. *Journal of Geophysical Research: Earth Surface*, 122, 1389-1429.
- SELBY, M. J. 1993. *Hillslope materials and processes*, Oxford : Oxford Univ. Press,
- SMART, G. M., DUNCAN, M. J. & WALSH, J. M. 2002. Relatively Rough Flow Resistance Equations. *Journal of hydraulic engineering (New York, N.Y.)*, 128, 578.

- SNYDER, N., WHIPPLE, K., TUCKER, G. & MERRITTS, D. 2003. Importance of a stochastic distribution of floods and erosion thresholds in the bedrock river incision problem. *Journal of Geophysical Research*, 108, 2117.
- SPIEGLER, A. 1971. *Die Taugl : Landschaft und Landschaftsgeschichte, Hydrographie und Karst*.
- SURIAN, N. 2015. Fluvial Processes in Braided Rivers. In: ROWINSKI, P. & PAWLICK, A. R.-. (eds.) *Rivers- Physical, Fluvial and Environmental Processes*. Switzerland: Springer International Publishing, 403-425.
- TOTH, C. & JUTZI, B. 2017. Plattformen und Sensoren für die Fernerkundung und deren Geopositionierung. In: FREEDEN, W., RUMMEL, R. & HEIPLE, C. (eds.) *Photogrammetrie und Fernerkundung*. Berlin, Heidelberg: Berlin, Heidelberg: Springer Berlin Heidelberg, 64.
- TOURISMUSVERBAND BAD VIGAUN. 2021. *Lebensader Taugl* [Online]. Available: <http://www.lebensader-taugl.at/de/impressum> [Accessed 19.04.2021].
- VAN DIJK, W. M., TESKE, R., VAN DE LAGEWEG, W. I. & KLEINHANS, M. G. 2013. Effects of vegetation distribution on experimental river channel dynamics. *Water Resources Research*, 49, 7558-7574.
- VÁZQUEZ-TARRÍO, D., BORGNIET, L., LIÉBAULT, F. & RECKING, A. 2017. Using UAS optical imagery and SfM photogrammetry to characterize the surface grain size of gravel bars in a braided river (Vénéon River, French Alps). *Geomorphology*, 285, 94-105.
- VENDITTI, J. G., RENNIE, C. D., BOMHOF, J., BRADLEY, R. W., LITTLE, M. & CHURCH, M. 2014. Flow in bedrock canyons. *Nature*, 513, 534-537.
- WELBER, M. 2013. Morphodynamics and driftwood dispersal in braided rivers.
- WESTOBY, M., BRASINGTON, J., GLASSER, N., HAMBREY, M. & REYNOLDS, J. 2012. Structure-from-Motion photogrammetry: a novel, low-cost tool for geomorphological applications. 936.
- WHIPPLE, K. X., DIBIASE, R. A. & CROSBY, B. T. 2013. Bedrock rivers. In: SHRODER, J. & WOHL, E. (eds.) *Treatise on Geomorphology*. San Diego: Elsevier Inc., 550-573.
- WHIPPLE, K. X., HANCOCK, G. S. & ANDERSON, R. S. 2000. River incision into bedrock: Mechanics and relative efficacy of plucking, abrasion and cavitation. *GSA Bulletin*.
- WIBERG, P. L. & SMITH, J. D. 1987. Calculations of the critical shear stress for motion of uniform and heterogeneous sediments. *Water resources research*, 23, 1471-1480.
- WILSON, M. & ATKINSON, P. 2005. Prediction uncertainty in elevation and its effect on flood inundation modelling. *GeoDynamics*.
- WOLMAN, M. G. & MILLER, J. P. 1960. Magnitude and frequency of forces in geomorphic processes. *United States Geological Survey Professional Paper 282C*.
- WOODGET, A. S., AUSTRUMS, R., MADDOCK, I. P. & HABIT, E. 2017. Drones and digital photogrammetry: from classifications to continuums for monitoring river habitat and hydromorphology. *WIREs Water*, 4, e1222.
- YANG, Y., GAO, S., WANG, Y. P., JIA, J., XIONG, J. & ZHOU, L. 2019. Revisiting the problem of sediment motion threshold. *Continental Shelf Research*, 187, 103960.
- ZHANG, L., PARKER, G., STARK, C. P., INOUE, T., VIPARELLI, E., FU, X. & IZUMI, N. 2015. Macro-roughness model of bedrock-alluvial river morphodynamics. *Earth Surf. Dynam.*, 3, 113-138.

# Appendix

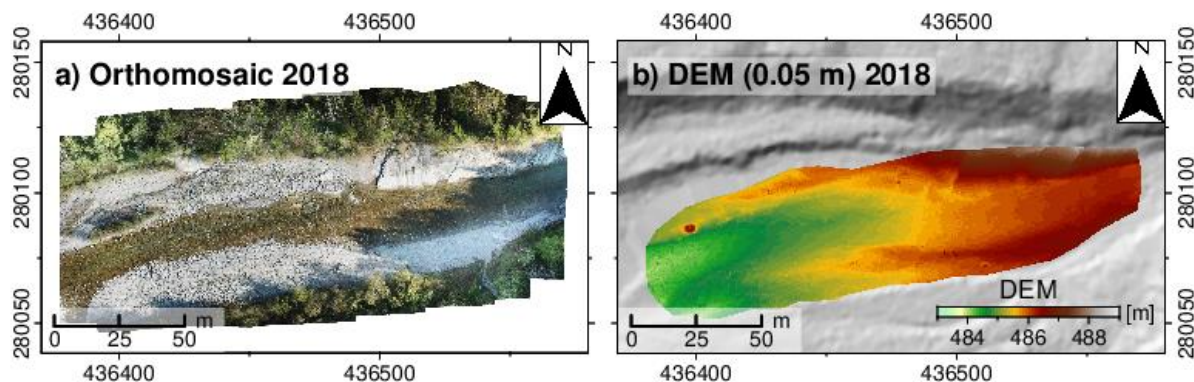
## Annotations

$\theta$	Bed slope
$\phi$	Frition angle
$\nabla$	2D gradient operator
$\omega, \alpha, \kappa$	Rotation angles of the x, y, z axes
$A_w$	Area of the block sidewall
$A_{xs}$	Cross sectional area of a sediment vertical to the stream
C	Chezy C friction parameter
C	Camera constant
$C_D$	Drag coefficient
$C_f$	Friction coefficient
$C_L$	Lift coefficient
D	Grain diameter
$D_{50}$	Median grain diameter
$D_{max}$	Maximum grain diameter
d	Mean flow depth
F	Collective term for all other acting forces
$F_B$	Buoyancy force
$F_D$	Drag force
$F_G$	Gravitational force
$F_g$	Aggregation of buoyancy and gravity forces
$F_L$	Lift force
$F_L^*$	Constant hydraulic lift force
$F_S$	Basal shear force
$F_w$	Block wall friction force
f	Focal length
f	Darcy-Weisbach friction parameter
g	Gravitational acceleration
H	Block height

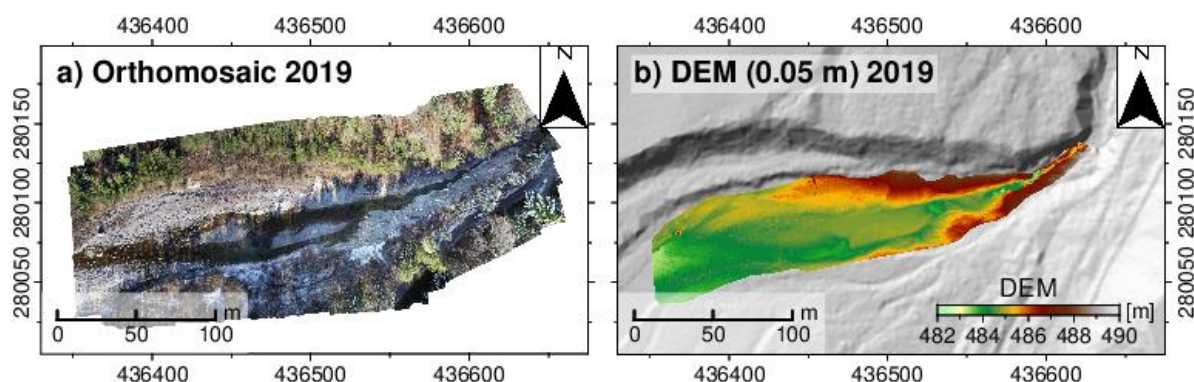
$H'$	Image main point
$h$	Water depth
$h_v$	Vertical flow depth
$I$	Mean slope
$L$	Block length
$n$	Manning's friction coefficient
$O'$	Position of the projection center
$P$	Protrusion height
$P'$	Point that deviates from the ideal position by $\Delta x'$ and $\Delta y'$
$p$	Pressure
$\rho$	Water density
$\rho_r$	Bulk density
$\rho_s$	Sediment density
$Re$	Reynolds number
$r_{123}$	Rotation value for x, y, z axes
$\tau$	Shear stress
$\tau_0$	Average shear stress
$\tau^*$	Shields number
$\tau_c^*$	Critical Shields number for initial sediment motion
$\tau_b^*$	Critical bed shear stress for initial sediment motion
$\tau_{pc}^*$	Critical Shields number for block entrainment by sliding
$\tau_b$	Bed shear stress
$\tau_{pc}$	Critical shear stress for plucking
$\tau_{max}$	Maximum bed shear stress
$\tau_w^*$	Block sidewall stress
$\tau_w$	Frictional stress along the block sidewalls
$U$	Mean flow velocity
$u$	Flow velocity
$u_*$	Shear velocity
$\mu$	Kinematic viscosity
$V_p$	Particle volume

$V_{ps}$	Submerged volume
$v_h$	Depth averaged horizontal velocity
$W$	Block width
$Z_0$	Roughness parameters
$Zb$	Topographic data

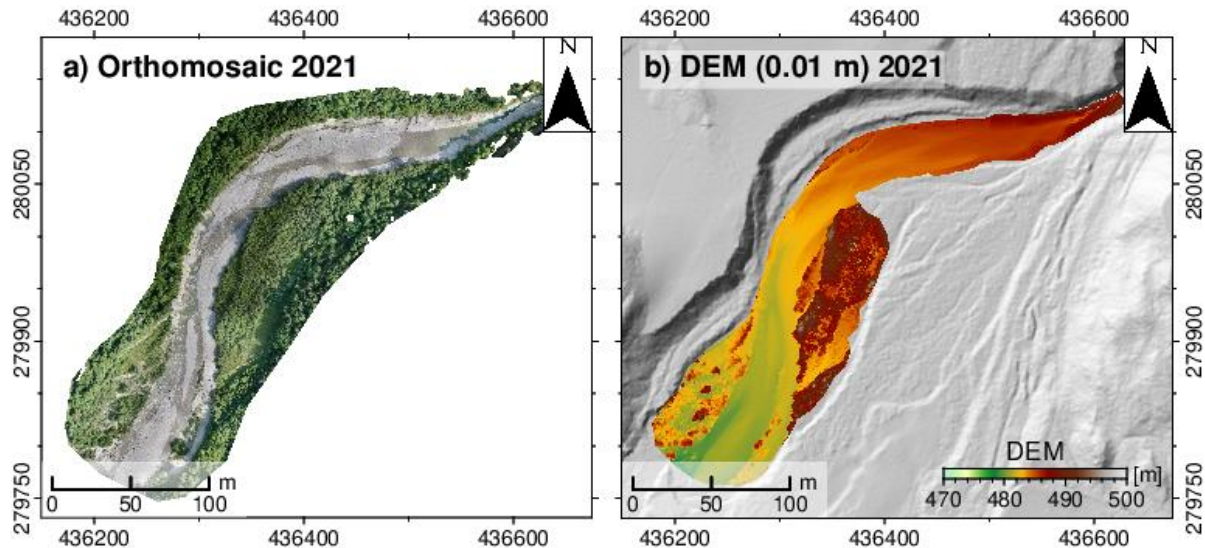
### Generated orthophotos and derived DEMs



Appendix 1: Orthomosaic and derived DEM processed with SfM photogrammetry and acquired via drone survey from 23.04.2018 with a spatial resolution of 0.05 m.



Appendix 2: Orthomosaic and derived DEM processed with SfM photogrammetry and acquired via drone survey from 04.12.2019 with a spatial resolution of 0.05 m.



Appendix 3: Orthomosaic and derived DEM processed with SfM photogrammetry and acquired via drone survey from 23.07.2021 with a spatial resolution of 0.05 m.

#### Executable flood simulation file based on GFS

#---- Defining variables

# DRY:	Determination of a dry cell if the fluid height is less than 1 mm
# SOURCE_X1:	X coordinate of the inflow point
# SOURCE_Y1:	Y coordinate of the inflow point
# MaxLevelOfRefinement:	Specifying the maximum level of refinement
# END:	Defining the last time step
# rho:	Setting the water density to 1000 [kg/m <sup>3</sup> ]
# T_cs:	Specifying threshold values e.g. for plucking

Define DRY 1e-3

Define SOURCE\_X1 436654.456191

Define SOURCE\_Y1 280248.793057

Define MaxLevelOfRefinement 9

Define END 6000

Define rho 1000

Define T\_cs486 486

Define T\_cs684 684

#---- Setting up the simulation domain and defining physical parameters

```
1 0 GfsRiver GfsBox GfsGEdge { x = 0.5 y = 0.5 } {
    PhysicalParams { L = 1400 g = 9.81 }
    MapTransform { tx = 435669.5 ty = 279389.5 }
```

```

GfsTime { end = END}

#---- Initialising variables

# MAX_P           Maximum water depth
# MAX_V           Maximum flow velocity
# MAX_T           Maximum bed shear stress
# MAX_u           Maximum shear velocity
# TIME_MAX_P      Time of maximum water depth
# T_base          Bed shear stress
# Velo            Flow velocity
# T_s             Lower and upper threshold values
# MAX_Ts          Maximum lower and upper threshold values
# density         Water density

Init {} {
  MAX_P = 0
  MAX_V = 0
  MAX_T = 0
  MAX_u = 0
  TIME_MAX_P = 0
  T_base = 0
  Velo = 0
  T_slower = 0
  T_upper = 0
  MAX_Tslower = 0
  MAX_Tupper = 0
  density = 1000

  # Specifying a constant hydraulic roughness is possible, but later on a variable roughness based on the
  # roughness map is implemented

  # Z0_roughness = 0.1
}

#---- Initialising the terrain module and defining the resolution at the inflow point
# Refinement of a circular area around with a centre at the inflow point (SOURCE_X1 and
# SOURCE_Y1) and radius 25 m

GModule terrain
Refine 8
Refine ((x - SOURCE_X1)* (x - SOURCE_X1) + (y - SOURCE_Y1) * (y - SOURCE_X1) <
25*25 ? 10 : 8)

```

```

#---- Implementing a DEM and assigning it to the variable Zb

    VariableTerrain Zb { basename = topo }

#---- Implementing the roughness map and assigning it to variable Z0
# Roughness is required in two different functions and must thus be implemented twice

    VariableTerrain Z0 { basename = rough2 }
    VariableTerrain Z0_roughness { basename = rough2 }

#---- Adaptive mesh refinement: Calculating the source area and cells with fluid with a high resolution
# istep = 1:      Recalling the function in each time step

AdaptFunction { istep = 1 } {
    cmax = 0
    minlevel = (t > 0 ? 1 : 7 )
    maxlevel = MaxLevelOfRefinement
} ((P > DRY) || (x - SOURCE_X1)*(x - SOURCE_X1) + (y - SOURCE_Y1) * (y - SOURCE_Y1)
< 25*25 ? 1 : 0)

#---- Implementing the friction model

# U and V represent the flow velocity in x and y direction
# Generation of a bimodal velocity distribution by function r*r which is related to the roughness of the
channel bed
# sqrt(U*U+V*V): Increase in flow resistance with rising flow velocity
# (P*P): Decrease in flow resistance with increasing water depth
# Specifying the required variables a and r for the friction model

SourceCoriolis 0 {
    if (P < DRY || Z0 < 1e-6) return 1e10;
    double a = P/Z0;
    double r = a > 2.718 ? 2.5*(log (a) - 1. + 1.359/a) : 0.46*a;
    return sqrt(U*U+V*V)/(P*P*r*r);
}

#---- Implementing bed shear stress in every time step
# T_r: initialising the roughness coefficient which is consistent to the parameter used for the friction
model
# Velocity: norm of the velocity vector

Init { step = 1 } {
    T_a = P/Z0_roughness;
    T_r = T_a > 2.718 ? 2.5*(log (T_a) - 1. + 1.359/T_a) : 0.46*T_a;
    T_base = P > DRY ? (Velocity/T_r)*(Velocity/T_r) * rho : 0
}

```

```

#---- Calculation of the ratio between bed shear stress and upper and lower critical values of the threshold
range in each time step

# Function is only solved if the water depth is greater than the defined variable DRY
# T_base > T_s: motion is triggered
# T_base < T_s: motion is not triggered

Init { step=1 } {
    T_slower = P > DRY ? (T_base/T_cslower) : 0
    T_supper = P > DRY ? (T_base/T_csupper) : 0
}

#---- Calculation of the shear velocity in every time step and assigning it to the variable u

# If water depth is greater than DRY, u is calculated as the square root of the bed shear stress
divided by the density of water

Init { step=1 } {
    u = P > DRY ? (sqrt(T_base/density)) : 0
}

#---- Assigning various parameters in each time step

# The condition P > DRY must be fulfilled

Init { step=1 } {
    TIME_MAX_P = P > MAX_P && P > DRY ? t : TIME_MAX_P
    MAX_P = P > MAX_P && P > DRY ? P : MAX_P
    MAX_V = Velocity > MAX_V && P > DRY ? Velocity : MAX_V
    MAX_T = T_base > MAX_T && P > DRY ? T_base : MAX_T
    MAX_u = u > MAX_u && P > DRY ? u : MAX_u
    MAX_Tslower = T_slower > MAX_Tslower && P > DRY ? T_slower : MAX_Tslower
    MAX_Ts684 = T_supper > MAX_Tsupper && P > DRY ? T_supper : MAX_Tsuppwe
    Velo = Velocity && P > DRY ? Velocity : Velo
}

#---- Specifying the position of the fluid source and time dependet inflow

# discharge.cgd: file that contains information about the discharge rate per time step in [m3/s]

SourceFlux P discharge.cgd (x >(SOURCE_X1 -10 ) && x < (SOURCE_X1 + 10 ) && y >
(SOURCE_Y1 -10 )&& y <(SOURCE_Y1 + 10 ) )

#---- Implementing the virtual data logger (stations and profiles)

# The position of the virtual data loggers was defined in other files

Include Taugl_Stations.gfs
Include Taugl_Profiles.gfs

```

```

----- Definition of which results are saved in what format and in which time step
# Output in the format of VTK files for visualisation with Paraview
# Solutions are generated every 60 secs

OutputSimulation {step = 60 } Taugl_%g.VTK { format = VTK depth = -1 }

# Output in the format of ASC files for visualisation with ArcGIS or GRASSGIS
# Solutions are generated every 600 secs

    OutputGRD { start = 0 step = 600 end = END } V_%g.asc { v = Velocity }
    OutputGRD { start = 0 step = 600 end = END } H_%g.asc { v = P }
    OutputGRD { start = 0 step = 600 end = END } T_%g.asc { v = T_base }
    OutputGRD { start = 0 step = 600 end = END } u_%g.asc { v = u }
    OutputGRD { start = 0 step = 600 end = END } Tslower_%g.asc { v = T_slower }
    OutputGRD { start = 0 step = 600 end = END } Tsupper_%g.asc { v = T_supper }

# Output in form of ASC files for visualisation with ArcGIS or GRASSGIS
# Solutions are generated at the end of the simulation

    OutputGRD { start = end} TIME_MaxH.asc { v = TIME_MAX_P}
    OutputGRD { start = end} MaxV.asc { v = MAX_V }
    OutputGRD { start = end} MaxH.asc { v = MAX_P }
    OutputGRD { start = end} MAXT.asc { v = MAX_T }
    OutputGRD { start = end} MAXu.asc { v = MAX_u }
    OutputGRD { start = end} MAXTslower.asc { v = MAX_Tslower }
    OutputGRD { start = end} MAXTsupper.asc { v = MAX_Tsupper }

----- Output in format of ASC files for visualisation with ArcGIS or GRASSGIS
# Solutions are generated at the end of the simulation
# OutputTime: Standard error is generated every time step
# OutputSimulation: Outputs of simulation are performed every time step of the simulated time

    OutputTime { istep = 1 } stderr
    OutputSimulation { step = 1 } stdout
}

----- Setting boundary conditions
# Simulation domain as a box

GfsBox {
    right = Boundary
    left = BoundaryOutflow
    top = Boundary
    bottom = BoundaryOutflow }

```